QUANTUM CHEMICAL SIMULATIONS OF THE MECHANICAL ACTIVATION OF PERICYCLIC REACTIONS

by

Gurpaul Singh Kochhar

A thesis submitted to the Department of Chemistry

In conformity with the requirements for

the degree of Master of Science

Queen's University

Kingston, Ontario, Canada

(December, 2011)

Abstract

Mechanochemistry, the use of mechanical stress to activate chemical reactions, has emerged as a significant area of interest in recent years. Two theoretical approaches have been developed to simulate mechanochemical processes: COnstrained Geometries Simulate External Force (COGEF) and External Force is Explicitly Included (EFEI). In the COGEF method, mechanical stress is simulated by increasing the distance between atoms in a molecule that serve as pulling points (PPs) at a constant rate. In the EFEI methods, a constant external force (F_{ext}) is applied between PPs, allowing the atoms to move to maintain that force. Both methods have been used in the literature to study the ring opening of cyclobutene under mechanochemical conditions. These studies have shown that applying a force between *cis* PPs in cyclobutene induces ring opening along the conrotatory pathway in COGEF-based simulations and ring opening along the disrotatory pathway in EFEI-based simulations. The latter is consistent with experiments. The work in this thesis identifies the origin of the differences in the outcomes obtained with these two methods, which may be of interest in the context of researchers selecting methods to simulate mechanochemical processes. The results demonstrate that the origin of the difference in behaviour is related to the manner in which these methods alter the potential energy surface (PES) through the application of a mechanical stress. Specifically, the PES obtained with the COGEF method does not contain a minimum energy pathway (MEP) linking cyclobutene to the disrotatory product, whereas the EFEI surface does contain such a path. The differences in PESs suggest that the EFEI method is more suitable to simulate mechanochemical processes. The EFEI approach was then used to examine how the electronic structure evolves to permit a formally forbidden disrotatory reaction to occur. The circumvention of the Woodward-Hoffmann rules was not due to a change in the electronic structure. Instead, the application of an external force shifts the transition state along the reaction coordinate towards the reactants, lowering the barrier for the reactions. The orbital effects that disfavor movement from reactants to products are rendered secondary to mechanochemical factors.

Acknowledgements

I would like to acknowledge the following people and organizations for their efforts in the completion of this thesis: my supervisor, Dr. Nicholas Mosey, for providing me with the in opportunity to work in his research group and guiding me in the area of mechanochemistry; the following professors for their assistance; Dr. Derek Pratt, Dr. Tucker Carrington, and Dr. Natalie Cann; fellow graduate students, Ben Carver and Adrian Bailey for collaborations and conversations on the topic of mechanochemistry; HPCVL, SHARCNET, and WestGrid for providing computational resources and financial support; Queen`s University and the Department of Chemistry for financial support; and finally my family for their support.

Table of Contents

List of Figures

List of Tables

List of Acronyms

AFM: Atomic Force Microscopy

BCB: Benzocyclobutene

CASSCF: Complete Active Space Self-Consistent Field

CPMD: Car-Parrinello Molecular Dynamics

COGEF: COnstrained Geometries simulate External Force

CSFs: Configuration State Functions

DOF: Degree of Freedom

DFT: Density Functional Theory

EFEI: External Force is Explicitly Included

FMPES: Force-Modified Potential Energy Surface

FPMD: First-principles Molecular Dynamics

GTOs: Gaussian type orbitals

IRC: Intrinsic Reaction Coordinate

LDA: Local Density Approximation

MEP: Minimum Energy Pathway

MD: Molecular Dynamics

NH: Nosé-Hoover

PES: Potential Energy Surface

PPs: Pulling Points

STOs: Slater type orbitals

TS: Transition State

TST: Transition State Theory

WH: Woodward-Hoffmann

Chapter 1:Introduction

1.1 Concept of Mechanochemistry

During chemical reactions, the reactants must overcome an energy barrier to be converted into products. This energy can be provided through heat, light, electrical potential, or by performing mechanical work on the system. These different means of activating reactions function by directing the applied energy to different degrees of freedom (DOFs) in either specific or non-specific ways, as outlined in Figure 1-1. Thermochemical activation involves heating the system, with the heat being distributed on average according to the equipartition principle. As such, the application of heat excites nuclear motions in a non-specific way. Photochemical methods involve subjecting molecules to radiation of particular wavelengths, which then induce specific transitions between electronic states to allow reactions to occur. Electrochemical methods affect the electronic DOFs in a non-specific manner by altering orbital energies through the application of an electric potential. At the molecular level, mechanical work can be performed on molecules by subjecting specific atoms, called pulling points (PPs), to mechanical stresses. These stresses result in the application of an external force (F_{ext}) between the PPs, which results in specific changes in molecular structure by altering the nuclear DOFs. The associated work performed on the system can be used to overcome reaction barriers. This approach is termed mechanochemistry. The combined ability to alter reaction barriers and induce specific changes in molecular structure through mechanochemistry may have several benefits for experimental research.

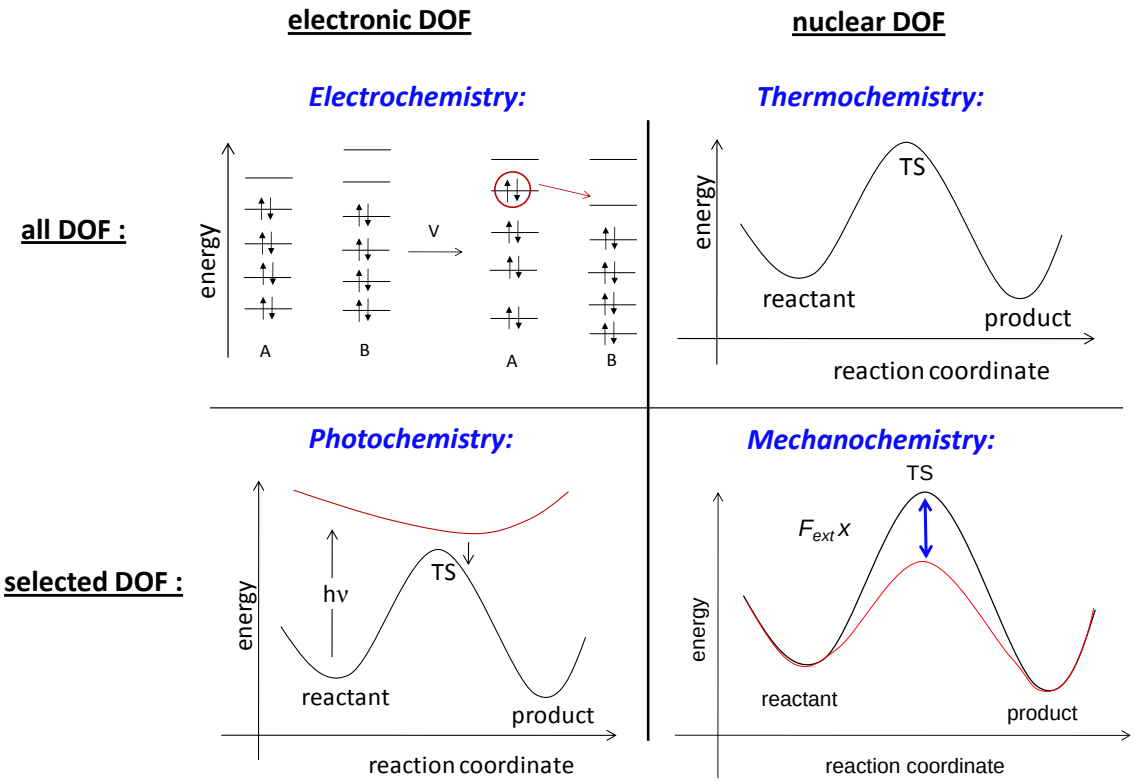

Figure 1-1: A demonstrative plot of how the different means of activating reactions affect the nuclear and electronic degrees of freedom (DOF). Both thermal and electrochemical means of activation increases the energy of all nuclear and electronic DOF respectively. Photochemical activation involves promoting reactions by targeting specific electronic DOF. In mechanochemistry, reactions are activated by applying an external force, F_{ext} to specific nuclear DOF.

Historically, mechanochemistry has been used to break down solid materials.[1] As noted above, mechanochemistry can also be used at the molecular level, and such efforts have gained interest in recent years.[2,3] This interest stems from the ability to lower reaction barriers while inducing specific changes in geometry to selectively activate reactions. The barrier is altered through two means. First, the application of F_{ext} deforms molecules along a specific direction on the ground-state PES which modifies the PES on which the molecule moves. Second, the application of F_{ext} performs work on the system in the amount of $W = F_{\text{ext}}q(\mathbf{x})$, where $\mathbf{x}$ represents the nuclear coordinates of the system and q represents the distance between PPs. The energy input by performing the work can contribute to that required to overcome the barrier, and

hence reduce the residual energy needed to overcome the barrier, e.g. through heat, is reduced. This concept is illustrated in Figure 1-2.

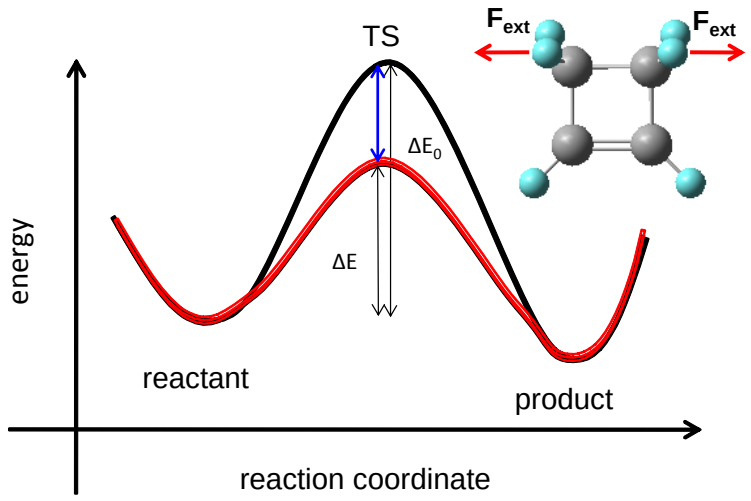

Figure 1-2: A demonstrative plot of how mechanical stress can be used to activate reactions. Here, ΔE_0 represents the reaction barrier on the Born-Oppenheimer PES (red curve) and ΔE represents the reaction barrier on the force-modified PES (black curve) that results from performing work on the system. The difference between the two reaction barriers is highlighted with a blue arrow. Mechanical stress is applied by applying F_{ext} to PPs in a molecule as shown in the cyclobutene structure.

1.2 Historical aspects of mechanochemistry

The majority of review articles date the origins of mechanochemistry to the textbooks of Fridrich Wilhelm Ostwald at the end of the 19th century.[1,4] Ostwald described mechanochemistry as the study of the chemical and physio-chemical changes of matter in all states of aggregation. Mechanochemistry in practice has been applied since prehistoric time when primitive peoples made fire from rubbing two rocks together. In this process, the mechanical energy from the friction between the two rock surfaces is converted into heat. Grinding and milling have also been used for millennia. The first recorded example of experimental mechanochemistry can be attributed to Theophrastus of Ephesus, a student of Aristotle. In this study, he found that rubbing

cinnabar with a brass pestle in a brass mortar in the presence of vinegar resulted in metallic mercury according to the mechanochemical reaction:

$$HgS + Cu \longrightarrow Hg + CuS \qquad (1.1)$$

During the twentieth century, mechanochemistry has found many applications in solid-state chemistry and materials science. Throughout this period, studies on solid-state mechanochemistry were focused on investigating the influence of high pressure on phase transitions in crystals and rates of solid-state reactions. [5] The application of mechanochemistry to material science was explored in the late 1960s. During this time, oxide-dispersion strengthened nickel and iron-based superalloys were prepared using a ball mill apparatus. This process, referred to as mechanical alloying, has developed into a powerful tool for the synthesis of alloys and other compounds that are difficult to prepare by conventional melting or casting techniques. [6] The mechanical activation of reactions using a ball mill apparatus occurs due to pressure and shear. The relationship between pressure and shear can be varied depending on specific features of the ball mill apparatus. Other apparati used to activate reactions are mills of shock action, which include jet mills, turbulent mills, and high peripheral-speed mills. Reactions are activated mechanochemically in these devices as the result of the collision of a particle with a solid surface in a gas jet or with a moving solid blade. Mills of shear action such as rollers and Leech mills are also used for mechanochemical synthesis. In this approach, a substance is placed between two solid surfaces. The substance is exposed to shear forces as one solid surface slides across another.

Although mechanical activation methods through grinding and milling are effective for the synthesis of solid materials on the bulk scale, they are largely non-specific in terms of the forces applied and the chemical bonds affected. The forces applied in these methods are not precise in terms of magnitude and direction. The non-specific nature of these methods has motivated the use of techniques with greater precision in the applied forces. The advances in mechanochemical methods from single-molecule manipulation techniques to molecular force probes and sonochemical experiments are discussed in Section 1.3.

1.3 Advances in mechanochemical methods

Single-molecule manipulation methods such as atomic force microscopy (AFM), optical tweezers, and magnetic tweezers have emerged as powerful experimental tools for studying the forces and motions associated with biological and chemical systems at the molecular level.[7] AFM-based techniques have had great success in single-molecule imaging and manipulation, specifically in investigating the mechanical design and folding properties of proteins. [8,9] In an AFM experiment, the molecule under study is held between a sharp tip at the end of the cantilever and a copper stage. A typical setup of an AFM experiment is shown in Figure 1-3. The force is applied to the molecule by increasing the separation distance between the sample surface and the cantilever. The displacement of the cantilever is measured from the reflection of a laser beam off the cantilever on a position-sensitive detector. The extension of the molecule can be determined from the separation distance between the cantilever tip and the sample surface. The force on the molecule can be determined from the spring constant and the deflection of the cantilever. The spring constant of the cantilever depends on the material properties and its shape, with typical values ranging from 10^1 to 10^5 pN / nm.[8] The values of the applied forces in AFM

experiments are on the orders of magnitude of 10^1 to 10^4 pN. This range of forces is sufficient for several mechanochemical processes, including bond rupture. [10]

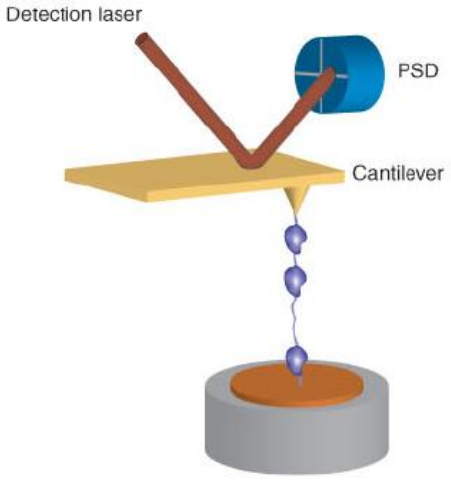

Figure 1-3: A general schematic of an AFM experiment. A protein molecule is attached to the sample surface and the cantilever tip. As the stage is retracted along the axial direction, the separation distance between the cantilever and the sample surface is increased. The deflection of the cantilever provides the force on the molecule and is measured from the reflection onto a position-sensitive detector. [11]

Optical tweezers, also known as an optical trap, have been used since the 1970s[12] and are often referred to as the most versatile single-molecule manipulation method.[13] In experiments using optical tweezers, a focused laser beam exerts radiation pressure on an optically transparent spherical bead. The molecule under study is attached to the bead through a non-covalent bond. The equilibrium position of the bead is near the focus of the laser beam. The shift of the bead from its equilibrium position results in a restoring force that is proportional to the displacement. For small displacements from the equilibrium position, the restoring force is linearly proportional to the displacement as shown in Hooke's law:

$$F = -k\Delta z \qquad (1.2)$$

where *F* is the magnitude of the restoring force, Δz is the extension from the equilibrium length, and *k* is the force or spring constant. The value of the spring constant depends on the steepness of the optical gradient (i.e. how tightly the laser beam is focused) as well as the polarizability of the trapped bead.[9] The applied force can also be generated by changing the intensity of the laser beam. In this case, the force acting on the bead is proportional to the gradient of the laser intensity.[14] Forces applied in experiments using optical tweezers are on the order of 0.1 to 100 pN in magnitude. [9] Optical tweezers have many applications in biological systems including trapping and manipulating viruses and bacteria[15], characterizing molecular-scale biological motors[16,17], and sorting cells by their intrinsic optical characteristics.[18]

Magnetic tweezers can also be used for the analysis of single molecules. In experiments using magnetic tweezers, the optically transparent plastic bead is replaced by a superparamagnetic bead that is controlled by an external magnetic field. The magnetic field exerts a constant force on the superparamagnetic bead. Simplified schematics of experiments using optical tweezers and magnetic tweezers are shown in Figure 1-4. The force applied to the bead is proportional to the gradient of the magnetic field at the position of the bead. Magnetic fields generated by sharp electromagnetic tips or small permanent magnets can be used to apply forces greater than 200 pN.[19] The applied force decreases as the bead moves further away from the magnet. Due to the properties of the magnetic field used to apply force, magnetic tweezers can be used to perform parallel single-molecule measurements.[20] The permanent magnet configuration in magnetic tweezers combines force-clamp properties with the ability to impose rotation. This makes magnetic tweezers ideally suited to investigate DNA topology. [21,22]

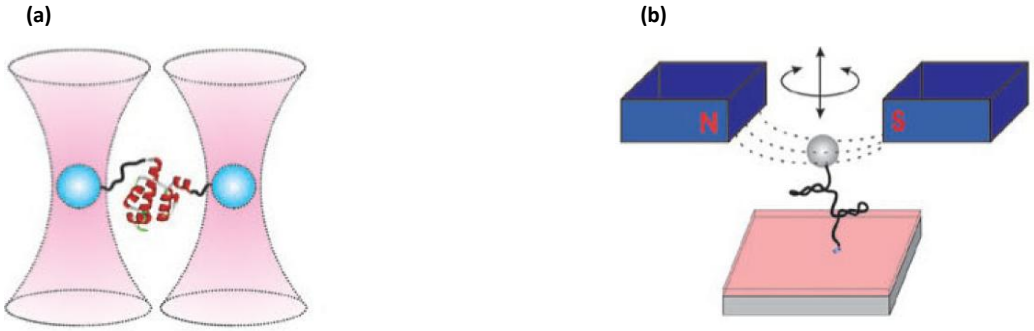

Figure 1-4: General schematics of single-molecule experimental techniques using (a) optical tweezers and (b) magnetic tweezers. Optical tweezers apply radiation pressure from a focused laser beam to transparent bead of distinct refractive index. The shift of the bead from the focal center produces a restoring force that is proportional to the displacement. Magnetic tweezers apply a force using an external magnetic field onto a superparamagnetic bead. The force applied is proportional to the gradient of the magnetic field**.** [23]

The use of AFM, optical tweezers, and magnetic tweezers allow precise forces to be applied to individual molecules. However, the single-molecule nature of these methods makes them unsuitable for practical synthetic efforts. Recent advances in molecular force probes and sonication experiments have made it possible to subject a large number of molecules to precise forces. The force ranges for these methods are summarized in Table 1-1.

Table 1-1: A comparison of the force ranges obtained using various mechanochemical methods

Mechanochemical method	**Force range (pN)**
Atomic force microscopy	10^1 - 10^3
Optical tweezers	0.1 - 100
Magnetic tweezers	0.1 - 200
Molecular force probes	150 - 600
Sonication	10^1 - 10^3

A molecular force probe is an inert molecule with a restoring force that can be varied systematically in increments of a hundred picoNewtons by constraining a single internuclear distance in the target molecule. The concept of a molecular force probe used to activate chemical reactions was first proposed by Boulatov (2009).[24] The authors in this study identified three

criteria that a molecular force probe must satisfy. First, the probe must be more structurally anisotropic than the functional group that it is bound to on the molecule. This would localize the strain on the non-reactive part of the molecule. Second, the functional groups and chemical reactions associated with the molecular force probe must be compatible with the molecule under study. [25] Finally, the molecular force probe should allow large restoring forces to be applied without the synthesis of highly strained molecules. An example of a molecule that is ideally suited to be a molecular force probe is stiff stilbene, which has two stable and structurally different isomers. Under photochemical conditions, *cis-trans* isomerization occurs about the central C=C bond in stilbene. The photoisomerization subjects the target molecule to external forces. The magnitude of the applied force can be controlled by using linkers of different lengths and chemical composition to connect the target molecule to the molecular force probe. The reaction under study was the ring opening of *trans*-3,4-dimethylcyclobutene to *trans*-2,4-hexadiene (Figure 1-5a). The reactant structure was connected to the phenyl rings in E and Z isomers of stilbene through linkers of approximately 16 to 20 atoms (Figure 1-5b). The dissociation of the carbon-carbon scissile bond in the reactant structure was found to be activated by the E-Z photoisomerization. The authors rationalized this by observing an accumulation of products at rates that depend on temperature and photon flux.

(a)

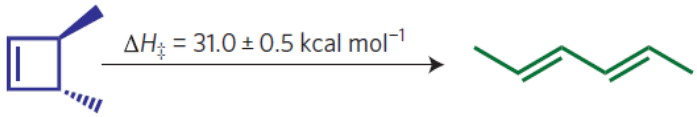

(b)

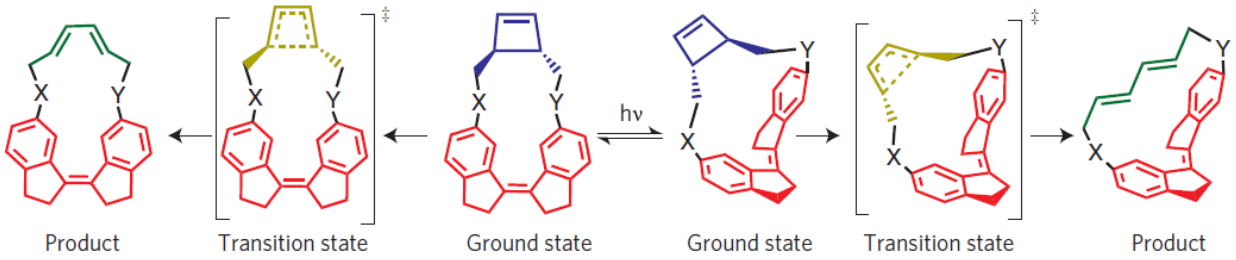

Figure 1-5: (**a)** Reaction scheme for the ring opening of *trans*-3,4-dimethylcyclobutene and (**b)** the structures of the macrocycles formed from incorporating the target molecule into the stiff stilbene molecular force probe via linkers. The linkers, X and Y, are of varying length and chemical composition. The force applied to the methyl groups attached to the carbon atoms of the scissile bond depend on the nature and length of the linker**.** [24]

Static quantum chemical calculations using density functional theory (DFT) were performed to calculate the restoring force that is exerted from the linkers. The DFT calculations showed that changes in enthalpic reaction barriers decreased steadily with increased size in macrocycle as illustrated in Figure 1-6.

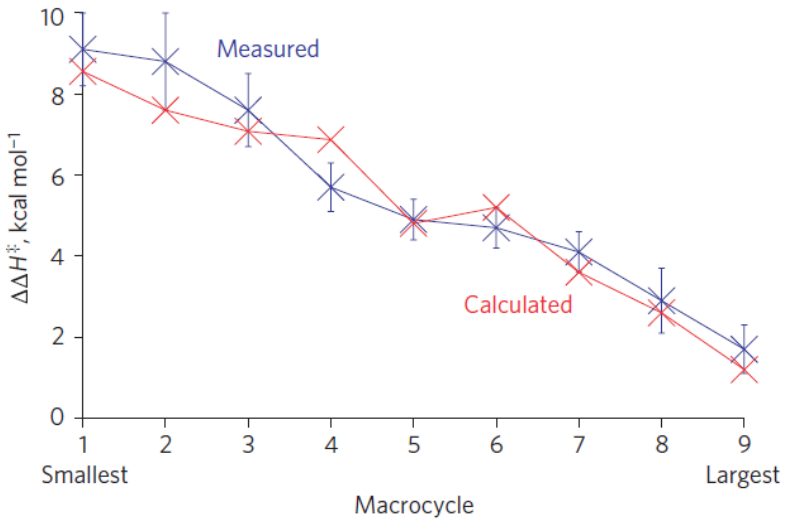

Figure 1-6: Measured (blue) and calculated (red) difference in enthalpic barriers for the formation of the Z and E products in the ring opening of *trans*-3,4-dimethylcyclobutene as a function of size of the macrocycle unit. The size of the macrocycle is used to modify the magnitude of the applied force, with larger macrocycles resulting in smaller forces.[24]

Using a molecular force probe to mechanically induce chemical reactions has several advantages. One of the main advantages is that bulk quantities of the probe-target molecule macrocycle can be synthesized and irradiated. Another advantage is the ability to modify the linkers used to connect the probe to the target molecule. Different linker sizes can permit restoring forces of varying magnitude and direction.

Sonication has become a popular technique for subjecting a large number of molecules to precise forces. [26,27] Sonication involves applying sound energy to agitate particles in a solution. The mechanical effects of ultrasound do not come from a direct interaction of the sonicator with the chemical species. Instead, mechanical action occurs due to acoustic cavitation.[28] This involves the formation, growth, and collapse of bubbles in a solution. The formation of cavitation bubbles occurs through a nucleated process, in which assembled molecules near the liquid-vapour interface are actively involved in the evolution of cavitation bubbles. [29] The

growth of cavitation bubbles can occur through various mechanisms. The use of high-intensity ultrasound results in a small cavity growing rapidly through inertial effects. At lower intensities, cavity growth occurs much slower through a process known as rectified diffusion. [26] In rectified diffusion, the growth process of the bubbles is greater than the shrinking process due to the fact that the cavity`s surface area is significantly greater during expansion than during compression. At a certain point during the growing process, the cavity bubble reaches a critical size where it can efficiently absorb energy from the external sound field. The critical size of the cavity is determined by the frequency of the ultrasound. Once the size of the cavity exceeds the critical size, the cavity cannot efficiently absorb sound energy, which results in its collapse.

The collapse of cavitation bubbles produces intense local heating of temperatures at approximately 5000° C as well as high pressures of about 500 atmospheres. [30] The changes in the cavity size and acoustic pressure throughout the formation, growth, and collapse are illustrated in Figure 1-7. The shock waves produced from the collapse of cavitation bubbles produces high-velocity interparticle collisions. The large-scale vibrations that result from the shock waves provide the force that causes extension and deformation in the chemical species of interest.

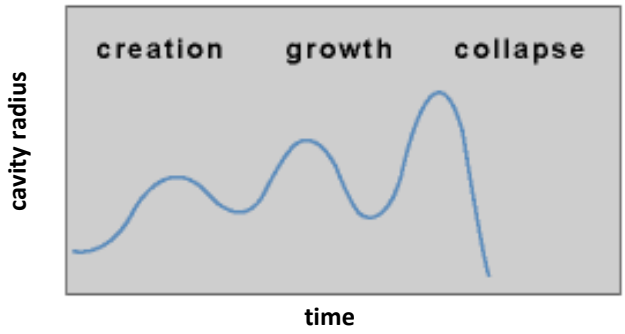

Figure 1-7: Changes in cavity size throughout a typical sonication process. At a certain point during the growth process, the cavity reaches a crtical size. Sizes exceeding the critical size result in the collapse of cavitation bubbles.

Sonochemical methods have been reported extensively as a means to mechanically activate chemical reactions. A particular study focused on using sonication to activate the ring opening of benzocyclobutene (BCB). [31] This reaction is governed by the Woodward-Hoffmann (WH) rules[32,33], which state that the ring opening of BCB should open along a conrotatory pathway for the thermally allowed pathway and a disrotatory pathway for the thermally forbidden pathway. Conrotatory opening refers to both methylene groups rotating in the same direction whereas disrotatory opening refers to both methylene groups rotating in opposite directions. Under mechanochemical conditions, the system is activated along the formally forbidden disrotatory pathway. Specifically, the application of stress using sonochemical methods on *trans*-substituents follows a conrotatory pathway whereas applying stress on *cis*-substituents leads to the system following a disrotatory pathway. As a result, an identical product is formed in violation of the WH rules. The mechanochemical, thermal and photochemical pathways are illustrated in Figure 1-8.

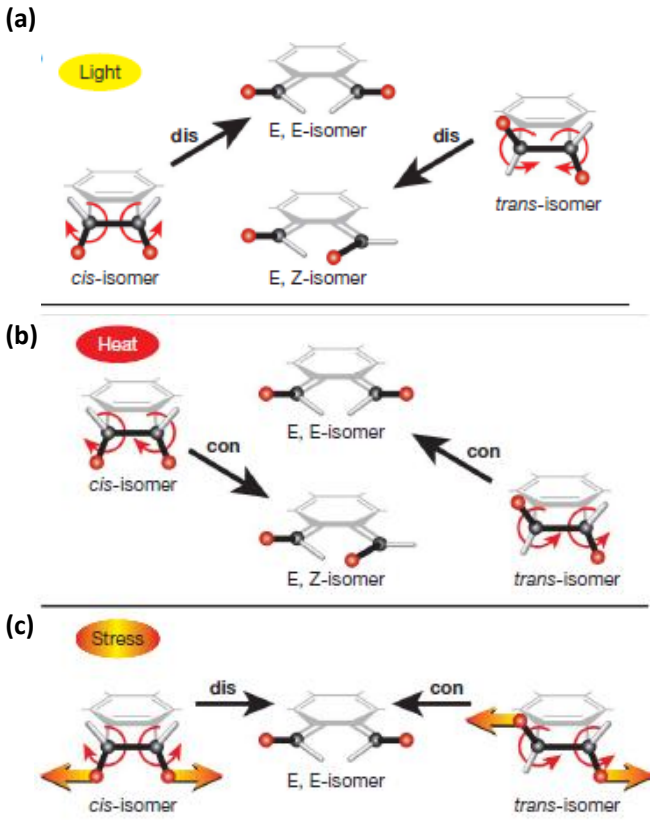

Figure 1-8: Expected reaction pathways of **(a)** thermally forbidden or photochemically allowed and **(b)** thermally allowed ring opening of BCB. Upon activation by light, the WH rules predict that both *cis* and *trans* BCB follow a disrotatory pathway. The stereochemistry is inverted from reactant to product with the *cis* isomer forming the E,E- product and the *trans* isomer forms the E,Z-product. Upon activation by heat, both isomers undergo conrotatory ring opening. The stereochemistry is preserved from reactant to product with the *cis* isomer forming the E,Z-product and the *trans* isomer forming the E,E-product. Under mechanochemical conditions **(c)**, the *cis*-isomer follows a disrotatory ring opening and the *trans* isomer follows a conrotatory opening yielding the identical E,E-product**.**[31]

The results of the sonication experiments demonstrate how mechanical stress can be used to selectively bias the system along particular pathways. The ability to violate the WH rules is fundamentally interesting, and more generally, selectively activating reactions along competing pathways may be of synthetic value. This has motivated several theoretical studies on mechanochemistry. The next section in this chapter will focus on discussing the theoretical models developed to simulate mechanochemical processes.

1.4 Theoretical models

Historically, mechanochemical simulations were performed using the COnstrained Geometries simulate External Force (COGEF)[34] method. This approach is based on imposing a distance constraint between the PPs:

$$\sigma_{ij}(\mathbf{x}) = \left[\mathbf{x}_i - \mathbf{x}_j\right]^2 - {q_0}^2 \tag{1.3}$$

where σ_{ij} is the distance constraint as a function of nuclear Cartesian coordinates $\mathbf{x}$, $\mathbf{x}_i$ is the position of atom i, $\mathbf{x}_j$ is position of atom j, and q_0 is the target distance between the pulling points i and j. The constraint equation (1.3) is satisfied when the calculated distance using atomic positions equals the target length. Imposing the distance constraint into mechanochemical simulations modifies the PES on which the molecule moves:

$$V_{COGEF}(\mathbf{x}, q) = V_{BO}(\mathbf{x}) - F_{int}q(\mathbf{x}) \tag{1.4}$$

where $V_{COGEF}(\mathbf{x}, q)$ is the force-modified potential energy function that arises from imposing a distance constraint on the system, V_{BO} is the Born-Oppenheimer potential energy as a function of all nuclear Cartesian coordinates $\mathbf{x}$ without any constraints, $q(\mathbf{x})$ is the calculated distance between PPs, and F_{int} is the magnitude of the restoring force required to keep the PP separation at the target distance q_0. In general, F_{int} is determined by projecting a force vector whose components correspond to the forces acting on atoms i and j along the vector connecting those atoms. In the COGEF approach, the distance between PPs is the control variable and the

constrained geometry is used to obtain the force acting on the PPs. Mechanical stress is simulated by increasing the distance between PPs at a constant rate.

An alternative method to simulate mechanochemical processes involves applying a constant external force between the two PPs and allowing the distance to change. In this approach, known as External Force is Explicitly Included (EFEI), F_{ext} is treated as the control variable and the optimized geometry is obtained from applying F_{ext} between the two PPs. The differences between how mechanical stress is simulated in both COGEF and EFEI methods are further shown in Figure 1-9.

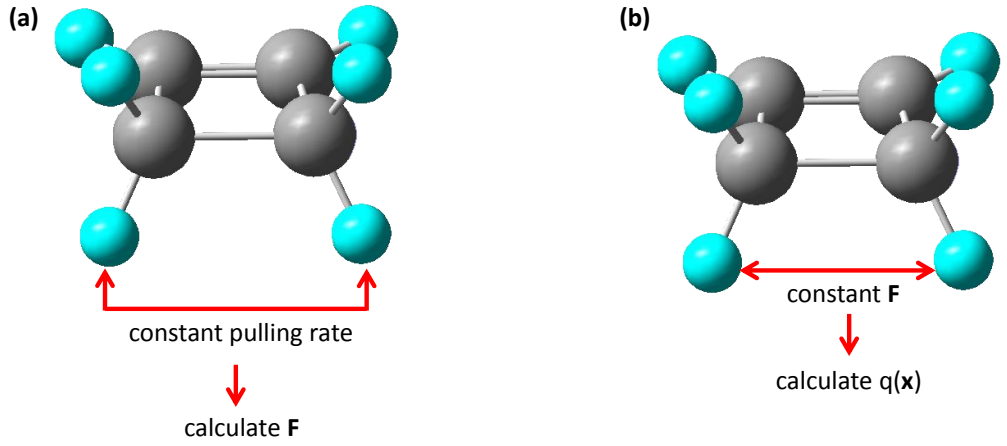

Figure 1 -9: Schematic demonstrating how mechanical stress is simulated using **(a)** COGEF and **(b)** EFEI. Hydrogen atoms in a *cis*-configuration attached the carbon atoms of the scissile bond of cyclobutene are used as PPs in both representations. In COGEF-based simulations, the distance between PPs q(**x**) is increased at a constant rate until it reaches the target value q_0. The force required to keep the distance fixed at q_0 is calculated. In EFEI-based simulations, a constant force is applied between PPs and the distance can be calculated from the optimized structure.

Recent experimental approaches have shown that the force is the control variable and can be applied directly to atoms or functional groups. [35] In force-clamp AFM experiments, properties such as catalytic activity are found to change when subjected to a constant external force. [36,37] Forces can also be applied in an isotensional manner through the use of mechanophores, which convert mechanical energy into force. [38, 39] Mechanophores are force-sensitive groups that can be

incorporated into a material to alter its reaction to stress. An example of such a case is the addition of aliphatic polymer chains onto a benzocyclobutene (BCB) moiety. [40,41] An advantage of using mechanophores is the possibility of avoiding non-specific rupture at forces large enough to break covalent bonds. [42]

The experimental results have motivated further theoretical studies on applying stress using a constant external force. Marx and coworkers[43] have developed a theoretical framework for understanding how the PES is modified from the applied F_{ext} as the control parameter. The force-modified potential energy surface (FMPES) obtained from EFEI-based simulations is defined as:

$$V_{EFEI}(\mathbf{x}, F_{ext}) = V_{BO}(\mathbf{x}) - F_{ext} q(\mathbf{x}) \qquad (1.5)$$

The expression for the FMPES is similar to that of the COGEF-based simulations. The application of F_{ext} directly modifies the PES in EFEI-based simulations whereas it indirectly affects the PES through a structural constraint q_0 in the COGEF-based simulations. At stationary points on the FMPES, the gradient of the potential $\nabla_x V_{EFEI}(\mathbf{x}, F_{ext})$ is equal to zero for fixed values of F_{ext}. As a result, F_{ext} cancels out the internal force, $\mathbf{F} = -\nabla_q V_{BO}(\mathbf{x}_0)$, acting on the PPs at the minimum point $\mathbf{x}_0$. The EFEI approach is often regarded as the correct force-transformed Born-Oppenheimer PES with $\mathbf{x}_0$ (F_{ext}) describing the exact deformation of the molecular structure $\mathbf{x}_0$ as a function of F_{ext}. [43] Important properties such as reactant and transition state (TS) molecular structures as well as activation energies as function of F_{ext} can be evaluated using the EFEI formalism.

1.5 Previous theoretical studies

Several theoretical studies on chemical reactions using both COGEF and EFEI-based simulations have appeared in the literature. [44,45] A recent study focused on investigating the ring opening of cyclobutene along conrotatory and disrotatory pathways using COGEF-based simulations.[46] The authors were motivated by the previous sonication results on the mechanically activated ring opening of BCB along the disrotatory pathway mentioned in Section 1.3. In this study, Car-Parrinello molecular dynamics simulations (CPMD)[47] (see Chapter 2) were used to investigate the ring openings of unsubstituted cyclobutene and ester substituted BCB. The results of the CPMD simulations showed that the ring opening of unsubstituted cyclobutene proceeded through the conrotatory pathway and the ring opening of ethyl substituted cyclobutene proceeded through the disrotatory manner. The details of this study are further discussed in Chapter 3.

A previous theoretical study has used EFEI-based simulations to investigate the mechanochemical response of cyclobutene. [42] In this study, Marx`s formalism was applied to investigate how F_{ext} modifies the PES. This allows one to locate transition states and barrier heights on the FMPES. The simulations were carried out using the Complete Active Space Self-Consistent Field (CASSCF) method[48] (see Chapter 2) with second order perturbation theory corrections CASPT2(4,4) /6-31G(d,p) level of theory.[49,50] The resulting FMPESs for applying a constant F_{ext} between *cis*-PPs and *trans*-PPs are shown in Figure 1-10. [40] The plots show how the energetic profiles for conrotatory and disrotatory minimum energy pathways are affected differently from the application of F_{ext}. The barrier heights for the conrotatory and disrotatory

pathways obtained from applying F_{ext} between *cis*-PPs become nearly equivalent when F_{ext} = 1.5 nN. The FMPES obtained using *trans*-PPs shows that the barrier for the conrotatory pathway decreases with $F_{ext.}$ The barrier for the disrotatory pathway remains largely unaffected from pulling on *trans*-substituents. The results of this study show that the barrier for the disrotatory pathway decreased with increasing F_{ext} when using *cis*-PPs.

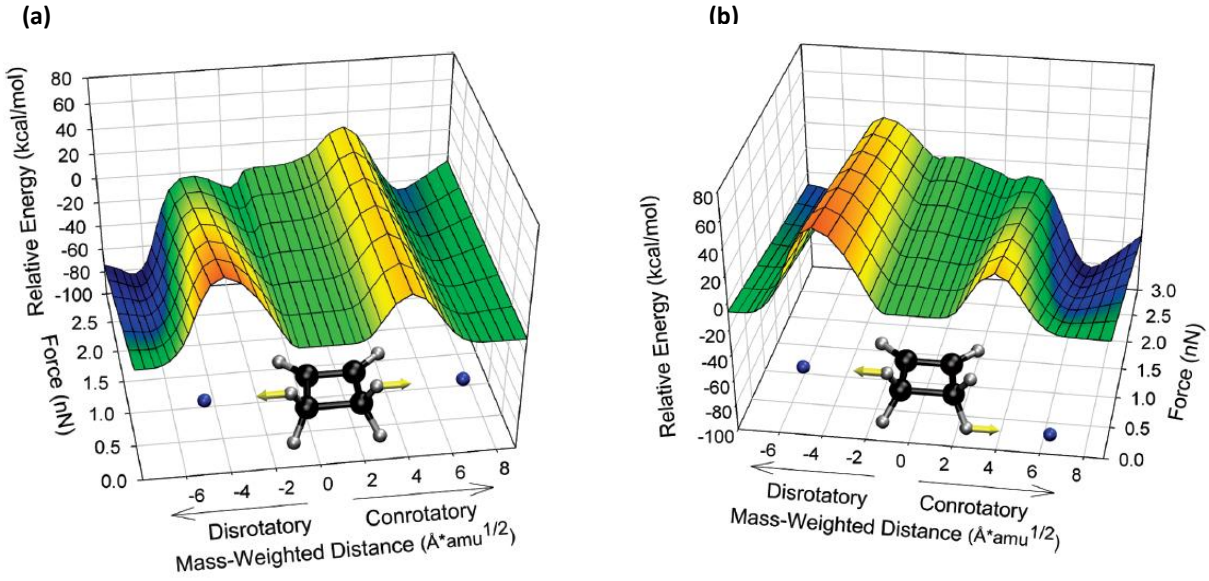

Figure 1-10: Force-modified potential energy surfaces obtained for the ring opening of cyclobutene under mechanochemical conditions with **(a)** *cis*-PPs and **(b)** *trans*-PPs. The barriers for the disrotatory pathway and conrotatory pathway are almost equivalent at 1.5 nN when using *cis*-PPs. The conrotatory barrier decreases steadily with applied F_{ext} and the disrotatory barrier remains unaffected when using *trans*-PPs.

1.6 Objectives of thesis

The previous theoretical studies have used COGEF and EFEI-based simulations to investigate the mechanical response of cyclobutene. These studies have shown that COGEF and EFEI simulations lead to different results for the ring opening of cyclobutene. It would be useful

to understand the origin of this difference, given that the qualitatively different outcomes of these two methods may lead to entirely different interpretations of experimental data and complicate the theoretical prediction of reaction barriers under mechanochemical conditions. Chapter 3 of the thesis reports the results of a study undertaken to identify why COGEF and EFEI methods yield different results for the ring opening of cyclobutene. The results indicate that two factors are at play. First, the FMPESs obtained through COGEF and EFEI methods are very different. In the case of COGEF, a minimum corresponding to the product of disrotatory ring opening does not exist. Meanwhile, the EFEI potential is smoothly transformed through the application of increasing F_{ext} such that the relative kinetics along the conrotatory and disrotatory pathways favour disrotatory opening at high F_{ext}. Second, in molecular dynamics simulations performed according to the COGEF approach, i.e. where the PPs are separated at a constant rate to mimic the application of an external force, the movement of the PPs is too slow at some times and too fast at others compared to the natural motion of the PPs during the reaction performed without constraints. This mismatch between PP motion and reaction kinetics allows the system to explore other pathways. Overall, the results of this study clarify the origin of the qualitative differences in the results of the COGEF and EFEI based simulations of the ring opening of cyclobutene, and indicate more general factors that must be considered when simulating reactions under mechanochemical conditions.

The results from Martinez and colleagues[42] have explained the activation of the ring opening of cyclobutene along the disrotatory pathway in terms of energetics. Specifically, the disrotatory pathway is activated since the barrier is reduced on the FMPES. Ultimately, the WH rules are based on the conservation of orbital symmetry. The typical route that the system has to take to follow a thermally forbidden pathway is to be exposed to irradiation resulting in changes

in the electronic state and orbital occupations. The application of F_{ext} does not interact with orbitals in a direct manner to induce electronic excitations. Therefore, it would be of fundamental value to determine how F_{ext} promotes reactions along pathways that are formally forbidden according to the WH rules. Chapter 4 describes a study taken to explore the changes in electronic structure that occur during pericyclic reactions induced to follow 'forbidden' pathways under mechanochemical conditions. The results demonstrate that the WH rules are indeed broken during these processes, as opposed to a new mechanochemical pathway becoming available. Instead the mechanical work performed on the system through the application of F_{ext} outweighs the underlying changes in electronic structure that disfavour the 'forbidden' processes. These fundamental insights into the interplay between mechanical work and electronic structure likely have broader application in the context using mechanical stresses to activate reactions.

---

[1] Beyer, M.K.; Clausen-Schaumann, H. *Chem. Rev*. **2005**, *105*, 2921-2948.

[2] Gilman, J.J; *Science*, **1996**, *274*, 65.

[3] Krüger, D.; Rousseau, R.; Fuchs, H.; Marx, D.*; Angew. Chem. Int. Ed.* **2003**, *42*, 2251.

[4] Boldyrev, V.V.; Tkáčová, K. *J. Mat. Syn. Proc*. **2000**, *8*, 121-132.

[5] Bridgeman, P.W.; *Rev. Modern. Phys.* **1946**, *18*, 1-93.

[6] Suryanarayana, C. *Non-Equilibrium Processing of Materials*, Pergamon, Oxford, 1999.

[7] Liang, J.; Fernandez, J. *ACS Nano*, **2009**, *3*, 1628-1645.

[8] Borgia, A.; Williams, P.M.; Clarke, J. *Annu. Rev. Biochem*. **2008**, *77*, 101-125.

[9] Sharma, D.; Cao, Y.; Li, H. *Angew. Chem. Int. Ed*. **2006**, *45*, 5633-5638.

[10] Grandbois, M.; Beyer, M.; Rief, M.; Clausen-Schaumann, H.; Gaub, H.E. *Science*, **1999**, *283*, 1727-1730.

[11] Neuman, K.C.; Nagy, A. *Nature Methods*, **2008**, *5*, 491-505.

[12] Ashkin, A. *Phys. Rev. Lett*. **1970**, *24*, 156

[13] Kuyper, C.L.; Chiu, D.T. *Applied Spectroscopy*, **2002**, *56*, 300A-312A.

[14] Grier, D.G.; *Nature*, **2003**, *424*, 810-816

[15] Ashkin, A.; Dziedzic, J.M. *Science*, **1987**, *235*, 1517-1520.

[16] deCastro, M.J.; Fondecave, R.M.; Clarke, L.A.; Schmidt, C.F.; Stewart, R.J. *Nature Cell. Bio.* **2000**, *2*, 724.

[17] Smith, D.E.; Trans, S.J.; Smith, S.B.; Grimes, S.; Anderson, D.L.; Bustamante, C. *Nature*, **2001**, *413*, 748-752.

[18] MacDonald, M.P.; Spalding, G.C.; Dholakia, K.; *Nature*, **2003**, *426*, 421-424.

[19] Yan, J.; Skoko, D.; Marko, J.F.; *Phys, Rev. E*, **2004**, *70*, 011905.

[20] Danilowicz, C.; Greenfield, D.; Prentiss, M.; *Anal. Chem*. **2005**, *77*, 3023-3028.

[21] Charvin, G.; Strick, T.R.; Bensimon, D.; Croquette, V. *Annu. Rev. Biophys. Biomol. Struct*. **2005**, *34*, 201-219.

[22] Strick, T.R.; Croquette, V.; Bensimon, D.; *Nature*, **2000**, *404*, 901-904.

[23] Walter, N.G.; Huang, C.Y.; Manzo, A.J.; Sobhy, M.A. *Nature Methods*, **2008**, *5*, 475-489.

[24] Yang, Q.Z.; Huang, Z.; Kucharski, T.J.; Khvostichenko, D.; Chen, J.; Boulatov, R.; *Nature Nanotech*. **2009**, *4*, 302-306.

[25] Tani, K.; Stoltz, B.M.; *Nature*, **2006**, *441*, 731-734.

[26] Berkowski, K.L.; Potisek, S.L.; Hickenboth, C.R.; Moore, J.S. *Macromolecules*, **2005**, *38*, 8975-8978.

[27] Price, G.J.; *Adv. Sonochem*. **1990**, *1*, 231-287.

[28] Suslick, K.S.; *Science*, **1990**, *247*, 1439-1445.

[29] Belova, V.; Shchukin, D.G.; Gorin, D.A.; Kopyshev, A.; Möhwald, H. *Phys. Chem. Chem. Phys*. **2011**, *13*, 8015-8023.

[30] Suslick, K.S.; Hammerton, D.A.; Cline, R.E.; *J. Am. Chem. Soc.* **1986**, *108*, 5641

[31] Hickenboth, C.R.; Moore, J.S.; White, S.R.; Sottos, N.R.; Baudry, J.; Wilson, S.R. *Nature*, **2007**, *446*, 423-427.

[32] Woodward, R.B.; Hoffmann, R.; *Angew. Chem. Int. Ed.* **1969**, *8*, 781-853.

[33] Woodward, R.B.; Hoffmann, R.; *J. Am. Chem. Soc.* **1965**, *87*, 395-397.

[34] Beyer, M.K. *J. Chem. Phys*. **2000**, *112*, 7307-7312.

[35] Kersey, F.R.; Yount, W.C.; Craig, S.L.; *J. Am. Chem. Soc.* **2006**, *128*, 3886-3887.

[36] Wiita, A.P.; Perez-Jimenez, R.; Walther, K.A.; Gräter, F.; Berne, B.J.; Holmgren, A.; Sanchez-Ruiz, J.M.; Fernandez, J.M. *Nature*, **2007**, *450*, 124-127.

[37] Wiita, A.P.; Ainavarapu, S.R.K.; Huang, H.H.; Fernandez, J.M.; *Proc. Natl. Acad. Sci.* USA **2006**, *103*, 7222-7227.

[38] Percec, V.; Rosen, B.M. *Nature*, **2007**, *446*, 381-382.

[39] Ribas-Arino, J.; Shiga, M.; Marx, D. *J. Am. Chem. Soc.* **2010**, *132*, 10609-10614.

[40] Potisek, S.L.; Davis, D.A.; Sottos, N.R.; White, S.R.; Moore, J.S. *J. Am. Chem. Soc.* 2007, 129, 13808-13809.

[41] Yang, Q.Z.; Huang, Z.; Kucharski, T.J.; Khvostichenko, D.; Chen, J.; Boulatov, R. *Nat. Nanotechnol*. **2009**, *4*, 302-306.

[42] Ong, M.T.; Leiding, J.; Tao, H.; Virshup, A.M.; Martinez, T.J. *J. Am. Chem. Soc*. **2009**, *131*, 6377-6379

[43] Ribas-Arino, J.; Shiga, M.; Marx, D. *Angew. Chem. Int. Ed*. **2009**, *48*, 4190-4193.

[44] Lenhardt, J.M.; Ong, M.T.; Choe, R.; Evenhuis, C.R.; Martinez, T.J.; Craig, S.L. *Science*, **2010**, *329***,** 1057.

[45] Aktah, D.; Frank, I.*; J. Am. Chem. Soc*. **2002**, *124***,** 3402.

[46] Friedrichs, J.; LüBmann, M.; Frank, I. *ChemPhysChem*, **2010**, *11*, 3339-3342

[47] Car, R.; Parrinello, M. *Phys. Rev. Lett.* **1985**, *55*, 2471

[48] Roos, B.O. *Adv. Chem. Phys*. **1987**, *69*, 399.

[49]Andersson, K.; Malmquist, P.A.; Roos, B.O.; Sadlej, A.; Wolinski, K. *J. Phys. Chem*. **1990**, *94*, 5483.

[50] Andersson, K.; Malmquist, P.A.; Roos, B.O. *J. Chem. Phys*. **1992**, *96*, 1218.

Chapter 2: Computational Methods

2.1 Introduction

Chemical simulations were performed to investigate the effect of applied F_{ext} on the ring opening of cyclobutene along conrotatory and disrotatory pathways. Static quantum chemical (QC) calculations were used to obtain optimized geometries and vibrational frequencies of minima on the force-modified potential energy surface (FMPES). Sections 2.2 and 2.3 describe the concept of the potential energy surface (PES) and the effect of force on the thermodynamics and kinetics of a reaction. Locating minima on the PES involves performing geometry optimizations, which are discussed in Section 2.4. Characterizing the structures on the PES can be accomplished by calculating vibrational frequencies as described in Section 2.5. Molecular dynamics (MD) simulations, which are described in Section 2.6, were performed to explore the PES in a physically meaningful manner. MD simulations were performed to investigate how to properly mechanochemical processes with two methods: External Force is Explicitly Included (EFEI) and COnstrained Geometries simulate External Force (COGEF). Mechanical stress is simulated in the EFEI method by applying a constant external force, F_{ext}, between two atoms in a molecule that serve as pulling points (PPs) and allowing those atoms to move to maintain that force. In MD simulations using the COGEF method, a target PP separation is defined and increased over time to mimic the application of an external force. The implementation of both of these methods is discussed in Section 2.7. The static and MD simulations were performed using the CASSCF method[1]. Section 2.8 describes the basis sets used in the calculations. The CASSCF method is an extension of the Hartree-Fock method, which is described in Section 2.9. Finally, the details of the CASSCF method are discussed in Section 2.10.

2.2 Potential Energy Surfaces

In computational chemistry, energy calculation methods are used to relate the energy of a molecule to its geometry. This is used to construct the potential energy surface (PES). Every energy-structure pair corresponds to a point on the PES. The structure-energy relationship is fundamental to computational chemistry and apparent from the total energy or Hamiltonian operator, $\hat{H}$:

$$\hat{H} = -\sum_{i=1}^{N} \frac{\hbar^2}{2m_i} \nabla_i^2 - \sum_{I=1}^{N} \frac{\hbar^2}{2M_I} \nabla_I^2 - \sum_{I=1}^{M} \sum_{i=1}^{N} \frac{Z_I e^2}{4\pi\varepsilon_0 r_{Ii}} + \sum_{i=1}^{N-1} \sum_{j>1}^{N} \frac{e^2}{4\pi\varepsilon_0 r_{ij}} + \sum_{i=1}^{N-1} \sum_{j>1}^{N} \frac{Z_I Z_J}{4\pi\varepsilon_0 r_{IJ}} \qquad (2.1)$$

where $\hbar$ is the reduced Planck constant ($h/2\pi$), m_i and M_I are the masses of the electron and nuclei respectively, ∇^2 is the Laplacian operator, Z_I and Z_J are nuclear charges, e is the charge of the electron, ε_0 is the permittivity of free space, r_{ij} is the electron-electron distance, r_{IJ} is the nuclear-nuclear distance, and r_{iI} is the electron-nuclear distance. The first two terms represent the electronic and nuclear kinetic energies, respectively. The last three terms represent the potential energy for the system. The full molecular Hamiltonian accounts for nuclear and electronic motions as well as the electrostatic interaction between all particles. Since the nuclei are much heavier than the electrons, their velocities are much slower. As a result, the electrons can adjust instantaneously to changes in nuclear positions. This implies that the total wave function can be separated into nuclear and electronic components:

$$\Psi_{tot}(\mathbf{r},\mathbf{R}) = \Psi_{nuc}(\mathbf{R})\Psi_{elec}(\mathbf{r};\mathbf{R}) \qquad (2.2)$$

where **r** represents the electronic coordinates and **R** represents the nuclear coordinates. The electronic wave function only depends parametrically on the positions of the nuclei, not their momenta. The separation of the total wave function into nuclear and electronic components is referred to as the Born-Oppenheimer approximation. The Born-Oppenheimer approximation is generally employed to construct the PES for a chemical system. The Born-Oppenheimer PES is constructed by solving the electronic Schrödinger equation for a large number of geometries[2]:

$$\hat{H}_{elec}\Psi_{elec}(\mathbf{r};\mathbf{R}) = E_{elec}\Psi_{elec}(\mathbf{r};\mathbf{R}) \qquad (2.3)$$

where $\hat{H}_{elec}$ is the electronic Hamiltonian and E_{elec} is the electronic energy. The potential energy of a given structure is obtained by adding the nuclear-nuclear repulsion term, which is a constant from the perspective of the electrons, to the electronic energy. For a system with N atoms, there are $3N$ Cartesian coordinates that define the geometry. Three of the coordinates describe the translation of the molecule in x, y, and z directions and another three to describe the rotation of the molecule with respect to three axes. This results in $3N$-6 coordinates for non-linear molecule and $3N$-5 coordinates for linear molecules to describe the internal movement of the nuclei. Constructing the PES for a particular molecule allows one to identify reactant and product structures as well as the transition state structure. The reactant and product structures correspond to local minima on the PES whereas the transition state structure is a first-order saddle point that connects the two minima. A minimum is defined as a point of the PES, where all first derivatives of energy with respect to atomic positions are zero and the second derivatives of the energy with respect to positions are positive in all directions. For a first-order saddle point, the second derivative of the energy with respect to the reaction coordinate is negative whereas the second

derivatives are positive in all other directions. The reaction coordinate is defined as a geometric parameter that results in the lowest energy pathway from reactants to products.

In mechanochemical simulations performed according to COGEF and EFEI formalisms, the Born-Oppenheimer PES is modified by including the mechanical work term as shown in Eq. (2.4).

$$V(\mathbf{x}, F_{ext}) = V_{BO}(\mathbf{x}) - Fq(\mathbf{x}) \tag{2.4}$$

where $V(\mathbf{x}, q)$ is the force-modified potential energy function, V_{BO} is the Born-Oppenheimer potential energy as a function of all nuclear coordinates $\mathbf{x}$ without any constraints, $q(\mathbf{x})$ is the calculated distance. In the COGEF method, F corresponds to the force that must be applied to keep the $q(\mathbf{x})$ at its target value. The magnitude of this force exactly equals the restoring force, F_{int}, acting along the constrained coordinate. In the EFEI method, F corresponds to the magnitude of an external force applied along the vector defined by $q(\mathbf{x})$.

The reactants, products, and transition state structures are located at stationary points on the FMPES. Since the Born-Oppenheimer potential energy and calculated distance between PPs are functions of coordinates, the first and second derivatives of the force-modified potential energy can be evaluated. Evaluating the first and second derivatives is useful for performing the geometry optimizations, vibrational frequency calculations, and molecular dynamics (MD) simulations as discussed in further sections.

2.3 Effect of Force on Thermodynamics and Kinetics of a Reaction

The positions of the reactant, product, and transition state structures on a PES can provide information on the relative stability of molecules as well as the rate at which a reaction occurs. The change in enthalpy difference of reactants and products, ΔH, can be used to evaluate other thermodynamic properties such as the Gibbs free energy change, ΔG and the entropy change, ΔS:

$$\Delta H = \Delta G - T\Delta S \tag{2.5}$$

where T is the temperature. In the absence of F_{ext}, the change in Gibbs free energy upon moving from reactants, R, to products, P, can be expressed as:

$$\Delta G(F_{\text{ext}} = 0) = \Delta G^0 + k_B T \ln[R]/[P] \tag{2.6}$$

where ΔG^0 is the standard state free energy change, k_B is Boltzmann`s constant, and [R] and [P] are reactant and product concentrations. The application of F_{ext} tilts the free energy surface along the mechanical reaction coordinate, which is the distance between PPs, $q(\mathbf{x})$. The free energy surface is altered by an amount that is linearly dependent on $q(\mathbf{x})$.[3] As a result, the change in free energy in the presence of F_{ext} can be expressed as

$$\Delta G(F_{\text{ext}}) = \Delta G^0 + k_B T \ln[R]/[P] - F_{ext} q(\mathbf{x}) + \Delta G_{stretch}^{R\to P}(F_{\text{ext}}) \tag{2.7}$$

At equilibrium, the Gibbs free energy change is zero. Eq. (2.7) becomes

$$\Delta G^0 - F_{ext}\Delta q(\mathbf{x}) + \Delta G_{stretch}^{R\to P}(F_{ext}) = -k_B T \ln K_{eq}(F_{ext}) \qquad (2.8)$$

where K_{eq} is the equilibrium constant and $\Delta G_{stretch}^{R\to P}(F_{ext})$ accounts for the Gibbs free energy change that results from the shift in minima of reactant and product states on the unmodified free energy surface to the force-modified free energy surface. This concept is further illustrated in Figure 2-1.

Eq. (2.8) shows that the equilibrium constant under mechanochemical conditions depends exponentially on the applied F_{ext}. Hence, by applying F_{ext}, one can alter the equilibrium of the reaction to increase or decrease the populations of molecules in reactant and product states.

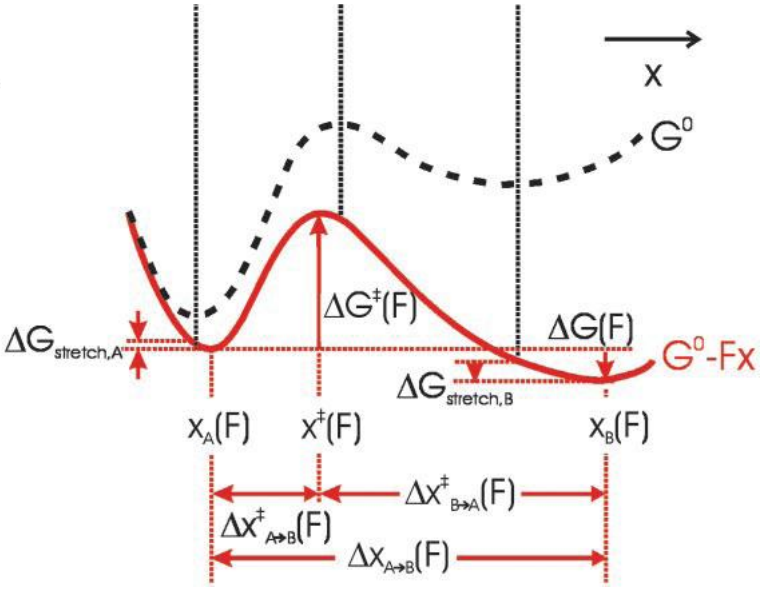

Figure 2-1: The effect of applied F_{ext} on the Gibbs free energy curve for a reaction. The dashed black curve represents the Gibbs free energy in the absence of F_{ext} and the solid red curve represents the Gibbs free energy from the application of F_{ext}. The application of F_{ext} shifts the position of reactant (x_A), transition state ($x^{\ddagger}$), and product (x_B) structures. The Gibbs free energy of the product state, B is lowered to a greater extent than reactant state, A. As a result, the rate of the forward reaction and the population of state B are increased.[3]

For a unimolecular reaction that involves the conversion of reactants *R* to products *P*, the rate of formation of products can be described by:

$$\frac{d[P]}{dt} = k[R]^n \tag{2.9}$$

where [R] and [P] represent the concentrations of reactant and product respectively, *k* is the rate constant for the reaction, and *n* is a stoichiometric coefficient if the reaction is elementary. The rate constant can be calculated using the Arrhenius equation:

$$k = Ae^{-\Delta E^{\ddagger}/RT} \tag{2.10}$$

where *A* is the Arrhenius pre-exponential factor, $\Delta E^{\ddagger}$ is the activation energy for the reaction, *R* is the universal gas constant, and *T* is the temperature. The Arrhenius equation is reliable for calculating rate constants when there is a temperature dependence on reaction rates. The activation energy is similar to the reaction barrier, $\Delta E_0^{\ddagger}$, which is the potential energy barrier that separates reactant and product minima. The activation energy, however, is an experimentally derived parameter that depends on the temperature of the reaction.

The effect of applied F_{ext} on the kinetics of a reaction was first described by Bell (1978). [4] In this work, a theoretical framework was developed for understanding the adhesion between cells. The model proposed that the application of F_{ext} lowers the activation energy of a reaction by

$$\Delta E_{Bell}^{\ddagger}(F_{ext}) = \Delta E_0^{\ddagger} - F_{ext} q(\mathbf{x}) \tag{2.11}$$

where $\Delta E_0^{\ddagger}$ is the barrier for the reaction in the absence of F_{ext} and $\Delta E_{Bell}^{\ddagger}(F_{ext})$ is the barrier for the reaction in the presence of F_{ext}. This notion that the application of F_{ext} lowers the activation energy for a reaction was also explored by Zhurkov (1965).[5] In this study, a modified version of the Arrhenius equation was proposed for describing the mechanical degradation of polymers:

$$k(F_{ext}) = ke^{-(\Delta E_0^{\ddagger} - W)/RT} \tag{2.12}$$

where $k(F_{ext})$ is the rate constant for the reaction under mechanochemical conditions and W is the work performed on the system. Eq. (2.12) shows that performing work on the system lowers the activation energy and therefore increases the rate of the reaction.

Other kinetic models are based on transition state theory (TST)[6]. TST makes three important assumptions: the transition state corresponds to a saddle point on the reaction coordinate and is used to determine the rate of the reaction, the motion of the system at a saddle point along a particular reaction coordinate can be treated as a free translational motion and expressed using kinetic theory[7], and the transition state is in quasi-equilibrium with an equilibrium constant

$$K^{\ddagger} = \frac{[TS]^{\ddagger}}{[R]} \tag{2.13}$$

where $[TS]^{\ddagger}$ is the concentration of the transition state species. The rate of formation of the products can be expressed as

$$\frac{d[P]}{dt} = k^{\ddagger}[TS] = k^{\ddagger}K^{\ddagger}[R] \tag{2.14}$$

where $k^{\ddagger}$ is the rate constant for the conversion of transition state to products. The rate constant is directly proportional to the frequency of the vibrational mode that corresponds to the transition state converting to products:

$$k^{\ddagger} = \kappa\nu \tag{2.15}$$

where ν is the frequency of the vibrational mode and κ is a proportionality constant. The equilibrium constant is related to the Gibbs free energy through

$$K^{\ddagger} = \frac{k_B T}{h\nu} e^{\frac{-\Delta G^{\ddagger}}{RT}} \tag{2.16}$$

Combining equations (2.15) and (2.16) yields a new rate constant:

$$k = k\ddagger K^{\ddagger} = \kappa \frac{k_B T}{h} e^{\frac{-\Delta G^{\ddagger}}{RT}} \tag{2.17}$$

As discussed above, the application of F_{ext} alters the positions of the minima and transition state structures on the Gibbs free energy surface. From Eq. (2.17), a decrease in the Gibbs free energy barrier for the reaction will result in an increase in the rate constant and thus increase the rate of the reaction. Using Eq. (2.5), the rate constant can be expressed in terms of the enthalpy and entropy change of a reaction:

$$k = \kappa \frac{k_B T}{h} e^{\frac{\Delta S^{\ddagger}}{R}} e^{\frac{-\Delta H^{\ddagger}}{RT}} \tag{2.18}$$

It is assumed in TST that the entropy changes in a reaction are not significant in a relative sense. The enthalpy changes in a reaction should resemble potential energy changes. In this thesis, the mechanochemical effects on the kinetics of a reaction will be examined by calculated potential energy barriers. Furthermore, one would expect that a decrease in the potential energy barrier leads to an increase in reaction rate

2.4 Geometry Optimizations

The thermodynamics and kinetics of a chemical reaction are based on the positions of structures on the PES and the associated energies. The location of structures on the PES involves performing a geometry optimization. A geometry optimization is the most common type of calculation performed in computational chemistry. This calculation involves locating minima and transition state structure on the PES. Obtaining the geometries and energies of minima and transition state structures allows one to determine reaction mechanisms with associated energetics and the preferred geometries for calculating other molecular properties. Searching for these structures requires locating stationary points on the PES. A stationary point is defined as a

point on the PES in which the internal forces acting on the nuclei are zero. The basic procedure in a geometry optimization is to start with an initial guess structure of molecular species, i.e. reactant, product or transition state, and update the atomic positions iteratively until the forces on the nuclei are very small. A common type of optimization procedure used in computational chemistry codes is the Newton-Raphson method. [8] In this procedure, the geometry is updated according to the expression

$$\mathbf{q}_{i+1} = \mathbf{q}_i - \mathbf{H}_i^{-1}\mathbf{g}_i \tag{2.19}$$

where $\mathbf{q}_{i+1}$ and $\mathbf{q}_i$ are column vectors containing 3N coordinates that define the molecular geometry, $\mathbf{g}_i$ is a column vector of 3N first derivatives of the energy with respect to coordinate $\mathbf{q}_i$ and $\mathbf{H}_i$ is the Hessian matrix that contains 3N x 3N second derivatives of the energy with respect to Cartesian coordinates. The first derivatives represent the forces on the nuclei and can be calculated analytically by a computational chemistry program. The second derivatives, however, are too expensive calculated analytically and are generally estimated during the optimization procedure. Once the geometry is updated, the Hessian matrix is updated using the expression

$$\left(\frac{\partial^2 E}{\partial q_a q_b}\right)_i \approx \frac{\Delta(\partial E / \partial q_b)_i}{\Delta q_a} \tag{2.20}$$

This procedure is repeated until the convergence criteria are satisfied. The geometry optimization is converged when all first derivatives and displacements are small and close to zero. For most computational chemistry codes, the maximum force on the nuclei should be less than 4.5 x 10^{-4}

Hartree / Bohr.[9] In this thesis, geometry optimizations are performed to locate minima and transition state structures on the FMPES. Intrinsic reaction coordinate (IRC) calculations are also performed to map out certain reaction pathways. IRC calculations involve starting with a system corresponding to a transition state and following the minimum energy path (MEP) in each direction from the transition state until the stationary points on either side of the transition state are reached. Ultimately, these calculations generate the MEP on the potential energy surface that connects the reactants, transition state, and products for a given reaction.

2.5 Frequency Calculations

Vibrational frequencies are useful for characterizing the nature of stationary points on the PES as well as evaluating properties such as zero-point corrected energies and vibrational partition functions. A vibrational frequency calculations involves first generating the Hessian matrix, **H**, for the system, which corresponds to a matrix containing the second derivatives of the potential energy with respect to nuclear positions. **H** can then be used to obtain normal modes, which correspond to the collective vibrational motions of the atoms, and the force constants of the modes. To do this, **H** is transformed into a product of three matrices:

$$\mathbf{H} = \mathbf{PKP}^{-1} \tag{2.21}$$

where **P** is a square matrix with column vectors containing eigenvectors that are the normal modes and **K** is a diagonal matrix with the diagonal elements correspond to eigenvalues that are the force constants. The force constants can be related to the vibrational frequencies using the harmonic oscillator approximation for a diatomic molecule:

$$\nu = \frac{1}{2\pi}\left(\frac{k}{\mu}\right)^{1/2} \tag{2.22}$$

where μ is the reduced mass of the vibrational mode, ν is the frequency, and k is the force constant. The matrices **P** and **K** are useful for visualizing normal modes and characterizing stationary points. For minima, all diagonal elements of **K** are positive, which results in all positive frequencies. For a transition state structure, one diagonal element of **K** is negative. As a result, the frequency that is associated with a negative force constant is imaginary. The normal mode with the imaginary frequency corresponds to the motion of the molecule along the reaction coordinate.

2.6 Molecular Dynamics Simulations

Static calculations such as geometry optimization and IRC allow one to explore a limited portion of the PES. Locating minima and saddle points on the PES during a geometry optimization is carried out by following a series of structures, which have no physical meaning. Performing MD simulations explores the PES in a physically meaningful way by studying how systems evolve over time. In MD simulations, nuclei are treated as classical particles that obey Newton's equations of motion:

$$\mathbf{F}_i = m_i \mathbf{a}_i = -\frac{\partial V}{\partial \mathbf{r}_i} \tag{2.23}$$

where $\mathbf{F}_i$, m_i, $\mathbf{r}_i$, and $\mathbf{a}_i$ are the force, mass, position, and acceleration, respectively, of particle *i*. The potential energy, *V*, for the system can be obtained either through force field methods such as bond stretching, angle bending, and torsions or through quantum chemical calculations. The latter, known as *ab initio* or first-principles MD simulations, is used to evaluate the potential energy function in the MD simulations performed in this thesis.

Solving Newton's equations of motion by integrating the forces yields trajectories that contain the motions of the atoms over many time steps. Newton's equation of motion cannot be directly solved for systems with more than two atoms. As such, Verlet integration is used to numerically predict changes in atomic positions over time. Standard Verlet integration involves updating the position of the atoms for a time step, Δt according to the expression

$$r_i(t+\Delta t) = 2r_i(t) - r_i(t-\Delta t) + a_i(t)\Delta t^2 \qquad (2.24)$$

The standard Verlet algorithm is based on a Taylor expansion of updating the positions forward and backwards in time. The velocities of the atoms are not directly included in this algorithm. Instead, they are calculated numerically through differences in atomic positions:

$$v_i(t) = \frac{r_i(t+\Delta t) - r_i(t-\Delta t)}{2\Delta t} \qquad (2.25)$$

Velocities are needed in the algorithm for calculating the temperature and determining the total energy of the system. One of the main disadvantages of using standard Verlet integration is that the positions and velocities are not calculated at the same time. As a result, this complicates evaluating the total energy as well as controlling the temperature of the system. For this reason,

the velocity Verlet algorithm is generally employed in MD simulation to numerically predict changes in atomic positions. In this algorithm, the positions and velocities are updated according to the expressions

$$\mathbf{r}_i(t+\Delta t) = \mathbf{r}_i(t) + \mathbf{v}_i(t)\Delta t + 0.5\mathbf{a}_i(t)\Delta t^2 \tag{2.26}$$

$$\mathbf{v}_i(t+\Delta t) = \mathbf{v}_i(t) + 0.5(\mathbf{a}_i(t) + \mathbf{a}_i(t+\Delta t))\Delta t \tag{2.27}$$

The velocity Verlet algorithm provides physically meaningful trajectories because the positions and velocities are evaluated at each time step. The initial positions and velocities are provided for the atoms at the onset of the MD simulations. The starting structure is usually obtained from a previous geometry optimization. The velocities are selected at random using a Maxwell-Boltzmann distribution function:

$$f(v) = \left(\frac{m}{2\pi k_B T}\right)^{3/2} \exp\left(-\frac{1}{2} m v^2 / k_B T\right) \tag{2.28}$$

The next step in the MD simulation is to re-scale the initial velocities to keep the temperature of the system in a given range. This involves defining a target temperature and an allowed range for this temperature. If the temperature is outside the range, the velocities are re-scaled uniformly using the expression

$$v_i^{rescaled} = v_i^{orig} \sqrt{\frac{T_{\text{target}}}{T_{current}}} \tag{2.29}$$

Although velocity re-scaling is an effective method of keeping the temperature in a given range, when the temperature ventures outside the desired range it is reset to the desired temperature by uniformly scaling all atomic velocities by the same factor. Thermostats are often used to correct temperature fluctuations for the entire systems, in which the atomic velocities are not scaled uniformly. Some of the common thermostats employed in MD simulation are the Berendsen[10], Anderson[11], and Nosé-Hoover (NH)[12,13] thermostats. NH thermostats are used for the MD simulations performed in this thesis. In the NH thermostat, the system is coupled to a heat bath that adds or removes energy that results in temperature fluctuations consistent with the canonical ensemble. The heat bath is considered an integral part of the system by adding a time-scaling parameter $\boldsymbol{s}$ that is associated with a mass $\boldsymbol{Q}$. The magnitude of $\boldsymbol{Q}$ determines the coupling between the heat reservoir and the real system. As such, the value of $\boldsymbol{Q}$ influences the temperature fluctuations. The value of $\boldsymbol{s}$ determines the extent to which the timescale in the extended system is stretched by according to the expression:

$$dt = \boldsymbol{s}dt \tag{2.30}$$

The effectiveness of the NH thermostat depends on the value of $\boldsymbol{Q}$. The value of $\boldsymbol{Q}$ should be chosen so that the oscillations of the thermostat are equivalent to the oscillations of the real system. Once the temperature fluctuations are controlled through re-scaling and thermostats, the system is allowed to equilibrate at the simulation conditions for a significant period of time. For the MD simulations performed, the system was equilibrated in canonical (NVT) ensemble. In the

canonical ensemble, the total number of particles *N*, the volume *V*, and the temperature *T* are held constant throughout the simulation. Once the system is equilibrated, the velocity Verlet algorithm is used to update the positions and velocities over time.

2.7 Implementation of COGEF and EFEI-based Simulations

For the COGEF-based MD simulations, mechanical stress is simulated by increasing the distance between PPs at a constant rate. This is accomplished by imposing a distance constraint between the PPs. The constraint is enforced in the simulation using the method of Lagrange multipliers. In most quantum chemical software packages, the RATTLE algorithm[14] is used as an iterative procedure to update the position of atoms over time with the constraint included. In the RATTLE algorithm, the total force acting on the system is

$$m_i \mathbf{a}_i = \mathbf{F}_i + \mathbf{G}_i \tag{2.31}$$

where $\mathbf{F}_i$ is the force due to intermolecular and intramolecular interactions that are not associated with the constraint and $\mathbf{G}_i$ is the force that must be applied to atom *i* due to satisfy the constraint. The magnitude of this force corresponds to the *F* in Eq. (2.4), and is given by:

$$\mathbf{G}_i = -\lambda(t)\mathbf{r}_{ij} \tag{2.32}$$

where $\mathbf{r}_{ij} = |\mathbf{r}_i - \mathbf{r}_j|$ is a vector defined by the distance and direction between the two atoms involved in the constraint, and λ is a Lagrange multiplier that must be determined to obtain the

force that is required to keep the distance between PPs fixed at q_0. The positions in the RATTLE algorithm are updated according to

$$\mathbf{r}_i(t+\Delta t) = \mathbf{r}_i(t) + \Delta t \mathbf{v}_i(t) + (\Delta t^2 / 2m_i)\left[\mathbf{F}_i(t) - 2\lambda(t)\mathbf{r}_{ij}(t)\right] \tag{2.33}$$

and the updated velocities are given by

$$\mathbf{v}_i(t+\Delta t) = \mathbf{v}_i(t) + (\Delta t / 2m_i)\begin{Bmatrix}\left[\mathbf{F}_i(t) - 2\lambda(t)\mathbf{r}_{ij}(t)\right] \\ \times\left[\mathbf{F}_i(t+\Delta t) - 2\lambda(t+\Delta t)\mathbf{r}_{ij}(t+\Delta t)\right]\end{Bmatrix} \tag{2.34}$$

The Lagrange multiplier is chosen such that the calculated distance between PPs equals the target length. An acceptable tolerance is introduced into the simulations. If the initial chosen constraint differs from the target length by a value less than the acceptable tolerance, then a new constraint must be selected. If not, the positions are updated according to Eq. (2.33). The next step in the algorithm is to compute the velocities of the atoms at time $t+\Delta t$. The dot product of $\mathbf{r}_{ij}(t+\Delta t)$ and $\mathbf{v}_{ij}(t+\Delta t)$ is calculated. If the dot product differs significantly from zero by an acceptable tolerance then a new constraint must be selected. If not, the velocities are updated according to Eq. (2.34). The above procedure is repeated until the chosen distance constraint converges to the target length.

In the EFEI-based MD simulations, mechanical stress is simulated by applying a constant force between the PPs. The implementation of the EFEI approach involves calculating the vector that connects the two PPs to obtain the distance and the mechanical work term, $F_{ext}q(\mathbf{x})$. F_{ext} is

provided to the program as a number and the program projects this force along the vector connecting the PPs. The components of the resulting force vector are then added to the forces acting on the PPs due to their positions on the Born-Oppenheimer surface to obtain the total forces acting on these atoms. The geometry is then optimized with a new distance between PPs and a new energy. Preliminary calculations based on the EFEI formalism have shown that the application of F_{ext} can significantly lower the energetics associated with stretching a carbon-carbon bond (Fig. 2-2).

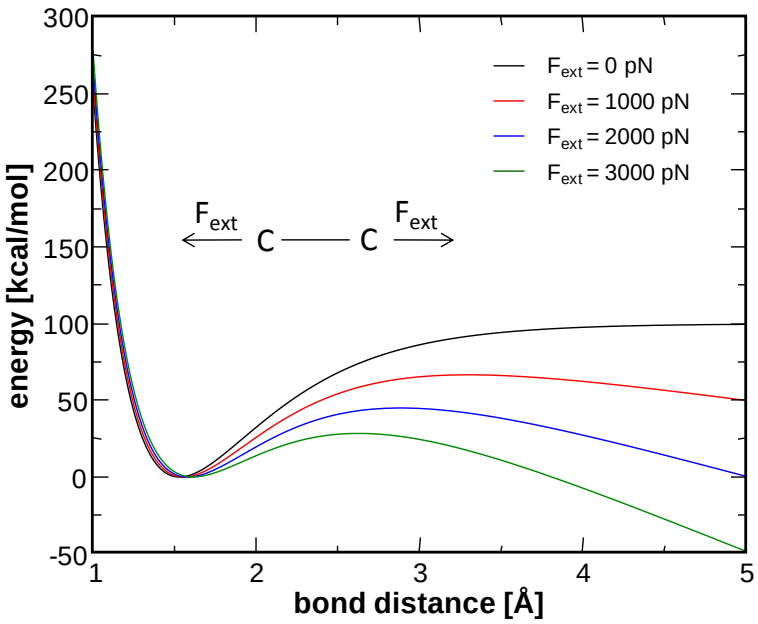

Figure 2-2: Energy as a function of carbon-carbon length for several values at F_{ext} under the EFEI formalism. The carbon-carbon bond length is modeled using a Morse potential. As the value of F_{ext} increases, the barrier for bond dissociation also decreases.

The data shown in Figure 2-2 demonstrates that the application of F_{ext} in the context of the EFEI formalism does not significantly affect the energetics of the system at the equilibrium bond length. The effect of force is more apparent at longer bond lengths, in which the barrier for the dissociation of carbon-carbon bond decreases with increased applied F_{ext}.

2.8 Molecular Orbitals and Basis Sets

In computational chemistry, *ab initio* methods attempt to calculate the total energy of a system by solving the electronic Schrödinger equation without fitting parameters to experimental data. Many different approximation methods exist for solving the electronic Schrödinger equation. One approximation that is common to nearly all *ab initio* methods is the use of a basis set. A basis set is a set of functions that are used to generate molecular orbitals. The molecular orbitals can be expanded as a linear combination of basis functions:

$$\chi_i(\mathbf{x}) = g(w)\sum_{v=1}^{K} c_{vi}\phi_v(\mathbf{r}) \qquad (2.35)$$

where χ_i represents the molecular orbitals as a function of electronic coordinates **x**, *g(w)* is an artificial spin function introduced to account for the fact that molecular orbitals depend on spin coordinates *w*, ϕ_v represent the atomic basis functions as a function of spatial coordinates **r**, c_{vi} are the coefficients that indicate the contribution of each basis function to the molecular orbital, *v* is the index of the basis function, and *K* is the total number of basis function. A molecular orbital can be thought of as an unknown function in the infinite coordinate system that is spanned by the complete basis set. Increasing the number of functions in a basis set results in a better representation of the molecular orbitals. This section will focus on discussing the various types of basis functions with an emphasis on atom-centered functions, which are used in the calculations performed in this thesis.

There are two main types of atom-centered basis functions that are employed in electronic structure calculations: Slater-type orbitals (STOs)[15] and Gaussian type orbitals (GTOs)[16]. STOs take the form of

$$\phi_{\varsigma,n,l,m}(r,\theta,\gamma) = NY_{l,m}(\theta,\gamma)r^{n-1}e^{-\varsigma r} \tag{2.36}$$

where N is a normalization constant and $Y_{l,m}$ are spherical harmonics, ς is a parameter, and n ,l, m are the principle, the angular momentum, and the magnetic quantum numbers respectively. The exponential dependence on the distance between the nucleus and the electrons in the STOs is also observed in the exact orbitals for the hydrogen atom. As such, the exponential dependence ensures a rapid convergence with increasing functions. Also, STOs exhibit a cusp at the nucleus as in the case of the exact orbitals of the hydrogen atom. In practice, STOs are not commonly used in a basis set due to the fact that there are a large number of integrals that cannot be evaluated analytically.

GTOs lead to integrals that can be evaluated analytically. GTOs can be expressed in polar coordinates as

$$\phi_{\varsigma,n,l,m}(r,\theta,\gamma) = NY_{l,m}(\theta,\gamma)\sum_{l=1}^{M} r^{l}\left(\frac{2\varsigma_{l}}{\pi}\right)^{3/4} e^{-\varsigma r^{2}} \tag{2.37}$$

The squared distance term between the electron and the nucleus in the exponential indicates that GTOs decay too quickly at distances that are far from the nucleus. In contrast to STOs, which exhibit a cusp at the nucleus, GTOs have a zero slope at the nucleus. The basic features of a Gaussian function can be improved by using contracted Gaussian functions that are obtained

from a linear combination of primitive Gaussian functions. This makes the shape of the function closely resemble that of a Slater function.

There are many different contracted basis sets available in the literature or built into electronic structure programs. Pople basis sets[17] are commonly employed in quantum chemical calculations. A Pople basis set takes the form of *X-YG*, where *X* represents the number of functions used to describe core electrons and *Y* represents the number of functions used to describe valence orbitals. Including *G* in this expression indicates that the functions are of Gaussian type. The basis set that is used to perform the calculations in this thesis is 6-31G(d,p). This is a split valence basis set, which means that the core orbitals are represented by a contraction of six primitive GTOs and the valence orbitals are split into two different basis functions. The first basis function describes the inner part of the valence orbitals and is a contraction of three primitive GTOs. The second basis function describes the outer part of the valence orbitals and is represented by one primitive GTO. The (d,p) term indicates that polarization functions are added to all atoms in the basis set. Polarization functions consist of higher angular momentum basis functions that are added to allow atoms in molecules to respond to asymmetry in their local environment. In the 6-31G(d,p) basis set, a single d-type polarization function is added to all heavy atoms whereas a single p-type function is added to each hydrogen atom.

2.9 Hartree-Fock Theory

The starting point for the majority of quantum chemical calculations is the Hartree-Fock method. For multi-electron systems, approximate solutions to the electronic Schrödinger equation can be obtained by using the variational principle. The variational principle states that

an approximate wave function has an energy above or equal to the energy of the exact wave function. The energy of the approximate wave function, also known as the trial wave function, can be calculated using the expression

$$E_{elec} = \frac{\left\langle \Psi^{*}_{elec}(\mathbf{r};\mathbf{R}) \middle| \hat{H}_{elec} \middle| \Psi_{elec}(\mathbf{r};\mathbf{R}) \right\rangle}{\left\langle \Psi^{*}_{elec}(\mathbf{r};\mathbf{R}) \middle| \Psi_{elec}(\mathbf{r};\mathbf{R}) \right\rangle} \tag{2.38}$$

where Ψ_{elec} and Ψ^{*}_{elec} are the trial wave function and its complex conjugate respectively. The numerator is the expectation value of the electronic Hamiltonian operator and the denominator is the norm of the wave function. The trial wave function should satisfy the same properties of the exact wave function. These properties are that the wave function is single-valued, continuous, antisymmetric with respect to the interchange of any two electrons, and does not distinguish between electrons. The antisymmetry and indistinguishability requirements can be met by building it from Slater Determinants, while the continuity requirement is achieved by selecting appropriate basis functions. A Slater determinant is the determinant of an N x N matrix of molecular orbitals χ_N, in which the columns represent the number of molecular orbitals and the rows represent varying the orbitals by the electronic coordinates, **x**(N). For the general case of N electrons and N molecular orbitals, a Slater determinant is given by

$$\Psi_{SD} = \frac{1}{\sqrt{N}} \begin{vmatrix} \chi_1 \mathbf{x}(1) & \chi_2 \mathbf{x}(1) .... \chi_N \mathbf{x}(2) \\ \chi_1 \mathbf{x}(2) & \chi_2 \mathbf{x}(2) ... \chi_N \mathbf{x}(2) \\ .... & .... & .... \\ \chi_1 \mathbf{x}(N) & \chi_2 \mathbf{x}(N) & \chi_N \mathbf{x}(N) \end{vmatrix} \tag{2.39}$$

In the Hartree-Fock model, the trial wave function is constructed from a single Slater determinant. Using the variational principle, the energy of a single Slater determinant wave function can be expressed as

$$E = \sum_{a=1}^{N} h_{aa} + \frac{1}{2}\sum_{a=1}^{N}\sum_{b=1}^{N}\left[J_{ab} - K_{ab}\right] \tag{2.40}$$

where h_{aa} is the one electron energy and is given by

$$h_{aa} = \int d\mathbf{x}_1 \chi_a(\mathbf{x}_1)\left[-\frac{\nabla_1^2}{2} - \sum_{I=1}^{M}\frac{Z_I}{r_{Ii}}\right]\chi_a(\mathbf{x}_1) \tag{2.41}$$

J_{ab} is the Coulomb integral and given by

$$J_{ab} = \int\int d\mathbf{x}_1 d\mathbf{x}_2 \frac{\left|\chi_a(\mathbf{x}_1)\right|^2\left|\chi_b(\mathbf{x}_2)\right|^2}{r_{12}} \tag{2.42}$$

and K_{ab} is the exchange integral and is given by

$$K_{ab} = \int\int d\mathbf{x}_1 d\mathbf{x}_2 \frac{\chi_a^*(\mathbf{x_1})\chi_b(\mathbf{x}_1)\chi_b^*(\mathbf{x}_2)\chi_a(\mathbf{x}_2)}{r_{12}} \tag{2.43}$$

The total Hartree Fock energy can be minimized using the variational principle by altering the coefficients of the molecular orbitals to give the set of molecular orbitals corresponding to the

lowest electronic energy for molecules. The energy of a molecular orbital χ_a can be evaluated using the Fock equation

$$\hat{f}(\mathbf{x}_1)\chi_a(\mathbf{x}_1) = \varepsilon_a \chi_a(\mathbf{x}_1) \tag{2.44}$$

where $\hat{f}$ is the Fock operator and is the sum of the one-electron, Coulomb, and Exchange operators. The one-electron operator is defined as

$$\hat{h}_a = \left(-\frac{\nabla_1^{\,2}}{2} - \sum_{I=1}^{M} \frac{Z_I}{r_{I1}} \right) \tag{2.45}$$

where the first term represents the one-electron kinetic energy and the second term is the Coulomb potential due to *M* nuclei. The Coulomb operator accounts for the average Coulomb repulsion between electrons in molecular orbitals *a* and *b*. The Coulomb operator is expressed as

$$\hat{J}_b(\mathbf{x}_1) = \int \frac{d\mathbf{x}_2 \left|\chi_b(\mathbf{x}_2)\right|^2}{r_{12}} \tag{2.46}$$

where the $\left|\chi_b(\mathbf{x}_2)\right|^2$ term is the charge cloud that results from an electron occupying χ_b. The exchange operator when applied to orbital *a* exchanges the coordinates of the electrons in orbitals *a* and *b.*

$$\hat{K}_b(\mathbf{x}_1)\chi_a(\mathbf{x}_1) = \left(\int \frac{d\mathbf{x}_2 \chi_b^*(\mathbf{x}_2)\chi_a(\mathbf{x}_2)}{r_{12}} \right) \chi_b(\mathbf{x}_1) \tag{2.47}$$

The exchange operator accounts for the Pauli repulsion between electrons in molecular orbitals *a* and *b*.

The ε_a eigenvalue in the Fock equation is the energy of the molecular orbital. The molecular orbitals that are optimized using the Fock equations are used to construct the Slater determinant. The Fock equation can be expressed in terms of a linear combination of *K* basis functions:

$$\hat{f}(\mathbf{x}_1)\sum_{v=1}^{K} c_{vi}\phi_v(\mathbf{r}) = \varepsilon_a \sum_{v=1}^{K} c_{vi}\phi_v(\mathbf{r}) \tag{2.48}$$

The above eigenvalue equation can be solved more easily by conversion into a matrix problem. Multiplying from the left by a basis function and integrating yields

$$\mathbf{FC} = \mathbf{SC}\boldsymbol{\varepsilon} \tag{2.49}$$

where **F** is the Fock matrix that contains Fock matrix elements, $F_{\alpha\beta}$. Each matrix element contains two parts from the Fock operator; integrals that involve one-electron operators and a sum over occupied molecular orbitals of coefficients that are multiplied with two-electron integrals. The **S** matrix is the overlap matrix and contains matrix elements, $S_{\alpha\beta}$, that have the form of

$$S_{\alpha\beta} = \int dr_1 \phi_\alpha^*(\mathbf{r}_1)\phi_\beta(\mathbf{r}_1) \tag{2.50}$$

with each matrix element representing the spatial overlap between basis functions α and β. The **C** matrix is a K x K matrix with columns defining the coefficients, c_{iv}. The **ε** matrix is a diagonal matrix with molecular orbital energies as the diagonal elements. The method for determining the set of coefficients **C** that define the lowest energy single Slater determinant trial wave function is known as the self-consistent field (SCF) procedure. The SCF procedure involves starting with an initial guess of coefficients that form the Fock matrix. The Fock matrix is diagonalized to form a new set of coefficients. The new set of coefficients is then used to construct a new Fock matrix. This procedure is repeated until the set of coefficients used for constructing the Fock matrix is equal to the coefficients that result from diagonalization.

2.10 Complete Active Space Self-Consistent Field Theory

The Hartree Fock method captures the kinetic energy of electrons, the nuclear-electron attraction, the exchange interactions, and electron-electron Coulombic repulsion. The exchange interactions account for the Pauli repulsion between electrons. The electron-electron Coulomb repulsion is treated in an average sense; instantaneous electron-electron interactions are not considered. As a result, the Hartree-Fock method overestimates the electon-electron Coulomb repulsion energy. The energy that is not captured in a Hartree-Fock calculation is known as the correlation energy. There are two types of correlation; dynamic correlation and static correlation. Dynamic correlation arises from electrons actively moving to avoid other electrons. Static correlation, also known as non-dynamical correlation, occurs in system with multiple resonance states of similar energies. This type of correlation accounts for the fact that electrons can avoid each other by occupying different resonance states. Both types of correlation are not captured in

the Hartree-Fock method since the trial wave function is constructed from a single Slater determinant.

A single Slater determinant wave function represents a single resonance state. The Coulomb electron-electron repulsion energy can be decreased by allowing electrons to spread out over several resonance states. Multi-reference methods such as Complete Active Space Self-Consistent Field (CASSCF) are used for chemical problems where static correlation is significant such as describing bond dissociation leading to open-shell products and formation of singlet diradicals. CASSCF, however, does not capture dynamical correlation. Multi-determinant methods such as full configuration interaction, couple-cluster, and perturbation theory calculations are generally used to capture dynamical correlation.

In the CASSCF approach, the trial wave function is constructed by including all Slater determinants that correspond to relevant resonance states. These Slater determinants are called configuration state functions (CSFs). The CSFs are generated by starting with a single Slater determinant corresponding to the HF wave function, and identifying occupied and unoccupied orbitals associated with the changes in electronic structure that occur during the reaction. There will be *m* relevant electrons, which are termed active electrons. Likewise, there will be *n* relevant orbitals, which are termed active orbitals. Collectively, the active electrons and orbitals are termed the active space. The set of CSFs are then obtained by generating Slater determinants corresponding to all possible combinations of *m* active electrons in the *n* active orbitals that are consistent with the multiplicity of the system. The resulting number of CSFs is:

$$N_{\text{determinants}} = \frac{n!(n+1)!}{\left(\frac{m}{2}\right)!\left(\frac{m}{2}+1\right)!\left(n-\frac{m}{2}\right)!\left(n-\frac{m}{2}+1\right)} \qquad (2.51)$$

which can become very large for large active spaces. The selection of which orbitals and electrons to include in the active space is crucial to the success of a CASSCF calculation. Selecting these orbitals is a labourious procedure, involving an examination of orbitals from the preliminary Hartree-Fock calculation to identify those which should be included in the active space. As such, CASSCF calculations are certainly not 'black box' in nature and require a great deal of care more than other methods such as Hartree-Fock and density functional theory.

Once the active space is identified, the CASSCF wave function is represented as a linear combination of CSFs [19]

$$\Psi_{CASSCF} = \sum_{K} A_K \Phi_K \qquad (2.52)$$

where A_K is a configuration mixing coefficient, Φ_K is the CSF, and K is the number of CSFs in the linear combination. The mixing coefficients and molecular orbital coefficients within the CSFs themselves are optimized variationally to minimize the energy of the wave function. The use of Hartree-Fock molecular orbitals in the optimization may be problematic in two scenarios. The first is when extended basis sets are employed that result in many virtual orbitals with low energies and are not well suited to describe electron correlation. The second problem arises if the real wave function has significant multi-configurational character. As such, Hartree-Fock theory would be qualitatively incorrect in describing the nature of the orbitals of the active space. A way of overcoming this problem is to use natural orbitals in the CASSCF optimization. Natural orbitals are the eigenvectors of the reduced one-particle electron density matrix.[20] The density matrix, ρ, for a wave function constructed from CSFs can be expressed as

$$\rho = \sum_J \sum_K a_{JK} \Phi_J^* \Phi_K \tag{2.53}$$

where the coefficients a_{JK} represent a set of numbers that form the density matrix. The natural orbitals reduce the density matrix to diagonal form:

$$\rho' = \sum_K b_K \Phi_K^* \Phi_K \tag{2.54}$$

where the coefficients b_K are the eigenvalues of the reduced density matrix, ρ', and represent the occupation numbers of each natural orbital. For a single Slater determinant wave function, the reduced density matrix is identical to the density matrix used in the formation of the Fock matrix. As such, the molecular orbitals have occupation numbers of exactly 0, 1 or 2. For a multi-determinant wave function constructed from natural orbitals, the occupation numbers may have fractional values between 0 and 2.

Natural orbitals are used in the calculations of the ring opening of cyclobutene and cyclohexadiene along conrotatory and disrotatory pathways in Chapter 4. The set of natural orbitals that define the active space for cyclobutene are shown in Figure 2-3. In the ring opening of cyclobutene, there are four active electrons (two forming the π bond and two forming the carbon-carbon scissile σ bond).

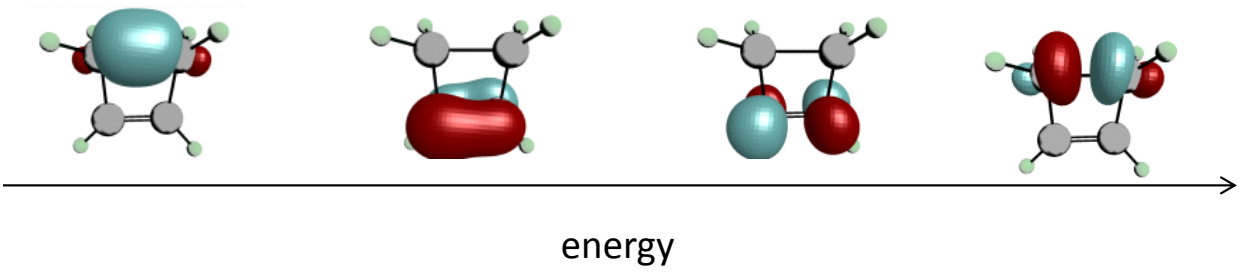

Figure 2-3: Natural orbitals that define the active space for cyclobutene. The different colours on the orbitals indicate different phases of the wave function. The orbitals are arranged from left to right in order of increasing energy.

For the forbidden disrotatory pathway of cyclobutene, the system progresses through a singlet diradical structure, in which two orbitals in the active space each have an occupation number of 1. The singlet diradical has multiple resonance states that can be accurately described with using a multi-reference wave function constructed from natural orbitals.

The CASSCF method is used to investigate the mechanochemical response of cyclobutene along conrotatory and disrotatory pathways using COGEF and EFEI conditions. The results of this study are presented in Chapter 3.

---

[1] Roos, B.O. *Adv. Chem. Phys*. **1987**, *69*, 399.

[2] Jensen, F. *Introduction to Computational Chemistry*, 1999, Wiley, Chichester, England.

[3] Bustamante, C.; Chemla, Y.R.; Forde, N.R.; Izhaky, D. *Annu. Rev, Biochem*. **2004**, *73*, 705-748.

[4] Bell, G.I. *Science*, **1978**, *200*, 618-627.

[5] Zhurkov, S.N. *Intern. J. Fracture Mech*. **1965**, *1*, 311

[6] Erying, H. *J. Chem. Phys.* **1935**, *3*, 107.

[7] Laidler, K.; King, C. *J. Phys. Chem*. **1983**, *87*, 2657.

[8] Ypma, J. T. *SIAM Review*, **1995**, *37*, 531-551.

[9] Ramachandran, K.I.; Deepa, G.; Namboori, K. *Computational Chemistry and Molecular*

Modeling: Principles and Applications, 2008, Springer, Berlin, Germany

[10] Berendsen, H.J.C., *J. Chem. Phys*., **1984**, 3684-3690

[11] Anderson, H.C. *J. Chem. Phys.* **1980**, *72*, 2384-2393

[12] Hoover, W.G. *Physical Review A*, **1985**, *31*, 1695-1697.

[13] Nosé, S. *J. Chem. Phys*. **1984**, *8*[1, 511].

[14] Anderson, H.C. *J. Comput. Phys*. **1983**, *52*, 24.

[15]Slater, J.C. *Phys. Rev.***1930**, *36*, 57.

[16] Boys, S.F.; *Proc. R. Soc. A.* **1950**, *200*, 542.

[17] Ditchfield, R.; Hehre, W.J.; Pople, J.A. *J. Chem. Phys.* **1974**, *54*, 724.

[19] Schmidt, M.W.; Gordon, M.S. *Annu. Rev. Phys. Chem*. **1998**, *49*, 233-236.

[20] Minkin, V.I. *Pure Appl. Chem.***1999**, *71*, 1919-1981.

Chapter 3: COGEF and EFEI-based MD Simulations of Cyclobutene

3.1 Introduction

Molecular dynamics (MD) simulations allow one to explore the potential energy surface (PES) in a physically meaning manner by studying how systems evolve over time. Incorporating mechanical stress into MD simulations can be achieved using two different approaches: External Force is Explicitly Included (EFEI)[1] and COnstrained Geometries simulate External Force (COGEF)[2]. These two approaches differ in the application of the external force, F_{ext}. In the EFEI method, a constant value of F_{ext} is applied between two atoms in a molecule that serve as pulling points (PPs) and the distance changes to maintain this force. In the COGEF method, the distance between PPs is fixed at a target value by stretching the PPs at a constant rate. The force that corresponds to keeping the distance between PPs at the target can then be calculated. Previous theoretical studies have used both EFEI and COGEF methods in MD simulations to investigate the mechanochemical response of cyclobutene.

A recent study based on the COGEF model has used Car-Parrinello molecular dynamics (CPMD) simulations to investigate the ring opening of cyclobutene along conrotatory and disrotatory pathways. [3] The CPMD simulations were performed using density functional theory (DFT) with the local density approximation[4] and the BLYP exchange-correlation functional. A total of 10 BLYP and 10 LDA independent CPMD simulations were performed for unsubstituted cyclobutene with *cis*-PPs (Fig. 3-1) and a pulling rate of 2.0 Å /ps. The authors used *cis*-PPs in the simulation because a sonication study reported by Hickenboth and coworkers[5] has shown that the applying stress between *cis*-PPs activates the ring opening of benzocyclobutene along the formally forbidden disrotatory pathway.

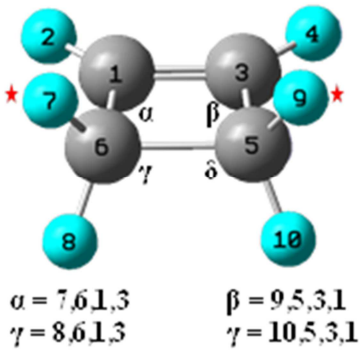

Figure 3-1: Chemical structure of cyclobutene with *cis*-PPs shown in red stars. The grey spheres represent the carbon atoms whereas the blue spheres represent hydrogen atoms. In the MD simulations, stress is applied between the *cis*-PPs using both EFEI and COGEF methods. The terms α, β, γ, and δ represent torsions that define the rotation of the methylene groups. These torsions are used to calculate conrotatory and disrotatory angles that are reported later in this section.

All simulations showed the formation of the conrotatory product. Snapshots taken throughout the simulation are shown in Figure 3-2. These structures show that the system initially moves in a manner consistent with the disrotatory pathway when the scissile bond dissociates at ~0.75 ps. Shortly after (t = 0.82 ps), one of the methylene groups moves in a manner that leads to the product of the conrotatory pathway, which is formed by t = 0.85 ps. Rotation about the central carbon-carbon bond follows, leading to *trans*-1,3-butadiene. The formation of the conrotatory product is inconsistent with the results of sonochemical experiments.

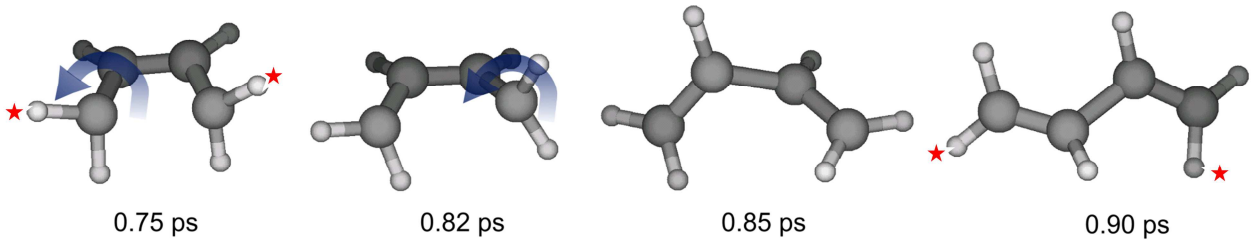

Figure 3-2: Snapshots taken throughout a CPMD simulation of the ring opening of cyclobutene. The PPs are shown with red stars. During the course of the simulation, both methylene groups rotate in the same direction yielding the conrotatory product.[3]

To demonstrate that *cis*-pulling led to the conrotatory product, the authors considered the changes in the conrotatory and disrotatory angles throughout the simulation. Both angles are defined in terms of the rotation of the methylene groups using the torsions illustrated in Figure 3-1. The conrotatory angle is defined in terms of both methylene groups rotating in the same direction and equals (α+δ)–(β+γ). The disrotatory angle is defined in terms of both methylene groups rotating in opposite directions and equals (α+ β) – (γ+ δ). These angles are defined in such a way that the disrotatory (conrotatory) angle tends to ±360° as the system moves along the disrotatory (conrotatory) pathway. The results are presented in Figure 3-3a.

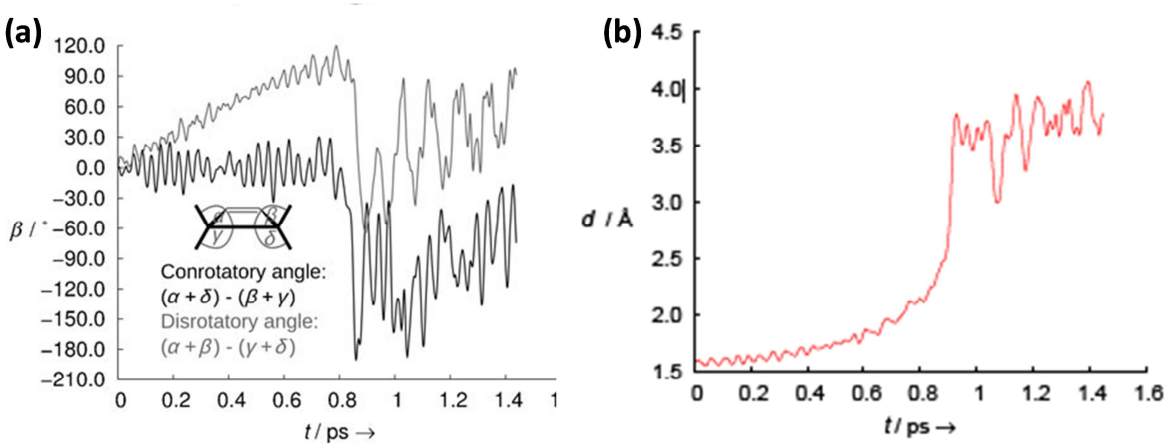

Figure 3-3: Changes in **(a)** conrotatory and disrotatory angles and **(b)** carbon-carbon scissile bond distance throughout a CPMD simulation of the ring opening of cyclobutene. Both angles are defined in terms of the rotation of the methylene groups. The disrotatory angle (gray curve) increases at the beginning of the simulation until approximately 0.75 ps, where the carbon-carbon scissile bond breaks. After this point, the disrotatory angle fluctuates around zero and the conrotatory angle (black curve) dominates the behaviour of the system. The carbon-carbon scissile bond distance steadily increases until the bond dissociation. After this point, the distance fluctuates around a constant value.[3]

Initially, the system follows the disrotatory pathway, with the disrotatory angle increasing and the conrotatory angle fluctuating around zero. The dissociation of the scissile bond at $t \approx$ 0.75 ps is accompanied by a sharp drop in the disrotatory angle to zero. At this point, the

conrotatory angle drops to -180° indicating progression along the conrotatory pathway. This is followed by a steady increase in both the disrotatory and conrotatory angles, which does not seem to be consistent with opening along either pathway. The change in carbon-carbon scissile bond distance was also monitored throughout the simulation (Fig. 3-3b). At the onset of the simulation, the carbon-carbon scissile bond distance steadily increases at a relatively constant rate. The carbon-carbon distances of the scissile bond increases rapidly between 0.75 and 0.9 ps, which can be attributed to its dissociation. After the bond breaks, the distance increases slowly from a value consistent with the PPs separation in the product.

The results of the CPMD simulations on ester substituted benzocyclobutene showed that the ring opening under mechanochemical conditions proceeds predominately through a disrotatory manner. A total of 15 LDA and 20 BLYP CPMD simulations were performed with 6 of the 15 LDA simulations and 17 of the 20 BLYP simulations showing disrotatory opening. The authors rationalized the system following a formally forbidden disrotatory pathway through intermediate orbital localization. Specifically, the ester functional groups and the benzene ring provide the orbitals with enough flexibility to change symmetry throughout the course of the reaction. The symmetry of the highest occupied molecular orbital (HOMO) was monitored throughout the simulation. The HOMO, which was mirror-symmetrical in the reactant becomes anti-symmetrical in the product (Fig. 3-4). Such intermediate orbital localization effects, in which the orbitals are localized on the atom, connect orbitals of different symmetry in violation of the WH rules.

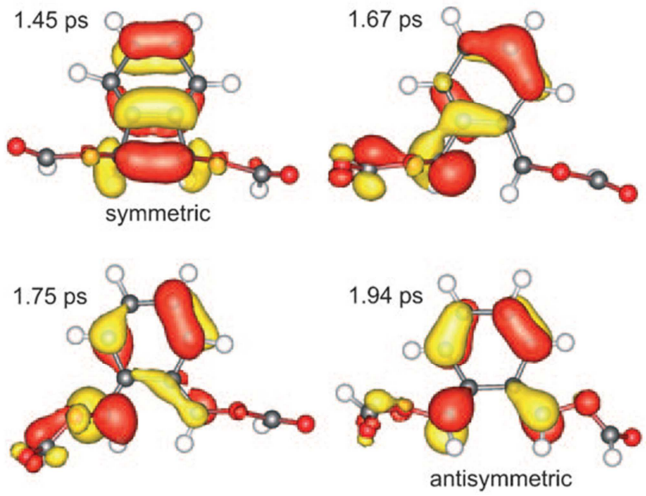

Figure 3-4: Change in the symmetry of the HOMO throughout a CPMD simulation. The HOMO is mirror-symmetrical in the reactant and becomes anti-symmetrical in the product. The connection of orbitals with different symmetry leads to the mechanically induce anti-WH product.[3]

Another recent study has examined the ring opening of cyclobutene under mechanochemical conditions.[6] The study was carried out by performing *ab initio* MD simulations that were based on the EFEI method. The MD simulations were performed at the CASPT2(4,4) /6-31G(d,p) level of theory.[7,8] A constant applied external force, F_{ext}, was applied between *cis* and *trans* substitutents, with 20 independent trajectories reported for each case. Snapshots taken from the MD simulations are shown for both *cis* and *trans*-pulling at a F_{ext} value of 2.5 nN in Figure 3-5.

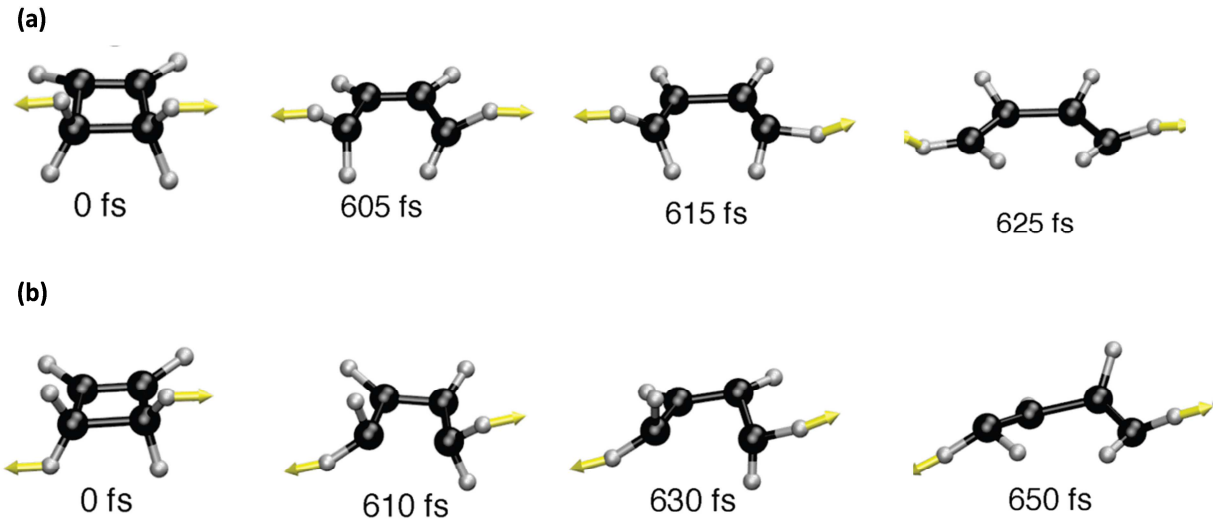

Figure 3-5: Snapshots taken during an MD simulation for the ring opening of cyclobutene using **(a)** *cis*-PPs and **(b)** *trans*-PPs at F_{ext} of 2.5 nN. The black spheres denote the carbon atoms and the white spheres denote the hydrogen atoms. The PPs are represented using yellow arrows. The application of F_{ext} between *cis*-PPs results in the system proceeding through a disrotatory pathway whereas the application of F_{ext} between *trans*-PPs yields the conrotatory product. The rupture of the carbon-carbon scissile bond was reported at a minimum F_{ext} of 1.5 nN. Applied forces that were greater than this value resulted in the system following the same pathways as observed for 2.5 nN. [6]

The series of structures shown in Figure 3.5a with PPs in a *cis* configuration with respect to the ring show that the system moves along the disrotatory pathway before and after the dissociation of the scissile bond. Likewise, the structures in Figure 3.5b, which were obtained with the PPs in a *trans* configuration, show that the ring follows a conrotatory pathway. The results of the MD simulations indicate that the selection of PPs influences the reaction pathway that the system follows. These results are consistent with those of sonication experiments, which demonstrated that cyclobutene moieties embedded in macromolecules can be selectively opened along conrotatory or disrotatory pathways based on the positions of the groups used to apply the external force.

Collectively, the previous theoretical studies indicate that EFEI-based and COGEF-based MD simulations lead to different results for the ring opening of cyclobutene. Specifically, the

studies using the COGEF method have shown the system proceeds exclusively through a conrotatory pathway when stress is applied between *cis*-PPs and differs from previous sonication experiments. The studies using the EFEI method showed that the system proceeds exclusively through a disrotatory pathway when stress is applied between *cis*-PPs in agreement with the sonication experiments, assuming that cyclobutene is a suitable approximation to the substituted cyclobutene molecules used in those experiments. The objective of this Chapter is to identify the origin of the differences between the outcomes of simulations performed using these methods. To accomplish this, first-principles molecular dynamics (FPMD) simulations were performed to study the ring opening of cyclobutene under COGEF and EFEI conditions. The results of the COGEF and EFEI-based MD simulations are presented in Sections 3.3 and 3.5 respectively. The analysis of the MD simulations will be carried out by performing relaxed potential energy surface (PES) scans for the disrotatory and conrotatory pathways. The results are presented in Sections 3.4 and 3.6 respectively. Determining the underlying difference between the COGEF and EFEI methods would clarify the correct manner to simulate MD simulations that incorporate mechanical stress.

3.2 Computational details

All calculations were performed at the CASSCF(4,4)/6-31G(d,p) level of theory. [9] FPMD simulations based on EFEI and COGEF methods were performed using a version of the GAMESS-US software package[10,11] that we modified to enable calculations on the force-modified potential energy surface (FMPES). The FPMD simulations were performed under canonical (NVT) conditions using a Nosé-Hoover thermostat[12,13] to maintain a temperature of 300K and a time step of 1.0 fs. A 5 ps timescale was used for the EFEI-based simulations. The

timescales for the COGEF-based simulations were chosen such that they were long enough to permit the reaction to occur. To understand how the presence of an applied force affects the outcome of the FPMD simulations, force-modified potential energy surfaces (FMPESs) were generated for both COGEF and EFEI methods using relaxed PES scans with the Gaussian 09 software package[14]. In general, PES scans involve calculating the energy for a series of molecular structures. The structures are obtained by varying a parameter such as a bond length, angle, or torsion. The initial and final values as well as the number of steps in between are specified for the selected parameter. In rigid scans, all of the non-constrained variables are kept fixed from the starting structure. In relaxed scans, however, the non-constrained variables are optimized. This allows a series of optimized structures to be generated on the PES. The parameter that was systematically varied was the distance between PPs in the COGEF-based simulations and the magnitude of F_{ext} in the EFEI-based simulations.

3.3 COGEF-based MD simulations

FPMD simulations were performed for the ring opening of cyclobutene under mechanochemical conditions using the COGEF procedure. Specifically, the application of a mechanical force was modeled by increasing the distance between the PPs at a fixed rate. Five independent trajectories were evaluated at each of four different pulling rates, yielding a total of 20 calculated trajectories. The pulling rates used were 0.5 Å/ps, 1.5 Å/ps, 2.5 Å/ps, and 5.0 Å/ps. The timescales for each pulling rate varied to permit the reaction to occur. All MD simulations showed that opening proceeds exclusively through a conrotatory pathway.

Snapshots that are taken for an MD simulation at a pulling rate of 0.5 Å/ps are shown in Figure 3-6 to illustrate the conrotatory ring opening process that was observed. At t = 0.0 ps, the

system is in the form of cyclobutene. The scissile bond dissociates at t = 2.8 ps, with the orientation of the methylene groups consistent with opening along the disrotatory pathway. However, shortly after (t = 3.0 ps), one of the methylene groups rotates in a manner that leads to the conrotatory product. Rotation about the central carbon-carbon bond follows, with the system ultimately forming *trans*-1,3-butadiene along the conrotatory pathway. This series of processes is analogous to those shown in Figure 3-2, which were also obtained using the COGEF model.

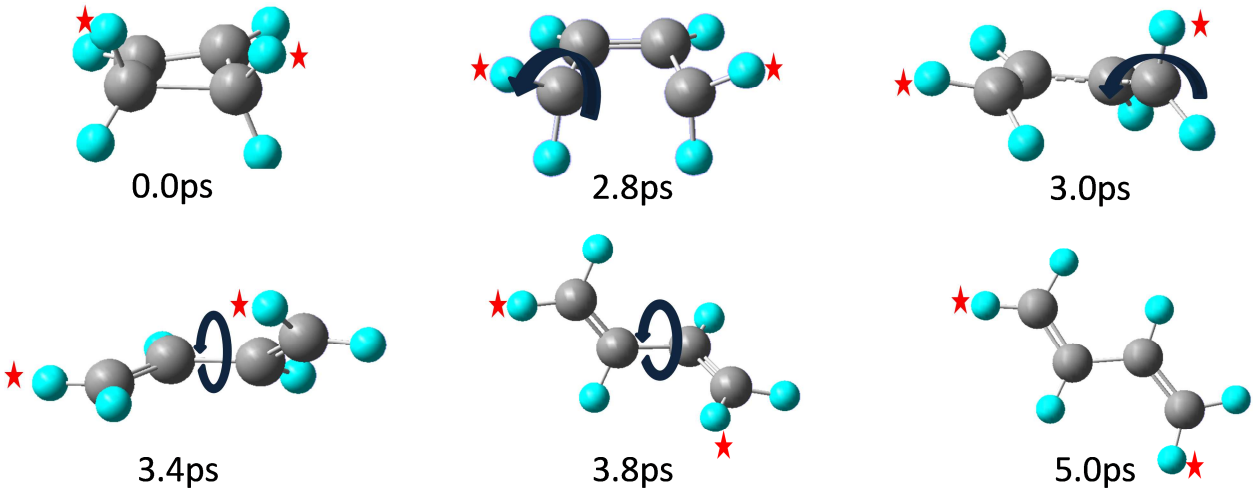

Figure 3-6: Snapshots taken during an FPMD simulation for the ring opening of cyclobutene using a pulling rate of 0.5 Å/ps. *cis*-PPs were used in the simulation and shown with red stars. The motion of the system is indicated using dark blue arrows.

The carbon-carbon scissile bond distances that yielded the structures in Figure 3-6 are shown in Figure 3-7. At the beginning of the simulation, the carbon-carbon scissile bond distance increases at a slow rate. At approximately 3.0 ps, a large increase in the carbon-carbon scissile bond distance is observed, and can be attributed to the cleavage of the carbon-carbon scissile bond. After this point in the simulation, the distance fluctuates around the distance in the *cis*-1,3-butadiene product before steadily increasing to the carbon-carbon distance in *trans*-1,3-butadiene.

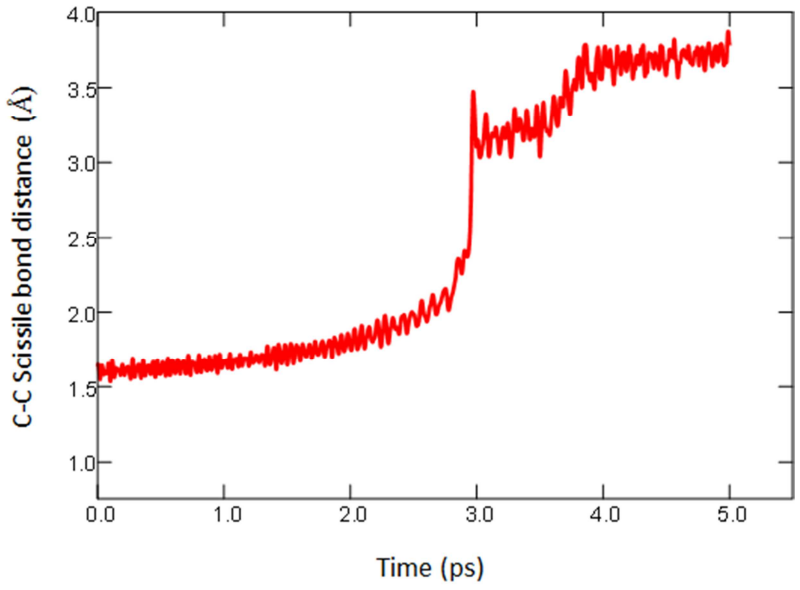

Figure 3-7: Changes in the carbon-carbon scissile bond distance during a FPMD simulation of the ring opening of cyclobutene with *cis*-PPs at a pulling rate of 0.5 Å/ps. Initially, the distance increases at a relatviely slow rate. The dissociation of the carbon-carbon scissile bond occurs at approximately 3.0 ps and is observed by a sudden increase in the carbon-carbon scissile bond distance.

The conrotatory and disrotatory angles for the ring opening of cyclobutene were also monitored throughout the FPMD simulation. These angles were calculated using the definition introduced by the previous COGEF study[3], in which the conrotatory angle equals (α+δ) – (β+γ) and the disrotatory angle equals (α+β) – (γ+δ). The calculated conrotatory and disrotatory angles for the duration of the FPMD simulation are shown in Figure 3-8. At the onset of the simulation, the conrotatory angle fluctuates around zero and the disrotatory angle steadily increases. At approximately 3.0 ps, the conrotatory angle increases sharply and the disrotatory angle drops below zero. The analysis of the angles indicates that the ring opening of cyclobutene proceeds toward a disrotatory pathway at the initial stages of the simulation. However, after the dissociation of the carbon-carbon scissile bond, the conrotatory pathway dominates the behaviour of the system. The conrotatory pathway for the ring opening of cyclobutene was also observed for the other rates of pulling.

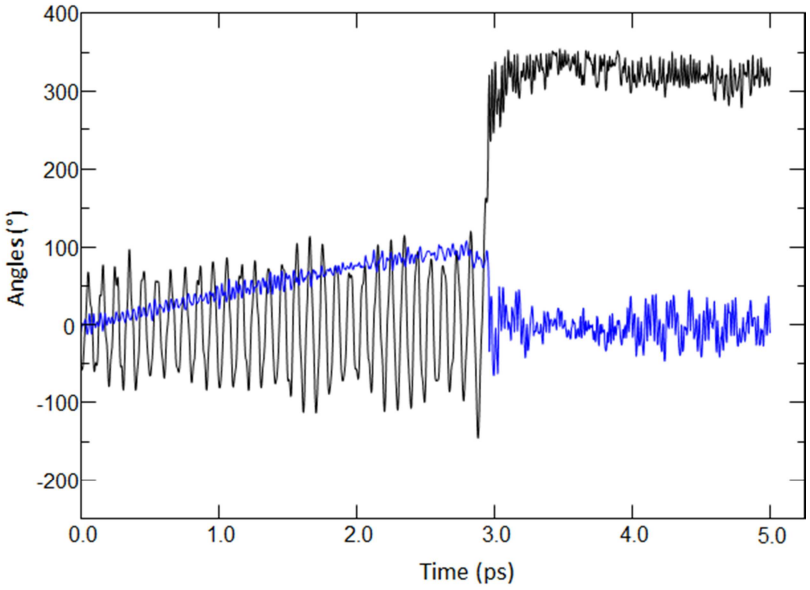

Figure 3-8: Changes in the conrotatory angle (black curve) and the disrotatory angle (blue curve) during an MD simulation at a pulling rate of 0.5 Å/ps. During the initial stages of the simulation, the conrotatory angle fluctuates around zero and the disrotatory angle steadily increases. The carbon-carbon scissile bond is cleaved at approximately 3.0 ps. After this point, the disrotatory angle drops below zero and the conrotatory angle significantly increases.

The results obtained from the COGEF-based FPMD simulations are consistent with the previous COGEF simulations[3], in which the ring opening proceeded exclusively through a conrotatory pathway. These results, however, are inconsistent with sonication experiments[4], which demonstrated that the ring opening proceeds through a disrotatory pathway when stress is applied between polymeric substituents in a *cis*-configuration.

3.4 Analysis of COGEF-based MD simulations using PES scans

The results from the COGEF-based MD simulations show that the ring opening of cyclobutene proceeds exclusively through a conrotatory pathway regardless of the rate of pulling. To understand why this is the case, the FMPES was constructed for both the conrotatory and disrotatory pathways. The FMPES was obtained by incorporating the mechanical work that

results from pulling at a constant rate into the Born-Oppenheimer PES according to the expression

$$V_{COGEF}(\mathbf{x}, q) = V_{BO}(\mathbf{x}) - F_{int}q(\mathbf{x}) \tag{3.1}$$

where $V_{COGEF}(\mathbf{x}, q)$ is the force-modified potential energy function that arises from imposing a distance constraint on the system, V_{BO} is the Born-Oppenheimer potential energy as a function of all nuclear coordinates **x** without any constraints, $q(\mathbf{x})$ is the calculated distance, and F_{int} is the magnitude of the restoring force required to keep the PP separation at the target distance q_0.

The Born-Oppenheimer and COGEF FMPESs were generated for both conrotatory and disrotatory pathways. In the conrotatory PES, the torsions α and δ were set equal to each other and fixed throughout the distance scan. This constraint is consistent with the rigorous definition of the conrotatory pathway in which the two methylene units move in the same direction at the same rate. In the disrotatory PES, the torsions α and β were set equal to each other and fixed throughout the distance scan. This constraint is consistent with the rigorous definition of the disrotatory pathway in which the two methylene units move in opposite directions at the same rate. The constraints in the PES scans are further illustrated in the Figure 3-9. The Born-Oppenheimer PESs for the conrotatory and disrotatory pathways are shown in Figure 3-10. In these plots, the energy was calculated by scanning the distance between PPs at the fixed torsions. Yellow lines one these plots illustrate the minimum energy pathways (MEPs) on each surface.

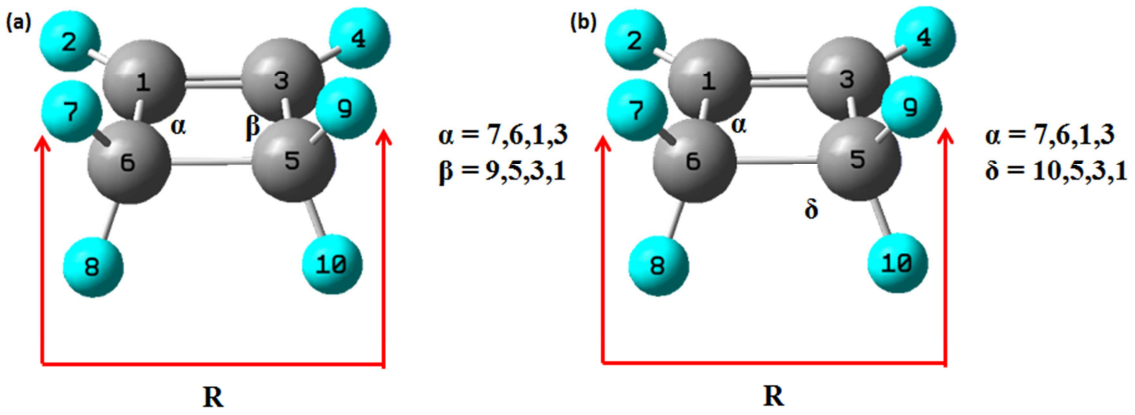

Figure 3-9: Schematic representations of cyclobutene showing the constraints in the PES scans for the **(a)** disrotatory pathway and **(b)** the conrotatory pathway. In the disrotatory PES scan, the torsions α and β are fixed and set equal to each other. In the conrotatory PES, the torsions α and δ are fixed and set equal to each other. The distance between the PPs (R) was also kept fixed during the scan for both pathways.

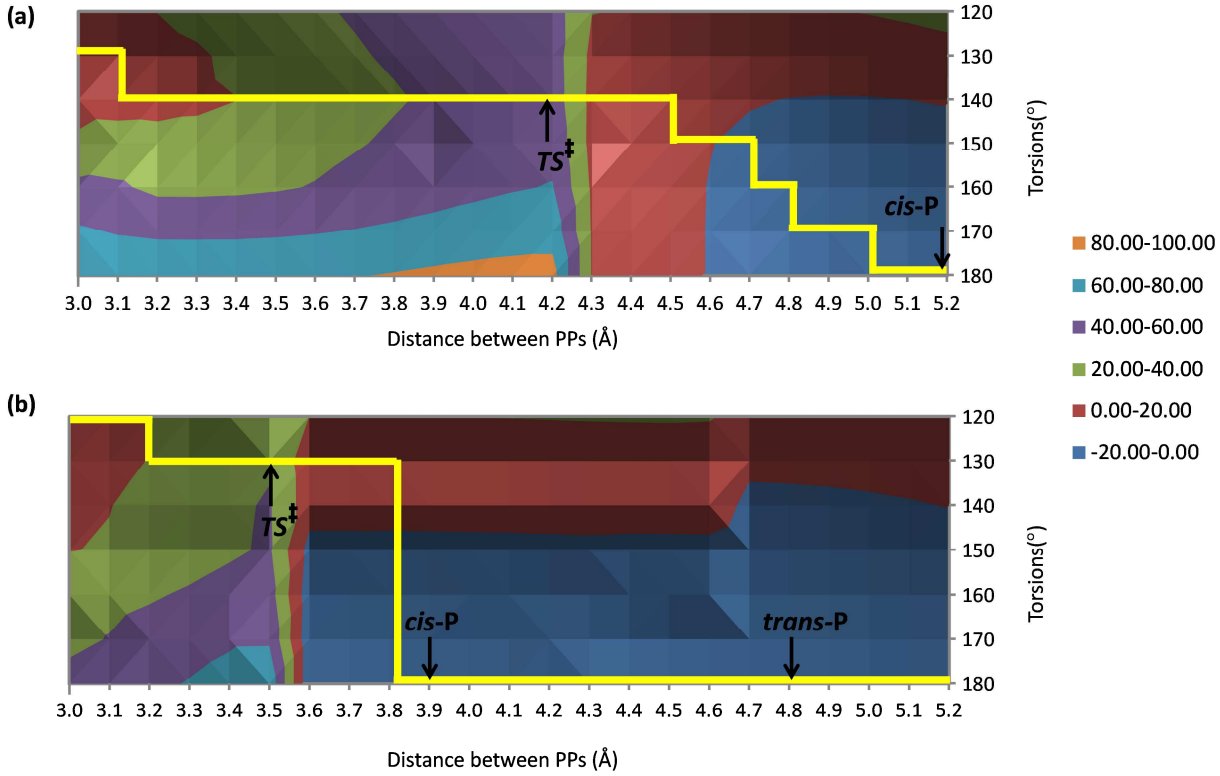

Figure 3-10: Born-Oppenheimer potential energy surfaces of the ring opening of cyclobutene for the **(a)** disrotatory pathway and **(b)** conrotatory pathway. The different colors on the contour plots represent the Born-Oppenheimer potential energy and are expressed in kcal/mol. The energies are calculated relative to the optimized reactant geometry, which corresponds to a structure at a PP distance of 2.5 Å. The minimum energy pathway (MEP) for both surfaces is outlined in yellow. For both pathways, the system progresses from reactant-like geometries at small PP distances to the respective products. The double daggers indicate estimated transition states for both pathways.

For the disrotatory Born-Oppenheimer PES, the energy increases steadily as the system progresses from reactant-like geometries at small PP separations to structures with larger PP separations resembling the disrotatory transition state (Fig 3-10a). The estimated transition state on the disrotatory PES is observed at a PP distance of 4.2 Å and is indicated by a double dagger symbol. As the system progresses from this point on the surface to a structure with a PP distance of 4.3 Å, the energy of the system sharply decreases. The sharp decrease in energy can be attributed to the dissociation of the carbon-carbon scissile bond. Once the carbon-carbon bond is cleaved, the methylene groups are free to rotate to form the disrotatory *cis*-1,3-butadiene, which was observed at a PP distance of 5.2 Å. The *trans*-1.3-butadiene product is not observed on the disrotatory Born-Oppenheimer PES because its carbon-carbon distance of 5.5 Å is not on the scanned surface. At longer PP distances, it is expected that the *cis*-1,3-butadiene product would rotate around the carbon-carbon single bond to form *trans*-1,3-butadiene.

For the conrotatory Born-Oppenheimer PES, the energy steadily increases as the system progresses from reactant-like geometries at small PP distances to structures with larger PP distances resembling the conrotatory transition state (Fig 3-10b). The estimated transition state on the conrotatory PES is observed at a PP distance of 3.5 Å and is indicated by a double dagger symbol. As observed on the disrotatory Born-Oppenheimer PES, the energy on the conrotatory Born-Oppenheimer PES decreases sharply as the system progresses from the estimated transition

state to a structure with a PP distance of 3.6 Å. Once the carbon-carbon bond is cleaved, the methylene groups are free to rotate to form the conrotatory *cis*-1,3-butadiene product, which corresponds to a PP distance of 3.9 Å and labeled *cis*-P on the surface. The *cis*-1,3-butadiene conrotatory product rotates around the carbon-carbon single bond to form the *trans*-1,3-butadiene conrotatory product, which corresponds to a PP distance of 4.8 Å and labeled trans-*P* on the surface.

The reaction barriers for both pathways can be estimated from the MEP connecting the reactant and product. The barrier for the conrotatory pathway is approximately 38 kcal /mol whereas the barrier for the disrotatory pathway is approximately 51 kcal /mol. The barriers were calculated using the optimized reactant and the estimated transition states. These values are in close agreement with the barriers calculated using the optimized transition state structures, which were 37 kcal / mol and 50 kcal / mol for the conrotatory and disrotatory pathways respectively. The relatively large difference in the barriers is expected since the disrotatory ring opening of cyclobutene is a formally forbidden high energy pathway according to the Woodward-Hoffmann rules. [15,16]

The FMPESs for the COGEF-based simulations were generated using equation (3.1). The resulting plots are shown in Figure 3-11. The yellow line on the conrotatory surface indicates the MEP path on that surface. The solid red line appearing on the disrotatory and conrotatory surfaces designates a MEP that starts on the disrotatory surface and then moves to the conrotatory surface after the scissile bond dissociates. The dashed red line indicates a possible route along which the system remains on the disrotatory surface after the scissile bond dissociates.

The MEP on the disrotatory surface shows that the energy increases steadily as the system progresses from reactant-like geometries at small PP distances to structures with larger PP distances resembling the disrotatory transition state (Fig 3-11a). The estimated transition state on the disrotatory PES is observed at a PP distance of 4.2 Å and is indicated by a double dagger symbol. As the system moves from this point to a structure with a PP distance of 4.3, the carbon-carbon scissile bond is cleaved. As the carbon-carbon scissile bond breaks, the methylene groups rotate from a disrotatory torsion of 150° to 120°. This is consistent with the results of the MD simulations. When the torsions reach 120°, the system is in a geometry in which the methylene units could easily rotate to yield either the conrotatory or disrotatory products. The data indicate that movement along the disrotatory direction as the PP separation increases leads to an increase in the energy. In fact, the position corresponding to the disrotatory product is not a local minimum on the FMPES. These results indicate that the transformation of the Born-Oppenheimer PES due to the application of an external force under COGEF conditions prevents the system from following the disrotatory pathway once the scissile bond dissociates. Indeed, the lowest energy pathway the system can follow after the scissile bond dissociates involves the torsion remaining at 120° (red dashed line), which does not lead to a structure consistent with the ring opening of cyclobutene. Instead, once the torsions reach 120°, it is energetically favourable for the system to move to the conrotatory pathway, with the torsions increasing in a manner that involves both methylene units rotating in the same direction. This pathway is designated by the red line on the conrotatory PES, which is a continuation of the red line on the disrotatory PES. In addition to the pathway that connects the initial disrotatory pathway to the conrotatory product, it is possible for the system to follow a pathway (yellow line in Figure 3-11b) that remains entirely on the conrotatory surface. Ultimately, both pathways (solid red and yellow curves) lead to the

formation of the conrotatory *trans*-1.3-butadiene product. This change in the FMPES accounts for the fact that only conrotatory products were observed during the MD simulations.

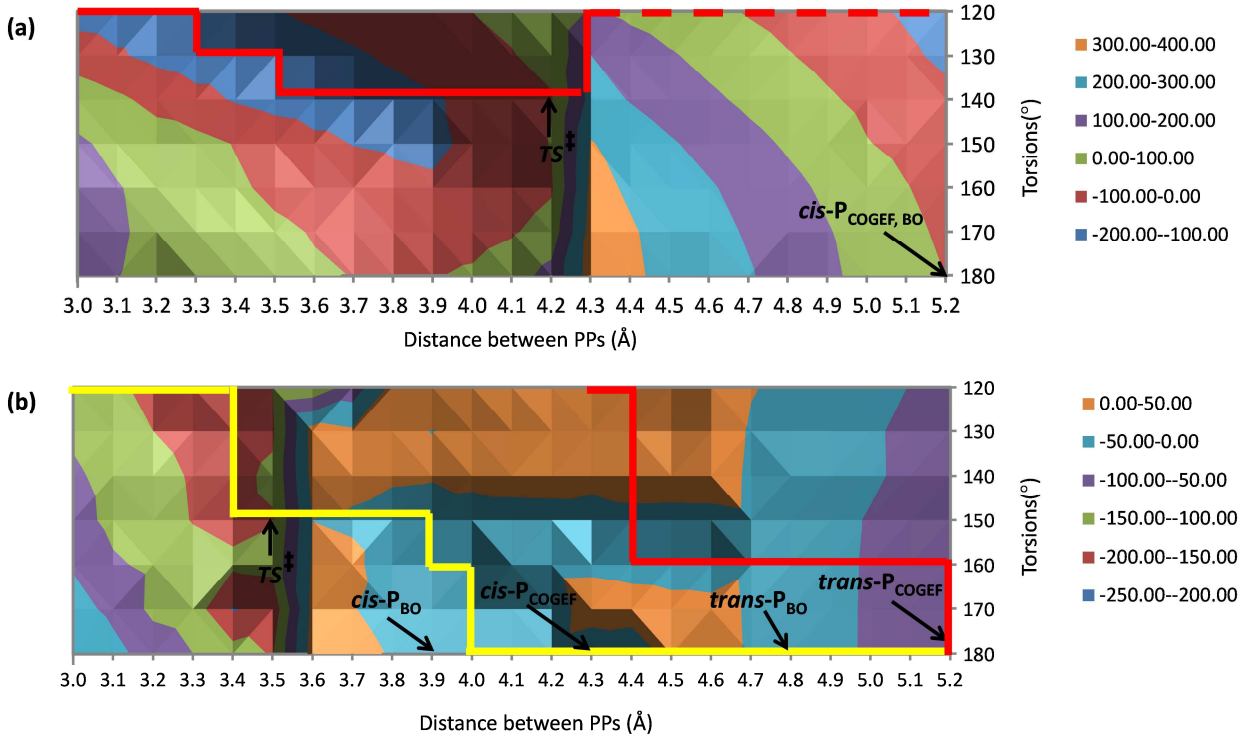

Figure 3-11: FMPESs of the ring opening of cyclobutene under COGEF mechanochemical conditions for (a) the disrotatory pathway and (b) the conrotatory pathway. The different colors on the contour plots represent the COGEF potential energy and are expressed in kcal/mol as shown in the legends. Note that the colors on the disrotatory surface do not correspond to the same energy range on the conrotatory surface. The energies are calculated relative to the optimized reactant geometry, which corresponds to a structure at a PP distance of 2.5 Å. The solid yellow, solid red, and dashed red curves represent the energy pathways starting from the conrotatory structures at small PP distances leading to the conrotatory *trans* product, starting from the disrotatory structures at small PP distances leading to the conrotatory trans product, and an alternative pathway on the force-modified disrotatory PES.

The results obtained from the FMPES scans under COGEF conditions are consistent with the FPMD simulations. The PESs show that the use of the COGEF model results in FMPESs that strongly favor the conrotatory pathway. The MEP for the system to follow is to progress from reactant-like distance on the disrotatory FMPES to form the product on the conrotatory FMPES, as observed in the FPMD simulations. Regardless of the rate of pulling in the MD simulations,

the system proceeds exclusively through the conrotatory pathway because the underlying FMPES does not contain a MEP that leads to the disrotatory product, and moreover, the disrotatory product is not a minimum on that surface.

3.5 EFEI-based MD simulations

FPMD simulations for the ring opening of cyclobutene under EFEI mechanochemical conditions were carried out by applying a constant F_{ext} between *cis*-PPs and allowing the distance to change over time. A total of 30 MD simulations were performed with five independent trajectories calculated at six different values of F_{ext}. The F_{ext} values varied from 2500 pN to 3000 pN in 100 pN intervals. The results of the MD simulations show that the ring opening is observed when $F_{ext} \geq$ 2800 pN. All simulations showed that the opening proceeds exclusively through a disrotatory pathway.

Snapshots that are taken from an MD simulation at F_{ext} = 2900 pN are shown in Figure 3-12. The structure at 0.1 ps shows that the scissile bond is quite extended and the methylene groups are rotated in a manner consistent with motion along the disrotatory pathway. This deformation of the structure is due to the application of F_{ext}. The scissile bond ruptures at ~1.6 ps, with the methylene groups moving in a manner that yields the disrotatory product. Rotation about the central carbon-carbon bond follows. Ultimately, this series of processes yields *trans*-1,3-butadiene along a disrotatory pathway.

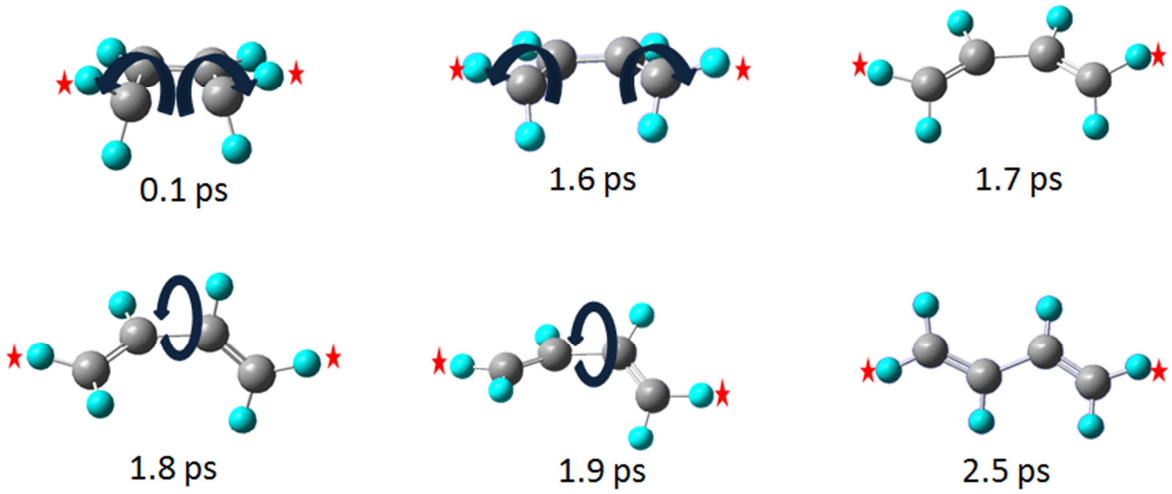

Figure 3-12: Snapshots taken during an MD simulation for the ring opening of cyclobutene at F_{ext} = 2900 pN. *cis*-PPs were used in the simulation and are shown with red stars. As the reaction progresses, both methylene groups rotate in opposite directions to yield the *cis*-conrotatory product observed at around 1.8 ps. Rotation around the carbon-carbon single bond leads to the formation of the *trans*-conrotatory product at 2.5ps. The motion of the system is indicated using dark blue arrows.

To illustrate the formation of the disrotatory product in the constant force MD simulations, the change in the carbon-carbon scissile bond distance was monitored over time. At the beginning of the MD simulation, the carbon-carbon scissile bond distance fluctuates around the equilibrium bond length until breaking rapidly at approximately 1.5 ps (Fig 3-13). The sudden jump in distance can be attributed to the cleavage of the carbon-carbon scissile bond. In the EFEI based simulations, the system is not stretched in a continuous manner as in the case of the COGEF based simulations.

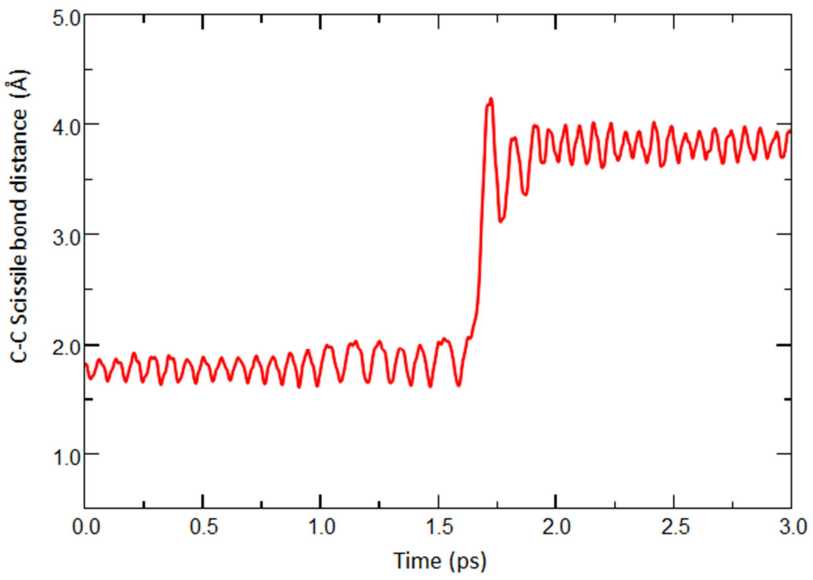

Figure 3-13: Changes in the carbon-carbon scissile bond distance during an MD simulation at a F_{ext} of 2900 pN. Initially, the distance fluctuates around the equilibrium carbon-carbon single bond length. The dissociation of the carbon-carbon scissile bond occurs at approximately 1.6 ps and is observed by a sudden increase in the distance.

The conrotatory and disrotatory angles for the ring opening of cyclobutene were also monitored throughout the MD simulation. The calculated conrotatory and disrotatory angles are shown in Figure 3-14. At the onset of the simulation, the conrotatory and disrotatory angles fluctuate around 0 and 100° respectively. At approximately 1.6 ps, the disrotatory angle sharply increases and the conrotatory angle decreases below 0°. The analysis of the angles indicates that disrotatory angle dominates the behavior of the system throughout the FPMD simulation. The results obtained for the carbon-carbon scissile bond length as well as the conrotatory and disrotatory angles were observed for the MD simulations at the other values of F_{ext}.

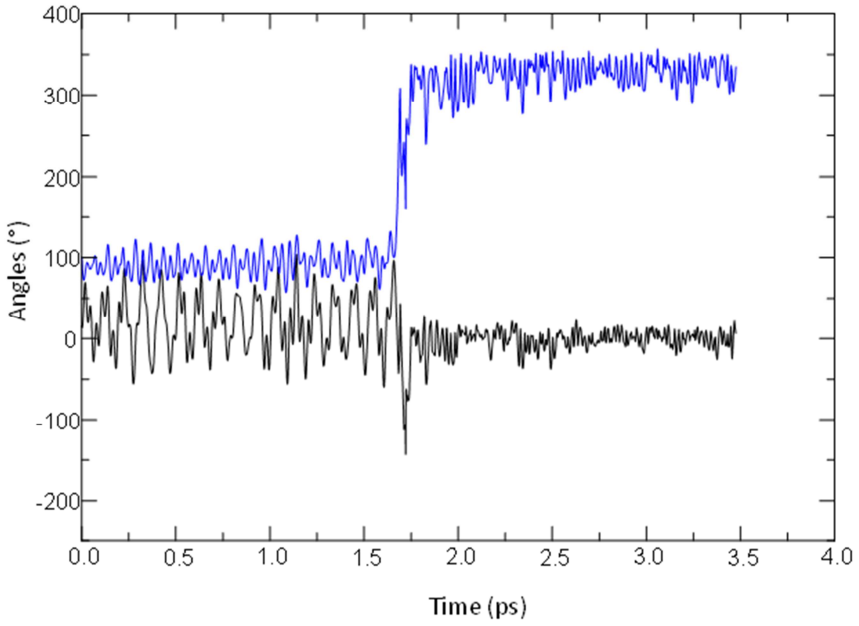

Figure 3-14: Changes in the conrotatory angle (black curve) and the disrotatory angle (blue curve) during an MD simulation at F_{ext} of 2900 pN. During the initial stages of the simulation, the conrotatory and disrotatory angles fluctuate around 0 and 100° respectively. The carbon-carbon scissile bond is cleaved at approximately 1.6ps. After this point, the conrotatory angle drops below 0° and the disrotatory angle significantly increases.

The observed disrotatory opening in the EFEI-based FPMD simulations is inconsistent with the COGEF-based simulations, which showed the ring opening proceeds exclusively through a conrotatory pathway. The results of the EFEI-based simulations, however, are in agreement with previous sonication experiments, assuming that cyclobutene is a suitable approximation to the substituted cyclobutene molecules used in those experiments.

3.6 Analysis of EFEI-based MD simulations using PES scans

To understand the formation of the disrotatory product in the EFEI based FPMD simulations, FMPESs were constructed for both conrotatory and disrotatory pathways. The FMPES was obtained by incorporating the mechanical work term that results from the application of F_{ext} between *cis*-PPs according to Marx's formalism[1]:

$$V_{EFEI}(\mathbf{x}, q) = V_{BO}(\mathbf{x}) - F_{ext} q(\mathbf{x}) \tag{3.2}$$

where $V_{EFEI}(\mathbf{x}, q)$ is the force-modified potential energy function that arises from applying a constant F_{ext} between the PPs, V_{BO} is the Born-Oppenheimer potential energy as a function of all nuclear coordinates $\mathbf{x}$, and $q(\mathbf{x})$ is the calculated distance between PPs. The calculated FMPESs for both pathways are shown in Figures 3-15 to 3-17 at F_{ext} = 500, 1000, and 1500 pN with labels indicating stationary points and yellow lines indicating MEPs.

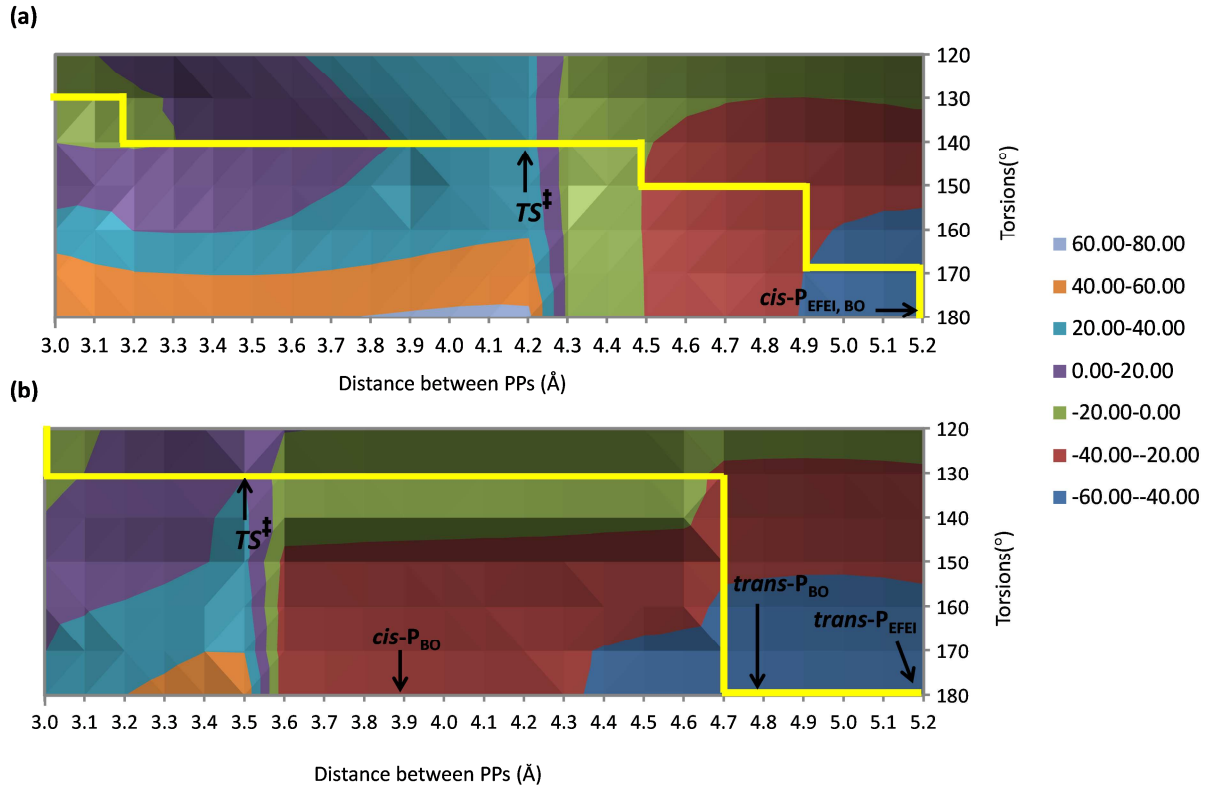

Figure 3-15: FMPES of the ring opening of cyclobutene for the **(a)** disrotatory pathway and **(b)** conrotatory pathway under EFEI mechanochemical conditions at F_{ext} = 500 pN. The different colors on the contour plots represent the EFEI potential energy and are expressed in kcal/mol as shown in the legends. The energies are calculated relative to the optimized reactant structure at F_{ext} = 500 pN. The MEP for both pathways is outlined in yellow and the transition states are indicated with double daggers.

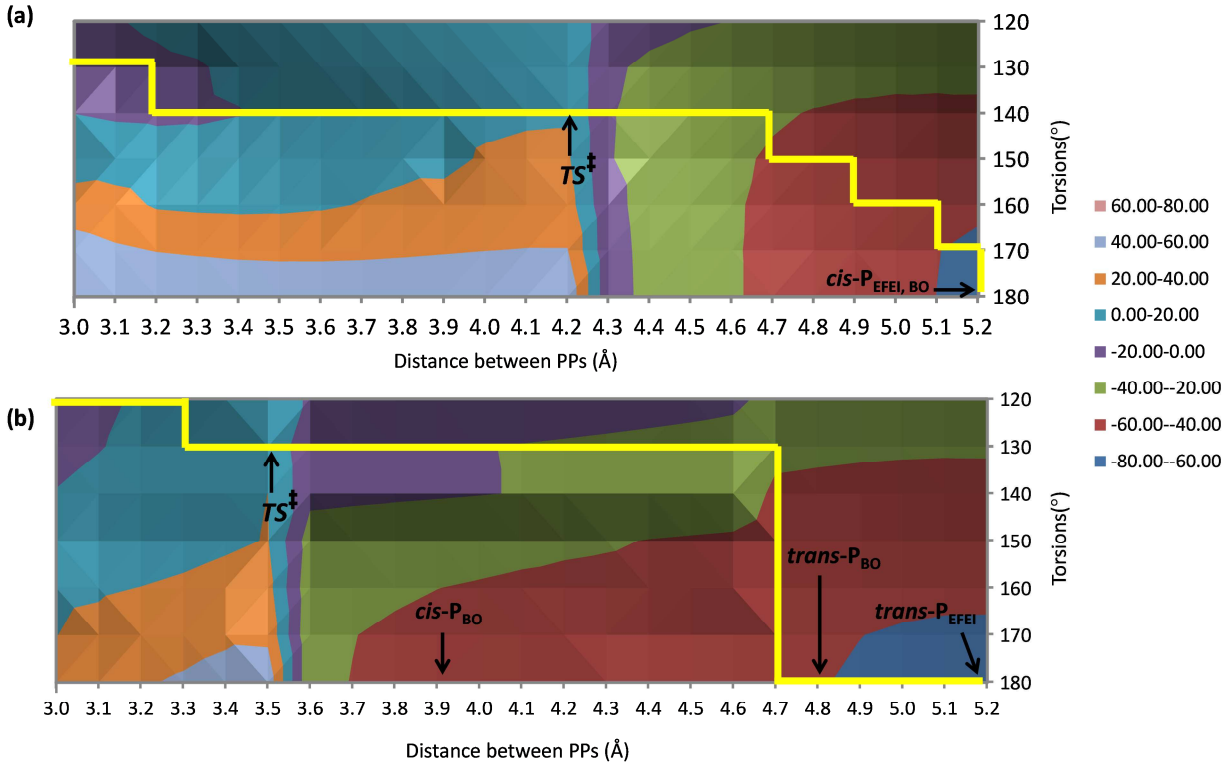

Figure 3-16: FMPES of the ring opening of cyclobutene for the **(a)** disrotatory pathway and **(b)** conrotatory pathway under EFEI mechanochemical conditions at F_{ext} = 1000 pN. The different colors on the contour plots represent the EFEI potential energy and are expressed in kcal/mol as shown in the legends. The energies are calculated relative to the optimized reactant structure at F_{ext} = 1000 pN. The MEP for both pathways is outlined in yellow and the transition states are indicated with double daggers.

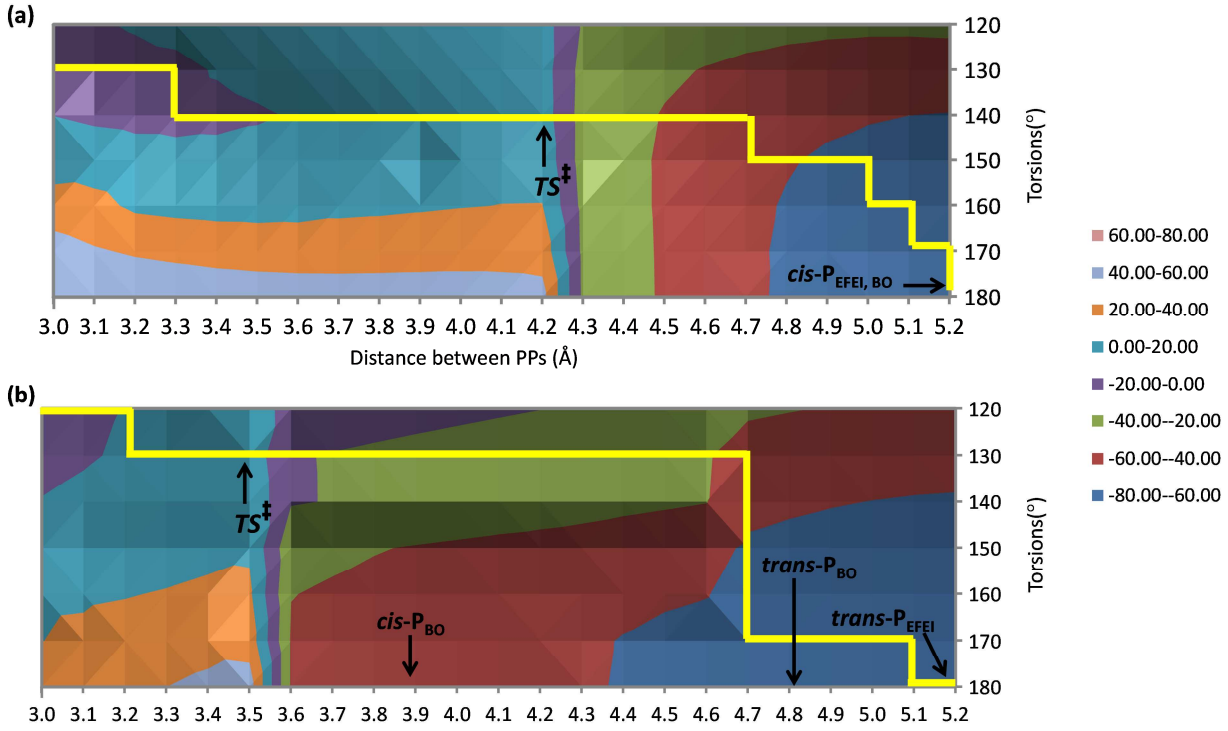

Figure 3-17: FMPES of the ring opening of cyclobutene for the **(a)** disrotatory pathway and **(b)** conrotatory pathway under EFEI mechanochemical conditions at F_{ext} = 1500 pN. The different colors on the contour plots represent the EFEI potential energy and are expressed in kcal/mol as shown in the legends. The energies are calculated relative to the optimized reactant structure at F_{ext} = 1500 pN. The MEP for both pathways is outlined in yellow and the transition states are indicated with double daggers.

To illustrate the greatest effect of applied F_{ext} on the potential energy surface, the results of the FMPES obtained at F_{ext} = 1500 pN will be compared to the Born-Oppenheimer PES. The solid yellow lines on the disrotatory and conrotatory FMPESs indicate the MEP (Fig. 3-17).

In the disrotatory FMPES, the energy increased steadily as the system progressed from reactant-like geometries at small PP separations to structures with larger PP separations resembling the disrotatory transition state (Fig. 3-17a). The estimated transition state on the disrotatory FMPES is located at a PP separation of 4.2 Å. The formation of *cis*-1,-3-butadiene (*cis*-$P_{EFEI,BO}$) occurred in the same position as indicated in the Born-Oppenheimer MEP.

In the conrotatory FMPES, the energy steadily decreases as the system progressed from reactant-like geometries at small PP separations to structures with larger PP separations resembling the conrotatory transition stat (Fig. 3-17b). The estimated transition state on the conrotatory FMPES is located at a PP separation of 3.5 Å. The *cis*-1,3-butadiene product was not observed on the conrotatory FMPES. This can be attributed to the fact that no barrier between *cis* and *trans* products was observed on any part of the FMPES. The position of *trans*-1,3-butadiene was shifted to a larger PP distance in comparison to the Born-Oppenheimer MEP.

For each of the FMPES obtained under EFEI mechanochemical conditions, the barriers for the disrotatory and conrotatory reactions can be estimated from the MEP. The estimated barriers as a function of applied F_{ext} are shown in Figure 3-18. The barriers were calculated using the optimized reactant structures at each F_{ext} and the estimated transition states on the FMPESs. It was found that increasing the applied F_{ext} between *cis*-PPs reduces the barrier on the disrotatory FMPES relative to the barrier on the conrotatory FMPES. At F_{ext} = 1500 pN, the barrier for the conrotatory pathway is greater than the barrier for the disrotatory pathway. The reduction of the barrier on the disrotatory FMPES relative to that for the conrotatory pathway is consistent with the results of the FPMD simulations performed with the EFEI model, which showed disrotatory opening at high F_{ext}, consistent with sonication experiments.

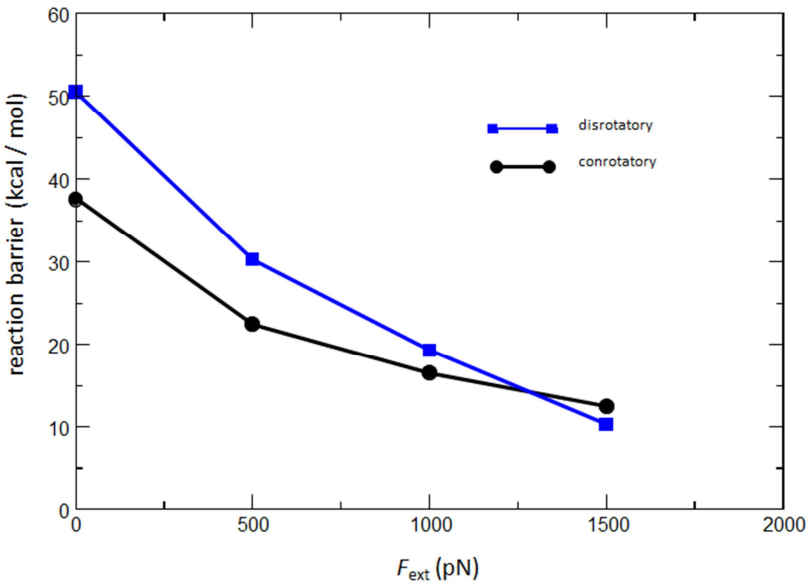

Figure 3-18: Estimated reaction barriers on the FMPES as a function of applied F_{ext} for the conrotatory pathway (black curve) and the disrotatory pathway (blue curve). As F_{ext} increases, the barrier on the disrotatory FMPES decreases relative to the barrier on the conrotatory FMPES. At F_{ext} = 1500 pN, the disrotatory barrier is lower than the conrotatory barrier.

3.7 Comparison of COGEF and EFEI methods

The COGEF and EFEI methods resulted in the system following different reaction pathways in the FPMD simulations of the ring opening of cyclobutene. The data presented above indicate that this difference originates from the different ways in which the COGEF and EFEI models modified the PES. In the case of COGEF, the PES is modified in a way that yields an MEP that initially moves along the disrotatory pathway followed by a transition to the conrotatory pathway once the scissile bond ruptures. In addition, the product along the disrotatory product is not a minimum on the FMPES obtained with COGEF. Meanwhile, the FMPESs obtained with EFEI show that conrotatory and disrotatory pathways remain accessible, but the relative heights of the barriers along these pathways change in a manner that renders the disrotatory pathway kinetically favoured at higher F_{ext}.

The differences in the results of the MD simulations performed with the COGEF and EFEI models may also be influenced by the rate at which the PPs separate with these two techniques. Figure 3-19 provides a comparison of the change in the PP separation obtained in the MD simulations as a function of time. The data show that in EFEI-based simulations, the carbon-carbon scissile bond distance oscillates around a value consistent with that in cyclobutene with F_{ext} = 2900 pN with *cis* PPs prior to bond rupture at t = 1.6 ps. A rapid increase in the PP separation occurs when the scissile bond dissociates, and then the separation oscillates around a constant value consistent with that in the product. The rapid jump between reactant and product distances over a period of a few femtoseconds when the scissile bond ruptures is consistent with the speeds at which reactive processes occur. Meanwhile, the separation between the PPs in the COGEF-based FPMD simulations increases linearly at all points during the simulation. As such, the PPs are separating much too quickly when the reaction does not occur, and far too slowly when the reaction does take place. The latter effect prevents the system from 'jumping' from reactant to product when the scissile bond dissociates. Rather, the system adopts some unstable form where the scissile bond has ruptured, but the PPs are moving too slowly due to the application of the constraints in the COGEF model. The time spent in this unstable state provides the system with an opportunity to explore other reaction pathways.

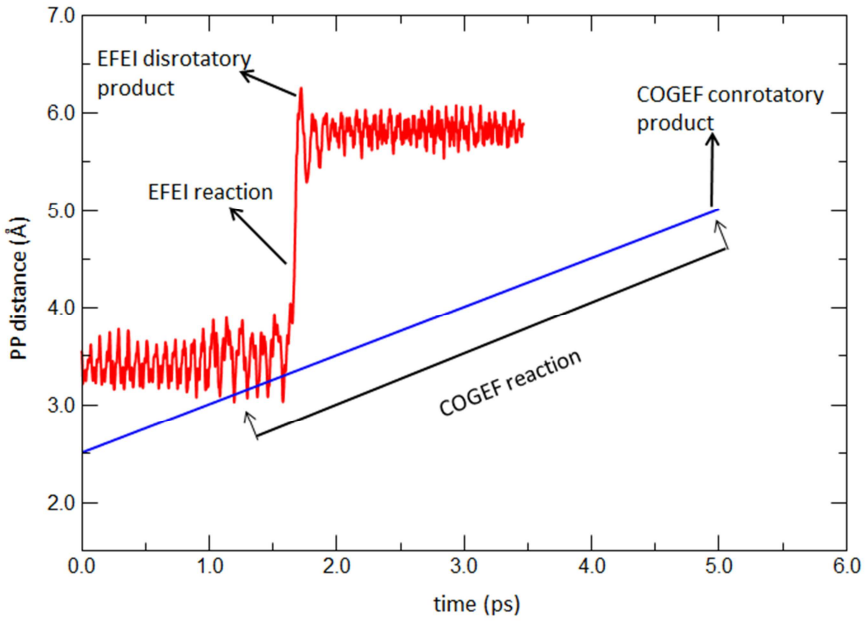

Figure 3-19: Changes in PP distance during FPMD simulations for the ring opening of cyclobutene under COGEF mechanochemical conditions (blue curve) at a pulling rate of 0.5 Å/ps and EFEI mechanochemical conditions (red curve) at F_{ext} = 2900 pN.

3.8 Summary

Overall, the results demonstrate that the method of simulating the presence of an external force directly affects the outcome of MD simulations. The ring opening of cyclobutene was observed to proceed exclusively through a conrotatory manner in the COGEF based MD simulations and in a disrotatory manner in the EFEI based MD simulations. The FMPESs obtained using both approaches were found to be significantly different. In the COGEF-based FMPES, the system does not follow a pathway that leads to the disrotatory product. This is because it is energetically unfavourable to form the disrotatory product on the COGEF FMPES. In contrast to the COGEF-based FMPES scans, the EFEI-based FMPES scans showed that the disrotatory pathway can be accessed due to a reduction in reaction barrier relative to the conrotatory pathway. The explicit inclusion of F_{ext} in the EFEI based simulations directly lowers

the Born-Oppenheimer potential energy and permits the reaction to follow the disrotatory. It was found that the constant pulling rate in the COGEF-based simulations resulted in a slower reaction timescale than observed in the EFEI based simulations, which allowed the system enough time to follow a conrotatory pathway. The results presented in this chapter suggest that mechanochemical processes should be modeled using the EFEI method since this approach is consistent with sonication experiments and captures the ring opening of cyclobutene in timescales that resemble typical chemical reactions.

---

[1] Ribas-Arino, J.; Shiga, M.; Marx, D. *Angew. Chem. Int. Ed*. **2009**, *48*, 4190-4193

[2] Beyer, M.K. *J. Chem. Phys*. **2000**, *112*, 7307-7312

[3] Friedrichs, J.; LüBmann, M.; Frank, I. *ChemPhysChem*, **2010**, *11*, 3339-3342

[4] Hohenberg, P.; Kohn, W.; *Phys. Rev*. **1964**, *136*, B684.

[5] Hickenboth, C.R.; Moore, J.S.; White, S.R.; Sottos, N.R.; Baudry, J.; Wilson, S.R. *Nature*, **2007**, *446*, 423-427.

[6] Ong, M.T.; Leiding, J.; Tao, H.; Virshup, A.M.; Martinez, T.J. *J. Am. Chem. Soc*. **2009**, *131*, 6377-6379

[7] Andersson, K.; Malmquist, P.A.; Roos, B.O.; Sadlej, A.; Wolinski, K. *J. Phys. Chem*. **1990**, *94*, 5483.

[8] Andersson, K.; Malmquist, P.A.; Roos, B.O. *J. Chem. Phys*. **1992**, *96*, 1218.

[9] Roos, B.O. *Adv. Chem. Phys*. **1987**, *69*, 399

[10] Schmidt, M.W.; Baldridge, K.K.; Boatz, J.A.; Elbert, S.T.; Gordon, M.S.; Jensen, J.H.; Koseki, S.; Matsunaga, N.; Nguyen, K.A.; Su, S.; Windus, T.L.; Dupuis, M.; Montgomery, J.A. *J.Comput. Chem.* **1993**, *14*, 1347-1363.

[11] Gordon, M.S.; Schmidt, M.W. in *Theory and Applications of Computational Chemistry the First Forty Years*. (Eds.: C. E. Dykstra,G. Frenking, K. S. Kim,G. E. Scuseria), Elsevier, Amsterdam, **2005**, pp. 1167 – 1189.

[12] Hoover, W.G. *Phys. Rev. A* **1985**, *31*, 1695-1697

[13] Nosé, S. *J. Chem. Phys*. **1984**, *81*, 511-519

[14] Gaussian 09, Revision A.1, Frisch, M. J.; Trucks, G. W.; Schlegel, H. B.; Scuseria, G. E.; Robb, M. A.; Cheeseman, J. R.; Scalmani, G.; Barone, V.; Mennucci, B.; Petersson, G. A.; Nakatsuji, H.; Caricato, M.; Li, X.; Hratchian, H. P.; Izmaylov, A. F.; Bloino, J.; Zheng, G.; Sonnenberg, J. L.; Hada, M.; Ehara, M.; Toyota, K.; Fukuda, R.; Hasegawa, J.; Ishida, M.; Nakajima, T.; Honda, Y.; Kitao, O.; Nakai, H.; Vreven, T.; Montgomery, Jr., J. A.; Peralta, J. E.; Ogliaro, F.; Bearpark, M.; Heyd, J. J.; Brothers, E.; Kudin, K. N.; Staroverov, V. N.; Kobayashi, R.; Normand, J.; Raghavachari, K.; Rendell, A.; Burant, J. C.; Iyengar, S. S.; Tomasi, J.; Cossi, M.; Rega, N.; Millam, N. J.; Klene, M.; Knox, J. E.; Cross, J. B.; Bakken, V.; Adamo, C.; Jaramillo, J.; Gomperts, R.; Stratmann, R. E.; Yazyev, O.; Austin, A. J.; Cammi, R.; Pomelli, C.; Ochterski, J. W.; Martin, R. L.; Morokuma, K.; Zakrzewski, V. G.; Voth, G. A.; Salvador, P.; Dannenberg, J. J.; Dapprich, S.; Daniels, A. D.; Farkas, Ö.; Foresman, J. B.; Ortiz, J. V.; Cioslowski, J.; Fox, D. J. Gaussian, Inc., Wallingford CT, 2009

[15] Woodward, R.B.; Hoffmann, R.; *Angew. Chem. Int. Ed.* **1969**, *8*, 781-853.

[16] Woodward, R.B.; Hoffmann, R.; *J. Am. Chem. Soc.* **1965**, *87*, 395-397.

Chapter 4: Orbitals under Mechanochemical conditions

4.1 Introduction

The violation of the Woodward-Hoffmann (WH) rules[1,2] observed in previous sonication experiments and the results of the MD simulations based on the 'External Force is Explicitly Included' (EFEI)[3] method in the previous chapter have motivated further studies on investigating the formation of the formally forbidden disrotatory product. The results obtained from Chapter 3 are consistent with those obtained by Martinez and coworkers[4]. In that work, first-principles molecular dynamics (FMPD) and force-modified potential energy surface (FMPES) scans were performed to show that application of an external force, F_{ext}, between *cis*-substituents in cyclobutene activates the disrotatory pathway. Both studies showed that the disrotatory pathway is activated because the barrier is reduced on the FMPES. The conclusions from the work of Martinez and coworkers, as well as the results from Chapter 3, explain the formation of the disrotatory product in terms of energetics. Ultimately, the WH rules are based on the conservation of orbital symmetry. The typical route taken to undergo a thermally forbidden pathway is to irradiate the system, which changes the electronic state and orbital occupations. However, the application of F_{ext} does not interact with the electronic structure in a manner that can induce excitations. Therefore, it would be of fundamental interest to investigate how applying F_{ext} promotes reactions that are forbidden by the WH rules. The objective of this chapter is to examine how the WH rules are being circumvented from an electronic perspective. This was accomplished by performing quantum chemical calculations to study how the electronic structure evolves during the disrotatory opening of cyclobutene and the conrotatory,

which is the formally forbidden pathway, opening of cyclohexadiene under mechanochemical conditions.

4.2 Computational details

All calculations were performed at the CASSCF/6-31G(d,p) level of theory. For the ring opening of cyclobutene, an active space of four electrons in four orbitals (4,4) was specified in the simulations. For the ring opening of cyclohexadiene, an active space of six electrons in six orbitals (6,6) was specified in the simulations. FPMD simulations and intrinsic reaction coordinate (IRC) calculations based on the EFEI model were performed using a version of the GAMESS-US software package[5,6] that we modified to enable calculations on the FMPES. The MD simulations were performed under canonical (NVT) conditions using a Nosé-Hoover thermostat[7,8] to maintain a temperature of 300K. The simulations were carried out for a 5 ps timescale with a time step of 1.0 fs. The populations of the natural orbitals comprising the active space for the ring openings of cyclobutene and cyclohexadiene were monitored throughout the FPMD simulations and along the reaction coordinate. The results are presented in Sections 4.3 and 4.4 for the FPMD simulations and IRC calculations respectively.

The analysis of the natural orbital populations will be further discussed by examining how the application of F_{ext} affects the molecular geometries of key species along the reaction coordinate. The structures of the molecular geometries and natural orbitals are presented in Section 4.5. Finally, Section 4.6 describes how mechanochemical control in chemical reactions can be achieved. In particular, this section will investigate how the application of F_{ext} can promote forbidden reactions on the ground state potential energy surface (PES).

4.3 Populations of Natural Orbitals during MD simulations

The disrotatory ring opening of cyclobutene and the conrotatory ring opening of cyclohexadiene were investigated by performing FPMD simulations on the FMPES. The simulations were based on the EFEI approach as discussed in the previous chapter. The force-modified potential energy[1] in the FPMD simulations is expressed as

$$V(\mathbf{x}, F_{ext}) = V_{BO}(\mathbf{x}) - F_{ext}q(\mathbf{x}) \tag{4.1}$$

where $V(\mathbf{x}, F_{ext})$ is the force-modified potential energy function that arises from applying a constant F_{ext} between the PPs, V_{BO} is the Born-Oppenheimer potential energy as a function of all nuclear coordinates **x** without any constraints, and $q(\mathbf{x})$ is the calculated distance between PPs. The hydrogen atoms attached to the carbon atoms of scissile bond were used as PPs, with the PPs in a *cis*-configuration to induce opening along the disrotatory pathway and a *trans*-configuration was used to induce opening along the conrotatory pathway.

The FPMD simulations of cyclobutene showed that the forbidden process occurred within the simulated time scales when $F_{ext} \geq 2800$ pN and the allowed process occurred when $F_{ext} \geq 3100$ pN.The populations of the natural orbitals were monitored throughout the FPMD simulation for the thermally allowed and forbidden pathways to determine how the electronic structure changed during the ring opening processes. The populations of the natural orbitals comprising the active space of cyclobutene are shown in Figure 4-1. These data show that when the system follows the disrotatory pathway, it is closed-shell with populations of 0 or 2 for the majority of the simulation. However, at approximately 1.6 ps, a diradical is briefly formed, as

shown by the crossing between the lowest energy reactant orbital (green curve) and the highest energy reactant orbital (black curve). The diradical formed during the FMPD simulations of the disrotatory ring opening of cyclobutene is not a stationary point, however, it is a structure that the system passes through along the reaction coordinate. Previous studies have shown that diradical formation occurs during the disrotatory ring opening of cyclobutene in the absence of F_{ext} and is necessary to meet the changes in orbital symmetry that occur during this reaction. [9,10]

The populations of the natural orbitals for the conrotatory opening of cyclobutene show that the diradical is not formed during the FPMD simulations, however, the orbital populations exhibit a small 'jump' at approximately 2.0 ps (Fig 4-1b). This result is consistent with the formation of a delocalized structure during the conversion of cyclobutene into 1,3-butadiene and is expected for the ring opening of cyclobutene along the thermally allowed pathway.

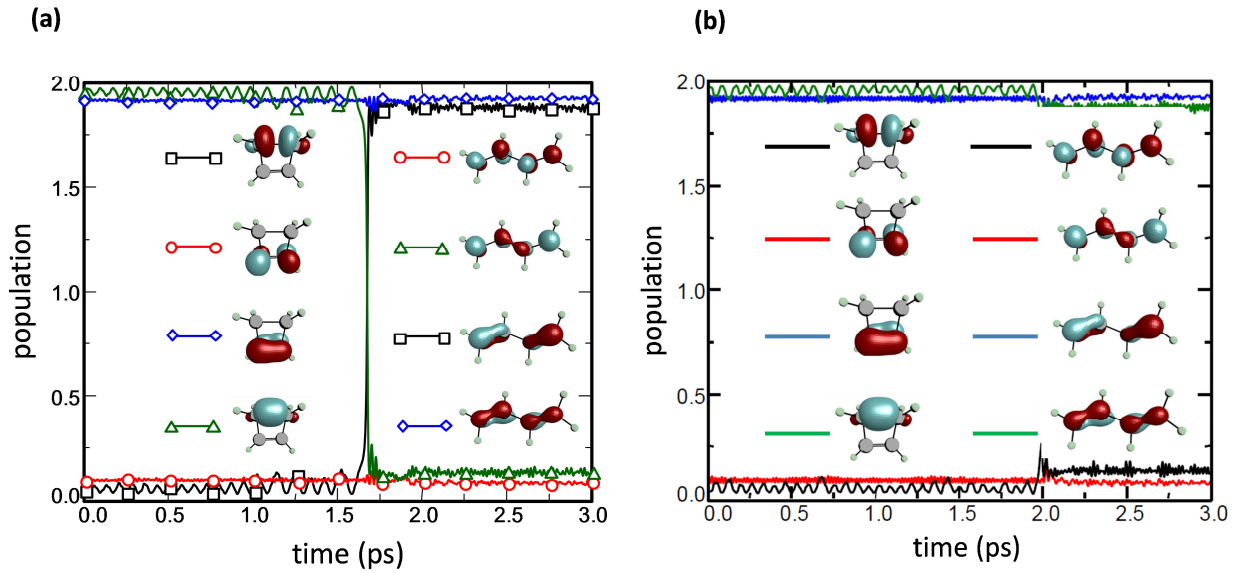

Figure 4-1: Populations of the natural orbitals comprising the active space during FPMD simulations of the ring opening of cyclobutene for the (a) disrotatory pathway at F_{ext} = 2800 pN and (b) conrotatory pathway at F_{ext} = 3100 pN. The natural orbitals of the reactants and products are shown at the left and right, respectively for each curve. The different colored curves denote correlated orbitals and the colours on the orbitals indicate different phases of the wave function. The orbitals are arranged from bottom to top in order of increasing energy. [11]

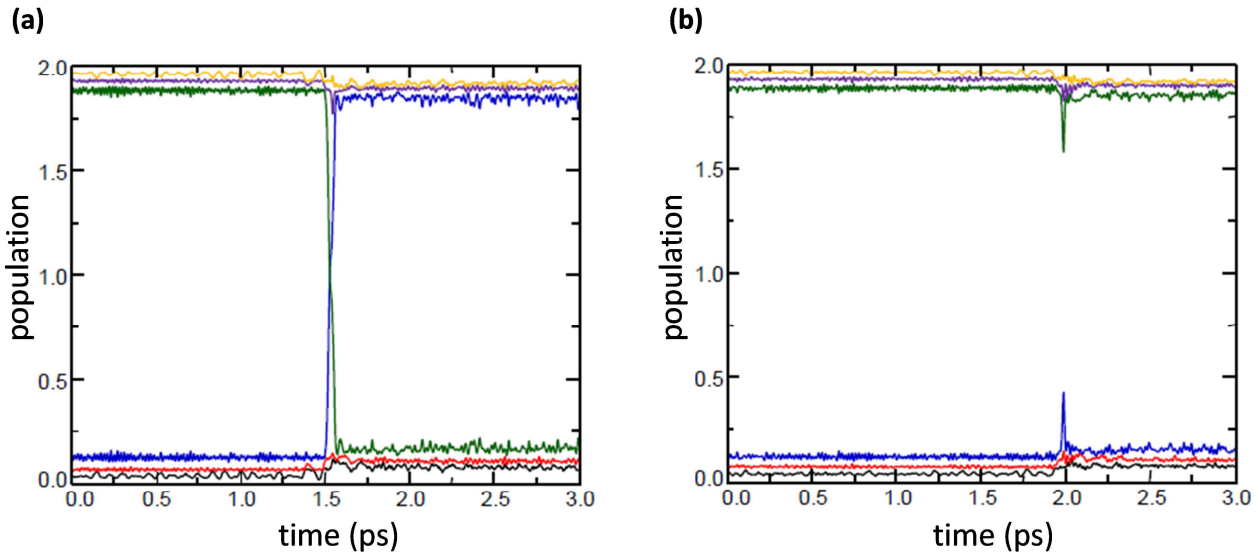

Figure 4-2: Populations of the natural orbitals comprising the active space during FPMD simulations of the ring opening of cyclohexadiene for the (a) conrotatory pathway at F_{ext} = 5400pN and (b) disrotatory pathway at F_{ext} = 4100pN. The different coloured curves denote correlated orbitals [11]

The populations of the natural orbitals comprising the active space for the ring opening of cyclohexadiene are given in Figure 4-2. The data corresponding to the thermally allowed disrotatory pathway indicate that a diradical is not formed during this process. As in the case of the ring opening of cyclobutene along the conrotatory pathway, a sharp jump is observed in the population of the natural orbitals at approximately 2.0 ps when the system converts to products. The populations of the natural orbitals for the ring opening of cyclohexadiene along the thermally forbidden conrotatory pathway indicate that a diradical is formed at approximately 1.5ps. This result is similar to the behavior observed along the disrotatory pathway of cyclobutene and is expected for a reaction that is forbidden by the WH rules.

4.4 Populations of Natural Orbitals along IRC

IRC calculations were performed to examine the electronic structure of the ring openings of cyclobutene and cyclohexadiene over a wider range of F_{ext} than was possible with the FPMD simulations. The populations of the natural orbitals along the IRC for the ring opening of cyclobutene along the conrotatory and disrotatory pathways are shown in Figure 4-3. The populations of the natural orbitals were calculated along the IRC at F_{ext} values of 0, 1000, 2000, and 3000 pN.

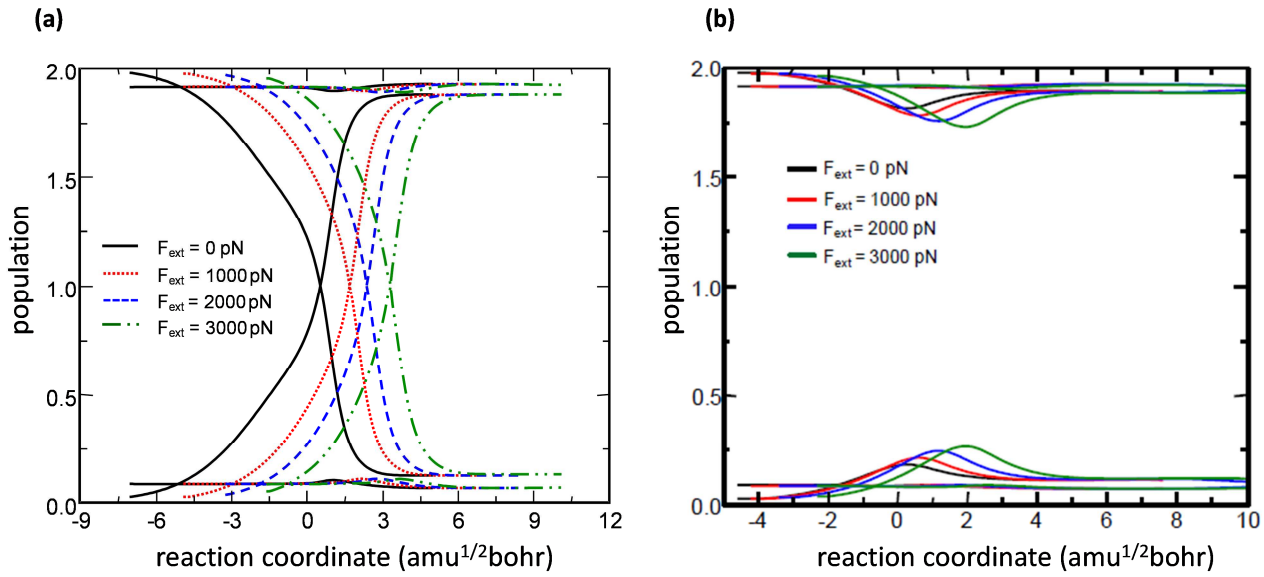

Figure 4-3: Populations of the natural orbitals comprising the active space along the IRC for the ring opening of cyclobutene along (a) the disrotatory pathway and (b) the conrotatory pathway. The natural orbitals monitored are analogous to those shown in Fig. 4.1. The transition state is located at 0 amu $^{1/2}$ bohr. Four curves are shown for each value of F_{ext}. [11]

The populations of the natural orbitals along the IRC for the disrotatory ring opening of cyclobutene demonstrate that the system progresses through a diradical structure regardless of increased applied F_{ext} (Fig. 4-3a). As such, the application of F_{ext} does not cause the evolution of the electronic structure to differ significantly from the reaction in the absence of F_{ext}. As the value of F_{ext} increases, the separation between the transition state and the diradical increases along the reaction coordinate. The populations of the natural orbitals along the IRC for the conrotatory ring opening of cyclobutene are consistent with the results obtained from the FPMD simulations in Figure 4-1b. The data shows a slight decrease in the population of one of the occupied orbitals and an increase in the population of one of the unoccupied orbitals as the system moves from reactants to products (Fig. 4-3b). The distance between this delocalized structure and the transition state increase steadily with F_{ext} as observed for the diradical and transition state in the disrotatory pathway.

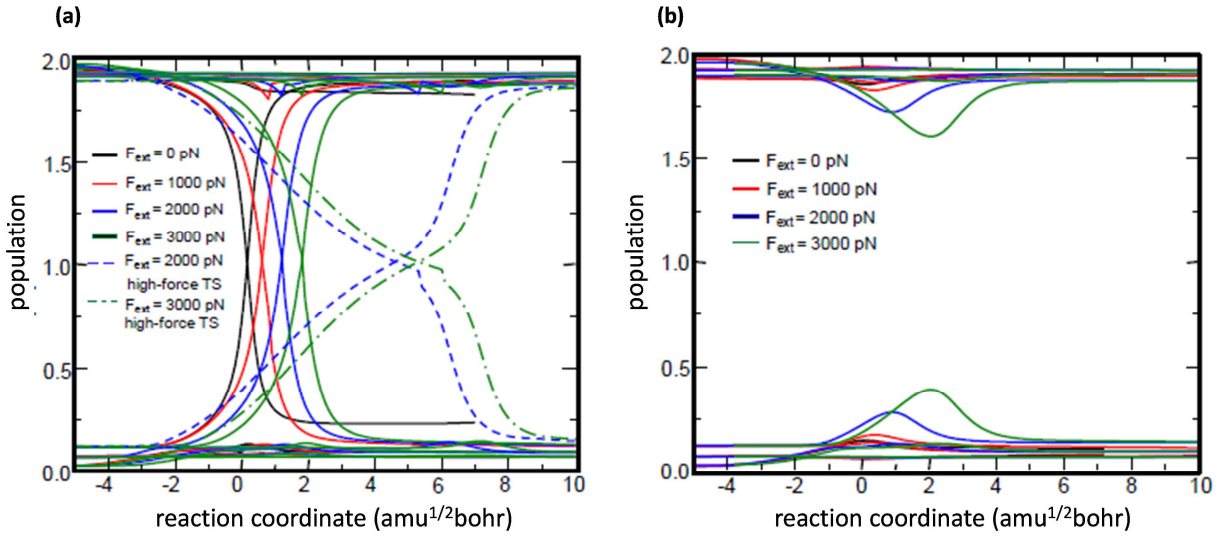

Figure 4-4: Populations of the natural orbitals comprising the active space along the IRC for the ring opening of cyclohexadiene along (a) the conrotatory pathway and (b) the disrotatory pathway. The transition state is located at 0 amu $^{1/2}$ bohr. Four solid curves represent the populations at various values of F_{ext}. The dashed curves in (a) represent the IRCs calculated using the high-force transition state at F_{ext} = 2000 and 3000 pN.[11]

The populations of the natural orbitals along the IRC for the conrotatory ring opening of cyclohexadiene demonstrate that the system proceeds through a diradical structure at all values of F_{ext} (Fig. 4-4a). The distance between the diradical structure and the transition state increases with F_{ext} as observed in the case of the ring opening of cyclobutene along the disrotatory pathway. Two sets of data are provided for F_{ext} = 2000 pN and 3000 pN, which correspond to IRCs calculated using different transition state structures. Two distinct transition states were located along the conrotatory pathway for the ring opening of cyclohexadiene. The structures of these transition states are shown in Figure 4-5. One of the transition states is observed when $F_{ext} \leq 1500$ pN whereas the other transition state is observed when $F_{ext} > 1500$ pN. The latter is referred to as the high-force transition state in Figure 4-4a.

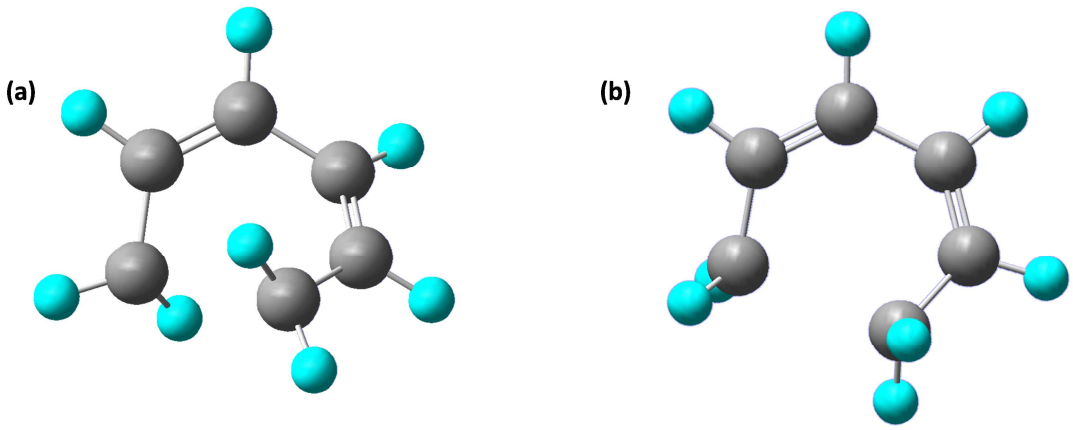

Figure 4-5: Chemical structures of the transition states for the conrotatory pathway of cyclohexadiene at **(a)** F_{ext} = 1000 pN and **(b)** F_{ext} = 2000 pN. The structure shown in **(a)** is present when $F_{ext} \leq 1500$ pN whereas the structure shown in **(b)** when $F_{ext} > 1500$ pN.

The populations of the natural orbitals along the IRC for the disrotatory ring opening of cyclohexadiene are consistent with the results obtained from the FPMD simulations and the populations of the natural orbitals along the IRC for the conrotatory ring opening of cyclobutene. The calculated populations show that the system proceeds through a delocalized structure, which is formed by a slight decrease in the population of one of the occupied orbitals and a slight

increase in the population of one of the unoccupied orbitals (Fig 4-4b). The position of the delocalized structure shifts steadily towards the product as F_{ext} increases.

4.5 Effects of F_{ext} on Molecular Geometry

The separation between the transition state and diradical along the IRC was found to increase with F_{ext} for the disrotatory ring opening of cyclobutene and the conrotatory ring opening of cyclohexadiene. This implies that there is a change in geometry of either or both of these structures as F_{ext} increases. To explore this, the structural details of the transition state and diradical for the ring opening of cyclobutene along the disrotatory pathway were compared by generating line structures at several values of $F_{ext.}$ It is clear that the transition state is more significantly affected by F_{ext} as compared to the diradical, with this structure shifting toward reactant geometries as F_{ext} increases (Fig. 4-7). The shift in the transition state along the reaction coordinate in the reactant direction reduces the barrier, which supports the notion that the application of F_{ext} modifies the potential energy surface (PES) in a manner that accelerates the reactions as discussed in Chapter 3. The diradical structures, however, appear to exhibit similar structures regardless of increased F_{ext}. This result is expected because the electronic structure is determined by geometry, and there exists a limited set of structures on the Born-Oppenheimer PES whose ground-state wave function corresponds to a diradical structure. To further explore the structural differences in the transition state and diradical with F_{ext}, the distance between carbon atoms of the scissile bond was evaluated for the ring openings of cyclobutene and cyclohexadiene along conrotatory and disrotatory pathways. The results are presented in Figure 4-6.

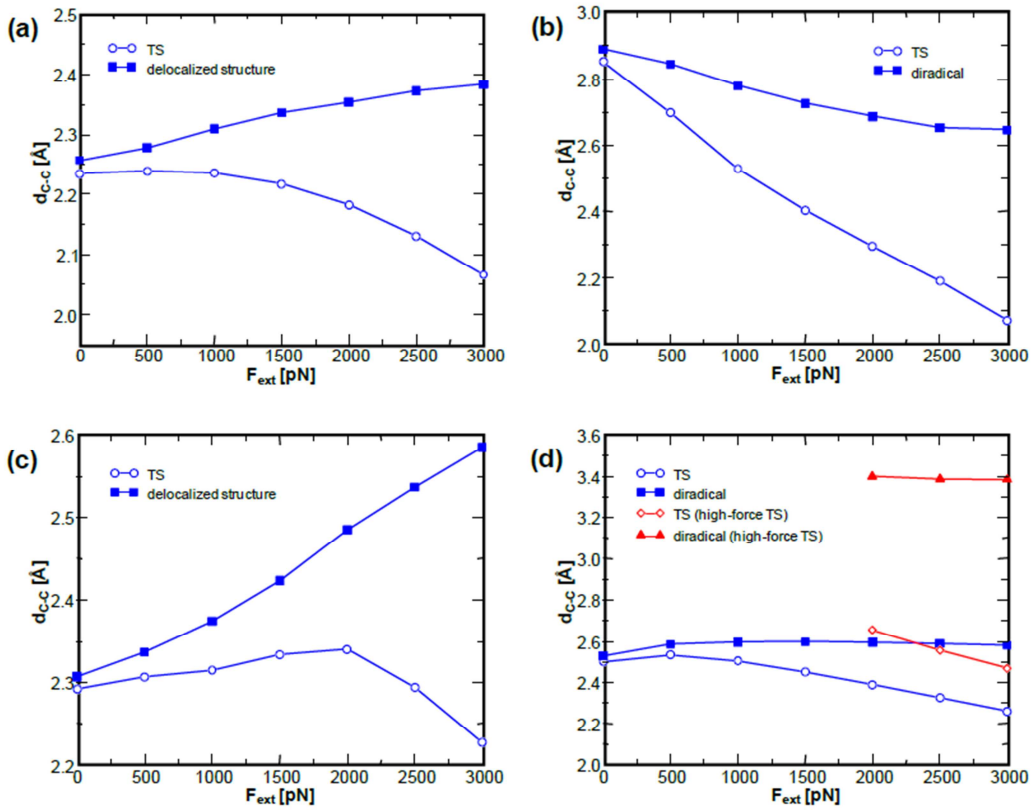

Figure 4-6: Changes in the carbon-carbon scissile bond distance with F_{ext} for (a) the conrotatory ring opening of cyclobutene, (b) the disrotatory ring opening of cyclobutene, (c) the disrotatory ring opening of cyclohexadiene, and (d) the conrotatory ring opening of cyclohexadiene. The red curves in (d) represent the high-force structure.[11]

The data for the conrotatory ring opening of cyclobutene show that the carbon-carbon scissile bond has a distance of approximately 2.25 Å in both the transition state and delocalized structures when F_{ext} = 0 pN. As F_{ext} is increased the carbon-carbon distance in the transition state decreases to a value of 2.07 Å when F_{ext} = 3000 pN (Fig. 4-6a). Meanwhile, the carbon-carbon distance in the delocalized structure is increased to 2.39 Å over the same force range.

The data for the disrotatory ring opening show that the carbon-carbon scissile bond has a distance of approximately 2.85 Å in both the transition state and the diradical structures when F_{ext} = 0 pN. As in the case for the conrotatory opening, the carbon-carbon distance in the

transition state decreased to a value of 2.07 Å at F_{ext} =3000 pN (Fig. 4-6b). However, the diradical structure is not significantly affected by F_{ext} as in the transition state.

Both sets of data for the ring opening of cyclobutene along conrotatory and disrotatory pathways are consistent with line structures shown in Figure 4-7. The carbon-carbon scissile bond distance for the transition state decreases with F_{ext}, which indicates that this structure becomes more reactant-like.

The data for the disrotatory ring opening of cyclohexadiene show that the carbon-carbon scissile bond distance in the transition state is not significantly affected until F_{ext} exceeds a value of 2000 pN. This may reflect the applied F_{ext} affecting other degrees of freedom such as angles and torsions that contribute to the reaction coordinate. The carbon-carbon scissile bond distance in the delocalized structure, however, is strongly affected by the application of F_{ext} in a manner that increases the separation between this structure and the transition state along the reaction coordinate (Fig. 4-6c). Two sets of data are given for the conrotatory ring opening of cyclohexadiene, which correspond to reaction pathways calculated using two different transition states as described in Figure 4-5. The two sets of data are consistent with the results obtained for the disrotatory ring opening of cyclobutene. Specifically, the data illustrates that the carbon-carbon scissile bond distance in the transition state decreases with F_{ext}, while the diradical remains largely unaffected. This can be attributed to the fact that only a small region of the Born-Oppenheimer PES connecting the reactants and products corresponds to a ground state electronic structure with unpaired electrons. The position of the transition state, however, is determined by the shape of the total FMPES, and thus is affected by the application of F_{ext}. As such, the transition state structures are shifted towards the reactants, which activate the disrotatory pathway by reducing the reaction barrier.

As a whole, the results show that the transition state structures are significantly affected by the application of F_{ext} whereas the diradical structure remains largely unaffected for all the reactions considered.

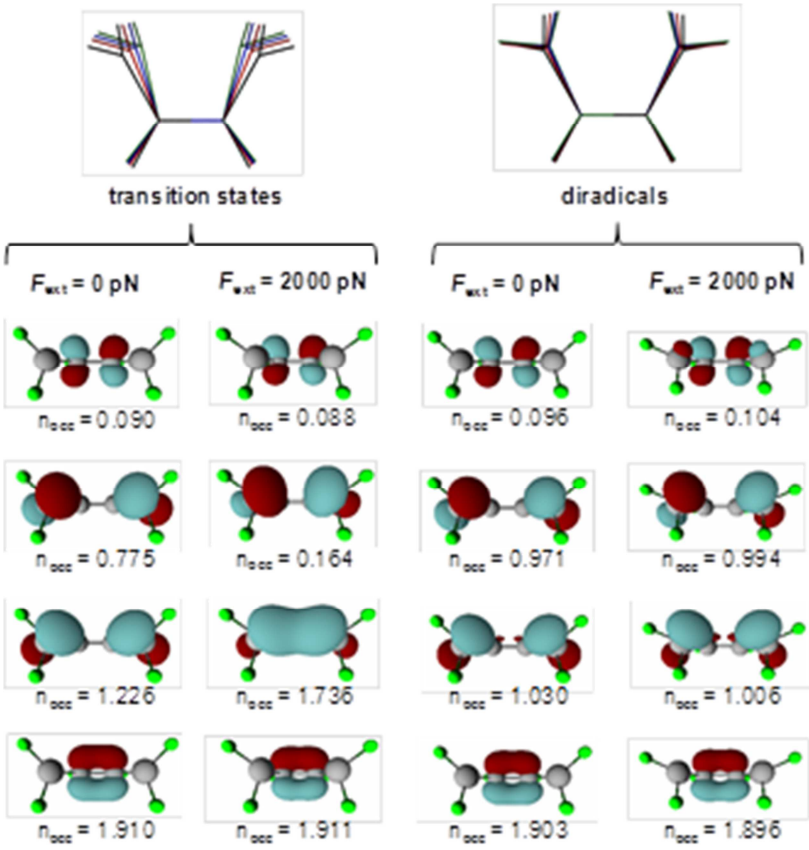

Figure 4-7: Structures, natural orbitals, and natural orbital populations of the transition states and diradicals along the disrotatory pathway for the ring opening of cyclobutene. The line structures provide a comparison of the structure of the transition states and diradicals with black, red, blue, and green lines representing F_{ext} = 0, 1000, 2000, and 3000 pN. The natural orbitals comprising the active space of the transition states and diradicals evaluated with F_{ext}=0 and 2000 pN are shown below the line structures along with their populations. Different colors of the orbitals indicate different phases of the wave function.[11]

The shift in the position of the transition state along the IRC in the reactant direction is also evident from the natural orbitals of cyclobutene with *cis* pulling, which are plotted in Figure 4-7. A comparison of the natural orbitals of the transition state at F_{ext}=0 and 2000 pN indicates that the latter has significant σ bonding character between the carbon atoms of the scissile bond.

The orbital populations in the transition state at F_{ext} = 0 pN indicate that the transition state has a high degree of diradical character. Meanwhile, the orbital populations in the transition state at F_{ext} = 2000 pN are closer to 0 and 2, indicating this structure is shifted toward the reactant. This shift in the position of the transition state toward the reactant on the IRC with increasing F_{ext} causes the transition state and reactant to have increasingly similar structures, and hence energies, reducing the barrier with F_{ext}. The results also show that the diradical formation occurs regardless of F_{ext}. The changes in orbital structures and populations leading to diradical formation are disfavored on the ground state. Furthermore, applying F_{ext} cannot change the electronic state, and must instead induce the necessary changes in the electronic structure by altering the geometry on the ground-state PES.

4.6 Forces along IRC

To investigate how the application of F_{ext} activates the forbidden reactions on the ground state PES, it is convenient to expand Eq. (4.1) as

$$E = \left\langle \psi \left| -\frac{\nabla^2}{2} - \sum_{I=1}^{M}\sum_{i=1}^{N}\frac{Z_I}{r_{iI}} + \sum_{i=1}^{N-1}\sum_{j>1}^{N}\frac{1}{r_{ij}} \right| \psi \right\rangle + \sum_{I=1}^{M-1}\sum_{J>1}^{M}\frac{Z_I Z_J}{r_{ij}} - F_{ext} q(\mathbf{x}) \qquad (4.2)$$

to explicitly show the contributions from the electronic energy (E_{elec}), nuclear-nuclear repulsion energy (E_{NN}), and mechanical work (E_{mech}), which correspond to the first, second, and third terms on the right-hand side, respectively. In Eq. (4.2) atomic units have been used, ψ is the electronic wave function, M and N are the number of nuclei and electrons, respectively, Z_I is the charge of

nucleus I, and r_{ij}, r_{Ii} and r_{IJ} correspond to electron–electron, electron–nucleus, and nucleus–nucleus distances, respectively.

Differentiating each term in Eq. (4.2) with respect to the reaction coordinate, **s**, yields an effective force, $\tilde{\mathbf{F}}_k = -\frac{\partial E_k}{\partial \mathbf{s}}$. This effective force corresponds to how each of the energy contributions affects the motion of the system along the reaction coordinate, where k indicates whether the derivative is evaluated using E_{elec}, E_{NN}, and E_{mech}. The effective force has units of Namu$^{-1/2}$ and the relative magnitudes determine which factors govern the behaviour of the system. The values of $\left|\tilde{\mathbf{F}}_{elec}\right| - \left|\tilde{\mathbf{F}}_{NN} + \tilde{\mathbf{F}}_{mech}\right|$ and $\left|\tilde{\mathbf{F}}_{mech}\right| - \left|\tilde{\mathbf{F}}_{NN} + \tilde{\mathbf{F}}_{elec}\right|$ were evaluated along the IRCs calculated at F_{ext} = 0, 1000, 2000, and 3000 pN. The first of these quantities compares the electronic factors to all other contributions, while the second term compares the mechanical work against all other contributions. The values obtained at F_{ext} = 0 and 2000 pN for the ring opening of cyclobutene along conrotatory and disrotatory pathways are shown in Figure 4-8.

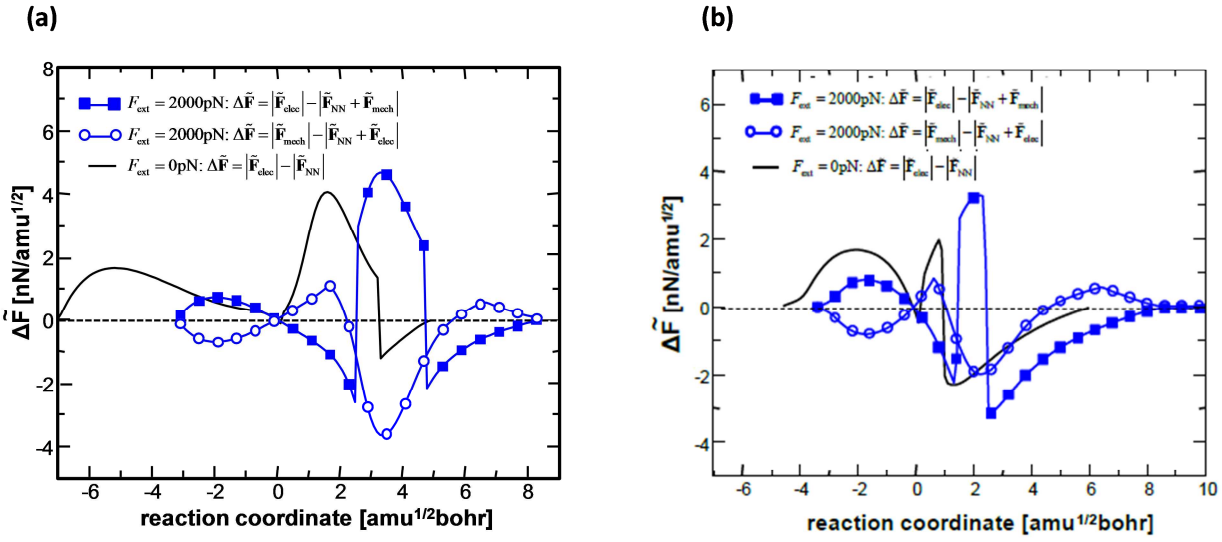

Figure 4-8: Comparison of the contributions to the effective force from E_{lec}, E_{NN}, and E_{mech} at values of F_{ext} = 0 and 2000 pN for the ring opening of cyclobutene along (a) the disrotatory pathway and (b) the conrotatory pathway.[11]

The data for both pathways obtained at F_{ext} = 0 pN only corresponds to $\left|\tilde{\mathbf{F}}_{elec}\right| - \left|\tilde{\mathbf{F}}_{NN}\right|$ because no work was performed on the system. For the disrotatory pathway, the reactants, transition state, and diradical are at positions of -7.0, 0.0, and 0.5 amu$^{1/2}$bohr along the reaction coordinate when F_{ext} = 0 pN. $\left|\tilde{\mathbf{F}}_{elec}\right| - \left|\tilde{\mathbf{F}}_{NN}\right| \geq 0$ within this region, which indicates that progress of the system from the reactant through the transition state and to the diradical is governed by the electronic structure when F_{ext} = 0 pN, as opposed to nuclear-nuclear repulsion. This is consistent with the WH rules that classify this process as forbidden on the basis of orbital symmetry. When F_{ext} = 2000 pN, the reactants, transition state, and diradical are located at -3.2, 0.0, and 2.4 amu$^{1/2}$bohr along the reaction coordinate, respectively. $\left|\tilde{\mathbf{F}}_{elec}\right| - \left|\tilde{\mathbf{F}}_{NN} + \tilde{\mathbf{F}}_{mech}\right| > 0$ between the reactants and transition state, and drops below 0 between the transition state and diradical. Similarly, $\left|\tilde{\mathbf{F}}_{mech}\right| - \left|\tilde{\mathbf{F}}_{NN} + \tilde{\mathbf{F}}_{elec}\right| < 0$ between the reactants and transition state, and exceeds 0 between the transition state and diradical (Fig. 4-8a). Altogether, this indicates that the Born-Oppenheimer energy terms ($E_{\text{elec}} + E_{\text{NN}}$) govern the behavior of the system between the reactant and transition state, while mechanical work controls the behavior between the transition state and diradical. This illustrates how the system can form the disfavored diradical structure under mechanochemical conditions. Essentially, the electronic factors that disfavor diradical formation are rendered secondary to mechanochemical effects that favor an increase in $q(\mathbf{x})$ through carbon-carbon bond scission in the region of the reaction coordinate between the transition state and diradical. These effects were also observed along the IRCs calculated at F_{ext} = 1000 and 3000 pN.

The data for the ring opening of cyclobutene along the conrotatory pathway show that when F_{ext} = 0 pN, the electronic terms dominate the reaction as the system progresses from reactant to transition state (Fig. 4-8b). The region near the transition state (0 amu$^{1/2}$bohr) is

governed by the nuclear-nuclear repulsion term. The electronic terms dominate as the system moves from this region towards the product direction until the IRC reaches approximately 1 amu $^{1/2}$ bohr. The data obtained when F_{ext} = 2000 pN is consistent with the results for the ring opening of cyclobutene along the disrotatory pathway. Specifically, the orbital effects dominate until the system reaches the transition state, and the mechanical work term dictates the behaviour of the system between the transition state and delocalized structure at approximately 1.2 amu $^{1/2}$ bohr. Analogous results were observed for the ring opening of cyclohexadiene along conrotatory and disrotatory pathways (Fig. 4-9). The electronic terms dominate the behaviour of the system between the reactant and the transition state for both conrotatory and disrotatory pathways when F_{ext} = 0 pN. When F_{ext} = 2000 pN, the mechanical work term dictates the behaviour between the transition state and diradical (located at approximately 5.5 amu $^{1/2}$bohr) for the disrotatory pathway. For the conrotatory ring opening of cyclohexadiene, the mechanical work term dictates the behaviour of the system between the transition state and delocalized structure (located at approximately 0.8 amu$^{1/2}$bohr).

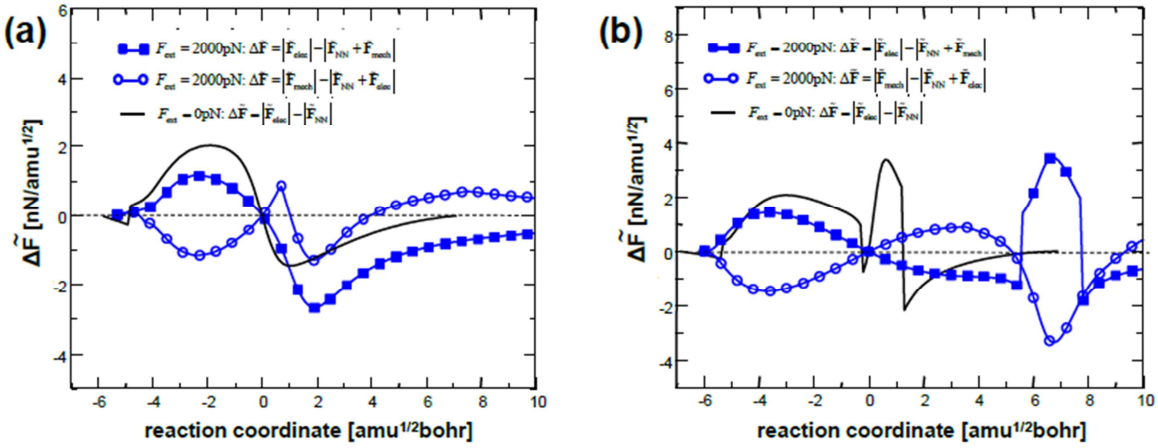

Figure 4-9: Comparison of the contributions to the effective force from E_{lec}, E_{NN}, and E_{mech} at values of F_{ext} = 0 and 2000 pN for the ring opening of cyclohexadiene along (a) the disrotatory pathway and (b) the conrotatory pathway.[11]

4.7 Summary

As a whole, the results clarify how reactions forbidden by the WH rules become allowed through the application of F_{ext}. The evolution of the electronic structure is similar at all values of F_{ext}. As such, the circumvention of the WH rules is not due to a change in electronic structure similar to that achieved through irradiation. Rather, the application of F_{ext} facilitates the forbidden reactions in two ways. First, applying F_{ext} shifts the transition state along the IRC toward the reactants, leading to a reduction in the reaction barrier. Second, when F_{ext} is applied, the orbital effects that disfavor movement from reactant to product along the forbidden pathway are rendered secondary to mechanochemical factors that favour progression toward products. The results in this chapter may be of fundamental value in a broader context than the narrow field of pericyclic reactions. Specifically, they highlight the fact that F_{ext} does not interact directly with the electronic structure of the system. Rather the application of F_{ext} alters the outcome of reactions by manipulating atomic positions, and the underlying contributions to the total energy of the system. Such concepts suggest that mechanochemical activation can be described largely in terms of structural and geometric details without consideration of the underlying electronic structure.

---

[1] Woodward, R.B.; Hoffmann, R.; *Angew. Chem. Int. Ed.* **1969**, *8*, 781-853.

[2] Woodward, R.B.; Hoffmann, R.; *J. Am. Chem. Soc.* **1965**, *87*, 395-397

[3] Ribas-Arino, J.; Shiga, M.; Marx, D. *Angew. Chem. Int. Ed*. **2009**, *48*, 4190-4193

[4] Ong, M.T.; Leiding, J.; Tao, H.; Virshup, A.M.; Martinez, T.J. *J. Am. Chem. Soc.* **2009**, *131*, 6377-6379

[5] Schmidt, M.W.; Baldridge, K.K.; Boatz, J.A.; Elbert, S.T.; Gordon, M.S.; Jensen, J.H.; Koseki, S.; Matsunaga, N.; Nguyen, K.A.; Su, S.; Windus, T.L.; Dupuis, M.; Montgomery, J.A. *J.Comput. Chem.* **1993**, *14*, 1347-1363.

[6] Gordon, M.S.; Schmidt, M.W. in *Theory and Applications of Computational Chemistry the First Forty Years*. (Eds.: C. E. Dykstra,G. Frenking, K. S. Kim,G. E. Scuseria), Elsevier, Amsterdam, **2005**, pp. 1167 – 1189.

[7] Hoover, W.G. *Phys. Rev. A* **1985**, *31*, 1695-1697

[8] Nosé, S. *J. Chem. Phys*. **1984**, *81*, 511-519

[9] Sakai, S. *J. Mol. Structure (Theochem)*. **1999**, *461*, 283-295.

[10] Breulet, J.; Schaefer, H.F. *J. Am. Chem. Soc*. **1984**, *106*, 1221-1226.

[11] Kochhar, G.S.; Bailey, A.; Mosey, N.J. *Angew. Chem. Int. Ed*. **2010**, *49*, 7452-7455.

Chapter 5: Conclusions and Future Work

Mechanochemistry – the activation of chemical reactions through the application of mechanical stresses between atoms in a molecule – has emerged as a topic of significant interest in the last five years. This interest has been prompted largely by several experimental results demonstrating that mechanical stresses can be used to selectively guide chemical systems along specific reaction pathways. A key example involves the activation of pericyclic reactions along reaction pathways that are formally forbidden according to the Woodward-Hoffmann (WH) rules. [1,2] The studies presented in this thesis provide fundamental insight into the manner in which mechanical stresses can be used to induce pericyclic reaction, particularly ring-openings, and illustrate how the outcomes of chemical simulations performed under mechanochemical conditions can be affected by the way in which the system is exposed to a mechanical stress.

The results presented in Chapter 3 focus on exploring how the outcomes of simulations performed to explore the ring opening of cyclobutene under mechanochemical conditions depend on the manner in which the external force is applied. Specifically, stresses were incorporated into molecular dynamics (MD) simulations using either the COGEF or EFEI methods . COGEF-based calculations involve specifying a target distance to be maintained between two pulling points (PPs) and applying a force needed to maintain the distance constraint. In molecular dynamics (MD) simulations, the target PP separation is increased at a constant rate to mimic the application of an external force. EFEI-based simulations apply a specific external force, F_{ext}, between the PPs and allow the PPs separation to change as needed to maintain this force. The results of the simulations demonstrated that the COGEF model consistently leads to ring opening

along the conrotatory pathway, while the disrotatory pathway is followed when the EFEI model is used. These results are consistent with those of previous MD simulations. Analysis of the force-modified potential energy surfaces (FMPESs) shed light on the origin of this outcome. Specifically, the FMPES obtained with COGEF conditions does not contain a minimum energy path (MEP) that connects the reactant to the product of the disrotatory opening. Indeed, this product is not even a minimum on the FMPES obtained under COGEF conditions. Instead, the system follows an MEP that involves the system moving in a disrotatory manner until the carbon-carbon scissile bond ruptures, after which the methylene groups rotate in a manner that leads to the conrotatory product. Meanwhile, the FMPESs obtained with the EFEI model contain pathways leading to both conrotatory and disrotatory products. At the values of F_{ext} used in the MD simulations, the barrier to the disrotatory pathway is lower than that for the conrotatory process. Overall, these results account for the differences observed in the MD simulations performed with these two different models. In addition, it was found that the constant rate at which the PPs separated in the COGEF-based MD simulations does not reflect the anticipated changes in this separation that would be expected to occur during reactions. As such, it is recommended that the EFEI model be used when performing mechanochemical simulations.

Future work in this area will focus on examining the mechanochemical response of cyclobutene with polymeric substituents attached to the carbon atoms of the scissile bond under COGEF and EFEI conditions. In typical sonication experiments, the collapse of cavitation bubbles leads to stresses that extend and deform systems by inducing large-scale vibrations in long chain polymeric substituents. It would therefore be interesting to examine the outcome of FPMD simulations for the ring opening of substituted cyclobutene under COGEF and EFEI conditions.

Chapter 4 focused on using the EFEI method to investigate how the electronic structure evolves during the ring openings of cyclobutene and cyclohexadiene.[3] The populations of the natural orbitals comprising the active spaces of cyclobutene and cyclohexadiene were monitored throughout the FPMD simulation and along IRCs for the conrotatory and disrotatory pathways. It was found that the systems progressed through a diradical structure for the WH forbidden pathways, at all values of F_{ext}. As the magnitude of F_{ext} increased, the distance between the transition state and the reactant decreased along the reaction coordinate, which leads to a reduction in the barrier. Meanwhile, the structure of the diradical species is largely unaffected by F_{ext}. To investigate how the application of F_{ext} drives forbidden reactions on the ground state potential energy surface (PES), the effects of the electronic, nuclear-nuclear repulsion, and mechanical work terms on the motion of the system were evaluated along the IRCs. It was determined that in the absence of F_{ext}, the electronic terms dominate the behaviour of the system from the progression of the reactant through the transition state to the diradical or delocalized structure for both reactions along conrotatory and disrotatory pathways. In the presence of F_{ext}, the electronic terms dominated the behavior of the system between the reactant and the transition state and the mechanical work term dominated the behavior of the system between the transition state and the diradical or delocalized structure for all reactions considered. As such, the circumvention of the orbital-based WH rules was not due to a change in electronic structure. Instead, the application of F_{ext} rendered the orbital effects secondary to mechanochemical factors that favor the progression towards products.

As a whole, the results presented in this thesis explain the role of F_{ext} in activating reactions mechanochemically. Reactions are activated mechanochemically by the application of F_{ext} performing work on the system, which modifies the PES on which the molecule moves. The

application of F_{ext} does not affect how the electronic structure evolves during a reaction. Increasing the applied F_{ext} does not change the structures the system passes through along the reaction coordinate. Since the barrier is reduced on the FMPES, the system can access structures along the reaction coordinate that would be accessible in the absence of F_{ext}.

---

[1] Woodward, R.B.; Hoffmann, R.; *Angew. Chem. Int. Ed.* **1969**, *8*, 781-853.

[2] Woodward, R.B.; Hoffmann, R.; *J. Am. Chem. Soc.* **1965**, *87*, 395-397

[3] Kochhar, G.S.; Bailey, A.; Mosey, N.J. *Angew. Chem. Int. Ed*. **2010**, *49*, 7452-7455.